A SEARCH FOR THE ASSOCIATED HIGGS PRODUCTION IN THE TAU CHANNEL

A Dissertation

Submitted to the Graduate School

of the University of Notre Dame

in Partial Fulfillment of the Requirements

for the Degree of

Doctor of Philosophy

by

Yury Pogorelov, B.Sc.

_____

Anna Goussiou, Co-Director

_____

Randal Ruchti, Co-Director

Graduate Program in Physics

Notre Dame, Indiana

July 2007

A SEARCH FOR THE ASSOCIATED HIGGS PRODUCTION IN THE TAU CHANNEL

Abstract

by

Yury Pogorelov

A search for the production of neutral Higgs bosons in association with bottom quarks in $p\bar{p}$ collisions at $\sqrt{s} = 1.96$ TeV is presented. The cross section for this process is enhanced in many extensions of the Standard Model (SM), such as in its Minimal Supersymmetric extension (MSSM) at large $\tan\beta$. The search is performed using the decay of the Higgs boson into two τ-leptons. The data, corresponding to a recorded integrated luminosity of 400 pb^{-1}, were collected with the DØ detector at the Fermilab Tevatron Collider. The results provide an upper limit for the production cross section of neutral Higgs bosons in the mass range of 90 to 150 GeV, and are interpreted in the MSSM. This cross section limit is comparable with the one obtained previously using the decay of the Higgs into two b-quarks, despite the 1:9 branching ratio of the $\tau^{+}\tau^{-}$ to $b\bar{b}$ decay modes.

To my Mom and Sister, for their support and encouragement.

CONTENTS

viii

TABLES

ACKNOWLEDGMENTS

CHAPTER 1

INTRODUCTION

1.1 Overview of the Standard Model

The Standard Model (SM) of particle physics is a theory which describes all currently known fundamental particles and their interactions, with the exception of gravity. Up to this date, Standard Model predictions agree with all experiments. According to the Standard Model, there are two types of particles, fermions and gauge bosons. The difference between these is the spin: fermions have half-integer spin whereas bosons have integer spin. Fermions make up all the matter in the universe and gauge bosons are responsible for the mediation of all forces.

TABLE 1.1

STANDARD MODEL FERMIONS: LEPTONS

Generation	Lepton	Name	Mass (MeV/c^2)	Charge	Lifetime
1	e	Electron	0.511	-1	$> 4.2 \times 10^{24} yr$
1	ν_e	Electron neutrino	$< 15 \times 10^{-6}$	0	
2	μ	Muon	105.7	-1	$2.2 \times 10^{-6} s$
2	ν_μ	Muon neutrino	< 0.17	0	
3	τ	Tau	1777	-1	2.9×10^{-13}
3	ν_τ	Tau neutrino	< 24	0	

1

TABLE 1.2

STANDARD MODEL FERMIONS: QUARKS

Generation	Quark	Name	Mass (MeV/c^2)	Charge (e)
1	d	Down	3-7	-1/3
1	u	Up	1.5-3	2/3
2	s	Strange	~ 95	-1/3
2	c	Charm	$\sim 1,250$	2/3
3	b	Bottom	$\sim 4,200$	-1/3
3	t	Top	174,000	2/3

The Matter: Fermions are divided into two families, leptons and quarks. Furthermore, there are three generations of quarks and leptons. Each generation contains a pair of leptons and a pair of quarks. Tables 1.1 and 1.2 show the names and properties of the three generations of leptons and quarks, respectively. Each particle, either lepton or quark, has a corresponding antiparticle.

Most of the visible matter in the universe is made of fermions of the first generation. Every atom in the universe consists of a massive nucleus surrounded by a cloud of electrons. Nuclei are made of protons and neutrons, which in turn are made of "up" and "down" quarks which belong to the first generation. Fermions of the second and third generations are heavier and decay into the particles of the first generation.

The Forces: From the mathematical point of view, the Standard Model is a local gauge invariant relativistic quantum field theory based on the principle of the least action [1]. In gauge theories, the interactions are the result of the local gauge invariance and symmetry. The symmetry of the Standard Model, $SU(3)_C \otimes SU(2)_L \otimes U(1)_Y$, defines all interactions. The $SU(3)_C$ part of the symmetry describes the

strong force, where C stands for color charge. The mediator of the strong force is a massless particle called gluon. The strong force holds the quarks inside hadrons, as well as the protons and neutrons inside nuclei. The $SU(2)_L$ is responsible for the weak interaction, which is mediated by massive particles called W and Z bosons. L stands for left-handed interactions. The β-decay is a result of the weak force. The $U(1)_Y$ part describes the electromagnetic interaction. Y stands for the weak hypercharge defined as $Y = 2(Q - I_3)$, where Q is the electric charge and I_3 is the third component of the weak isospin. The mediator of the electromagnetic interaction is a massless particle called the photon.

TABLE 1.3

STANDARD MODEL GAUGE BOSONS

	Name	Force	Mass (MeV/c^2)	Charge (e)
γ	Photon	electromagnetic	0	0
g	Gluon	Strong	0	0
$W^\pm$	W boson	Weak	80.4	± 1
Z	Z boson	Weak	91.2	0

1.2   The Higgs field

While the strong and electromagnetic forces are mediated by massless gauge bosons, the weak force is mediated by massive bosons (see Table 1.3). In fact, the reason why the weak force is weak or short-ranged is exactly that its mediators are massive. Particle masses in the Standard Model are the result of interaction with a doublet of Higgs scalar fields:

$$H = \begin{pmatrix} H^0 \\ H^- \end{pmatrix}$$

3

The Higgs field is unlike other known physical fields because of its non-zero Vacuum Expectation Value (VEV) which is the result of spontaneous symmetry breaking of the Higgs field in the Standard Model Lagrangian. The non-zero VEV of the Higgs field breaks the Electro-Weak symmetry. As a result, the W and Z bosons acquire mass by absorbing a component of the Higgs field as their longitudinal component. Fermions get their masses through Yukawa couplings to the Higgs field. The fact that the Higgs field couples to ordinary particles like fermions and W/Z bosons means that the Higgs boson can be produced in the interactions of the ordinary particles.

1.3 Supersymmetry

Up to the present, the Standard Model has been extremely successful, its predictions and experiments agreeing with great accuracy. All Standard Model particles, with the exception of the Higgs boson, have been observed in experiments. Despite this great success, the SM has drawbacks and unresolved problems. For example, it contains a large number of free parameters and the strong and electroweak forces are not unified. Also, the Higgs boson is a scalar field and the radiative correction to its mass are quadratic in nature (see Figure 1.1). This creates a hierarchy problem: why vacuum expectation value for the Higgs field is so low compared to where it would be after radiative corrections.

Supersymmetry offers a possible solution to the hierarchy problem. It introduces additional degrees of freedom: for each Standard Model fermion, there is a bosonic partner and for each Standard Model gauge boson, there is a fermionic partner. These additional degrees of freedom cancel the radiative corrections (Figure 1.2). Normally, SUSY requires that the supersymmetric partners have the same mass. However, no supersymmetric particles have been observed in experiment. That
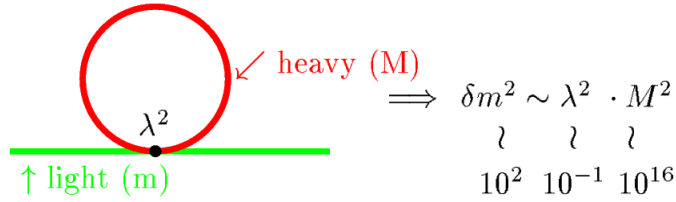
Figure 1.1. Radiative corrections to the light Higgs mass in the Standard Model [2]. Coupling to a heavy fermion with a mass M gives a large contributions to the Higgs mass.

means that Supersymmetry must be broken and super-partners are heavier than SM particles. To provide an effective cutoff in the Higgs loop radiative corrections, the masses of the super-partners must be relatively small, otherwise the hierarchy problem would remain. This fact is a motivation for the current searches of the super-particles at the Tevatron.

Besides a solution to the hierarchy problem, Supersymmetry can offer a solution to the unification of the gauge symmetries within a larger symmetry group. Unification of forces means that at some large energy the coupling constants of different interactions become identical. Exact unification within the SM is not possible because the running constants converge but never became identical (Figure 1.3).

For the supersymmetric extension to be self-consistent, it has to have an even number of Higgs doublets [2]. Therefore, the minimal supersymmetric extension of the SM (MSSM) contains two Higgs doublets. After electroweak symmetry breaking, five Higgs bosons remain. These are two neutral CP-even states, h and H, a neutral CP-odd state, A, and two charged states, H^+ and H^-. Supersymmetric relations between the components of the Higgs fields reduce the number of free parameters in the Higgs sector to just two. Typically, the mass of the CP-odd Higgs boson, m_A, and the ratio of vacuum expectations of two Higgs doublets, $tan\beta$, are chosen
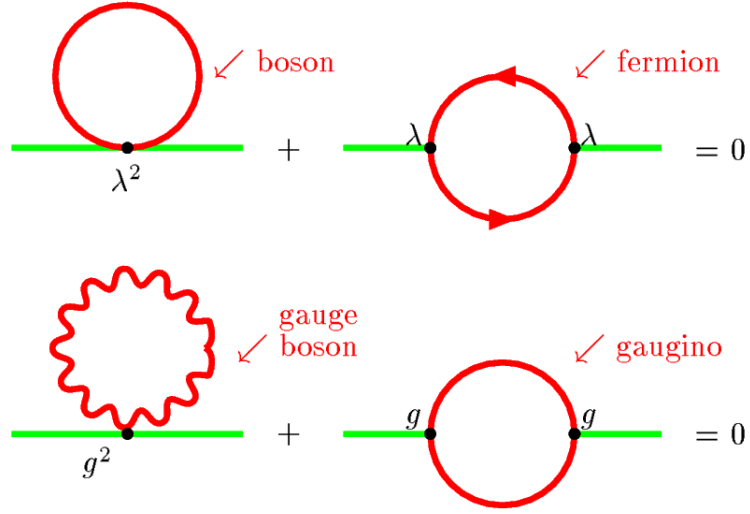
Figure 1.2. Cancellation of the radiative corrections to Higgs mass by the super-symmetric degrees of freedom[2]. Contributions from bosonic degree of freedom is canceled by the fermionic degree of freedom. Similarly, contribution from gauge boson degree of freedom is canceled by the gaugino degree of freedom.
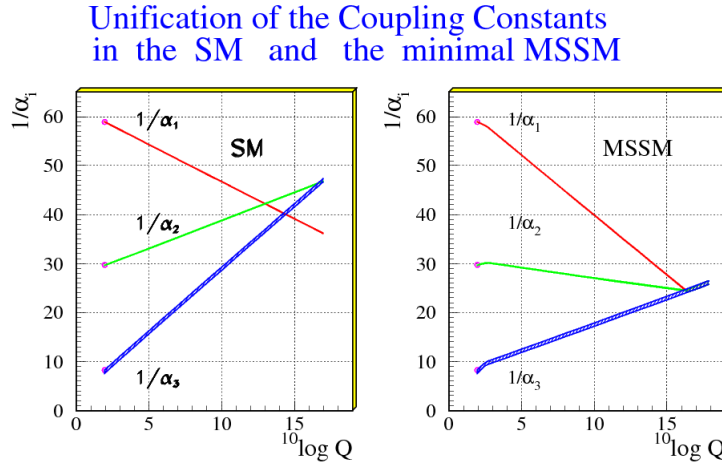
Figure 1.3. Coupling constants for the three forces in SM and MSSM

as the parameters which control the Higgs sector.

1.4 Higgs production at the Tevatron

Higgs bosons can be produced via a number of processes at the Tevatron. Figure 1.4 shows the SM Higgs production cross-sections of different processes as a function of the Higgs mass. The $gg \rightarrow h$ process has the largest cross-section ($\sim$ 1pb at the Higgs mass 120 GeV). The SM Higgs branching ratios are shown on Figure 1.5. For the low Higgs masses, $\sim 90\%$ of the time the Higgs particle decays into a pair of b-quarks and $\sim 10\%$ of the time into a pair of τ-leptons.

The leading order Feynman diagrams for the $gb \rightarrow bh$ and $q\bar{q} \rightarrow b\bar{b}h$ production are shown on Figure 1.6. The Standard Model cross-section for the b-quark associated Higgs production at the Tevatron is very small (0.1-2.0 fb) and, therefore, is out of reach for the Tevatron collider. In the MSSM, however, the A-higgs coupling to down-type quarks is proportional to $tan\beta$; therefore, the leading order MSSM production cross-sections are enhanced by the factor $tan^2\beta$. This opens up an opportunity for the Higgs discovery at the Tevatron. Figures 1.7, 1.8 and 1.9 show the MSSM production cross-sections and Higgs branching ratios for different $tan\beta$ and MSSM scenarios. The $h \rightarrow b\bar{b}$ decay channel has larger branching ratio than the $h \rightarrow \tau^+\tau^-$. However, the $b\bar{b}$ channel suffers from multi-jet QCD backgrounds.

SM Higgs production

σ [fb]

10^3

$gg \rightarrow h$

TeV II

$qq \rightarrow Wh$

10^2

$qq \rightarrow qqh$

$bb \rightarrow h$

10

$qq \rightarrow Zh$

$gg, qq \rightarrow tth$

TeV4LHC Higgs working group

1

100   120   140   160   180   200

m_h [GeV]
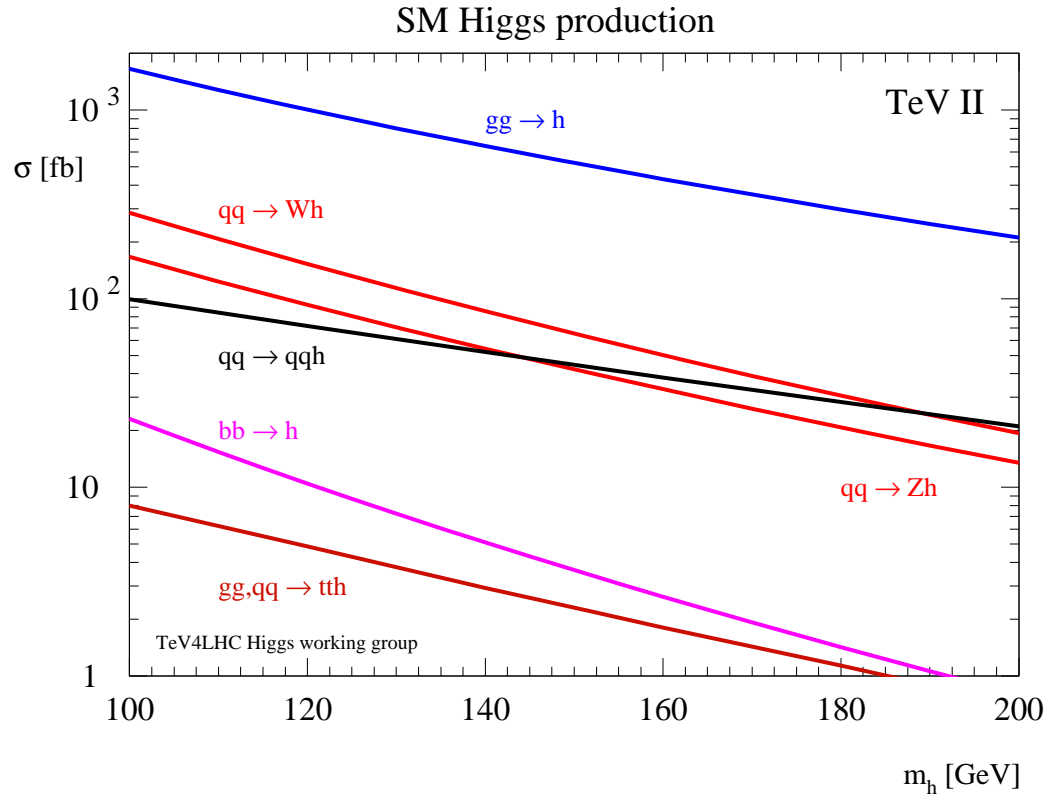
Figure 1.4. The SM production cross-sections of the Higgs at the Tevatron
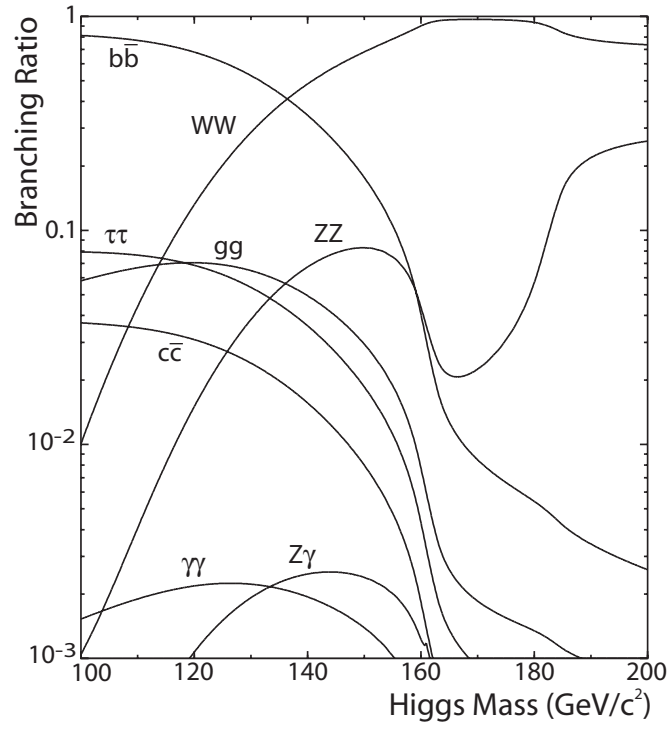
Figure 1.5. The SM Higgs branching ratios
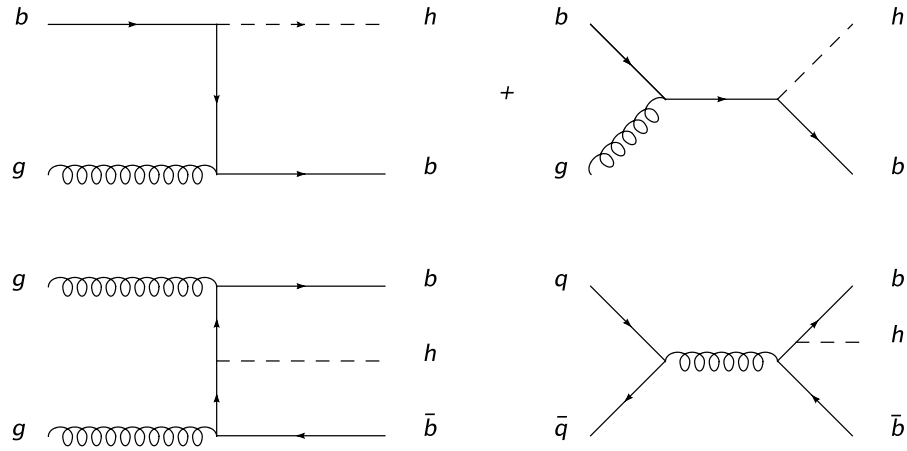
Figure 1.6. Leading Order diagrams of the Higgs production [3].
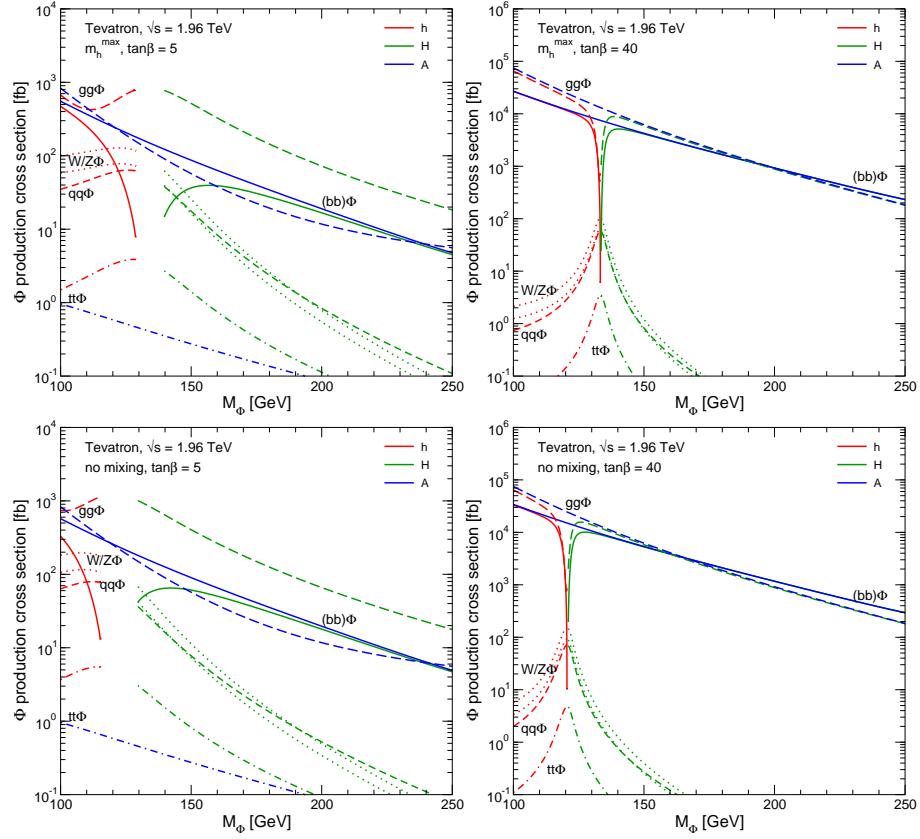
Figure 1.7. The MSSM production cross-sections for $tan\beta = 5$ and 40 for two MSSM scenarios.
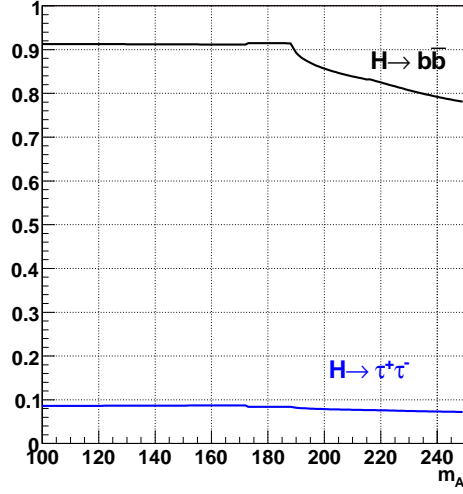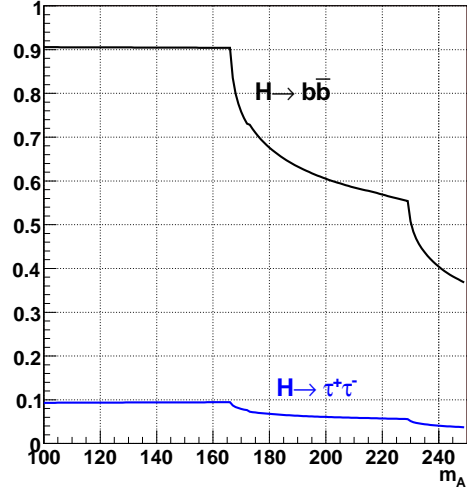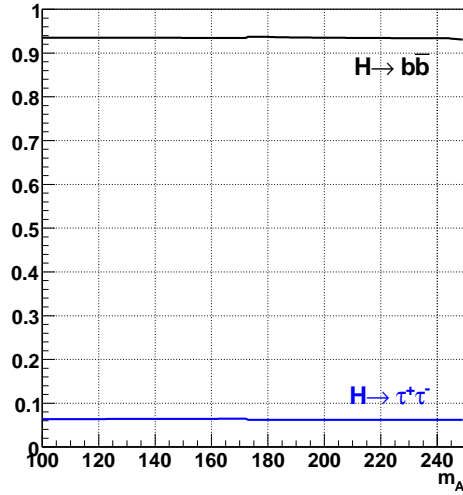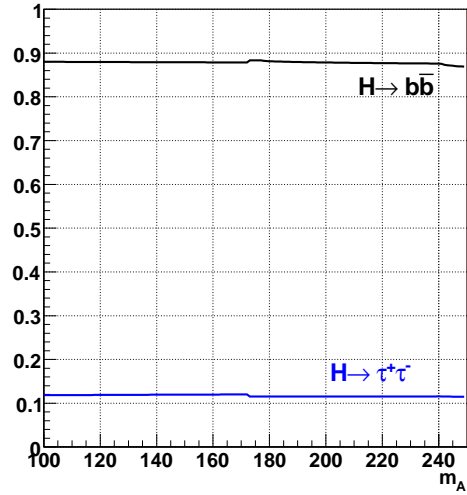
Figure 1.8. The MSSM Higgs (A state) decay branching ratios into $b\bar{b}$ and $\tau^+\tau^-$ (m_h^{max} scenario).

11

(a) $\tan\beta= 5$, $\mu < 0$

(b) $\tan\beta= 5$, $\mu > 0$
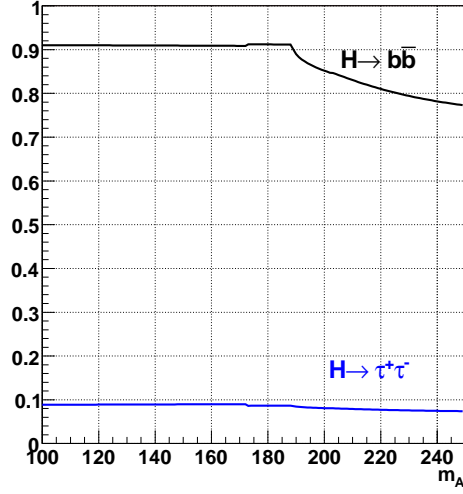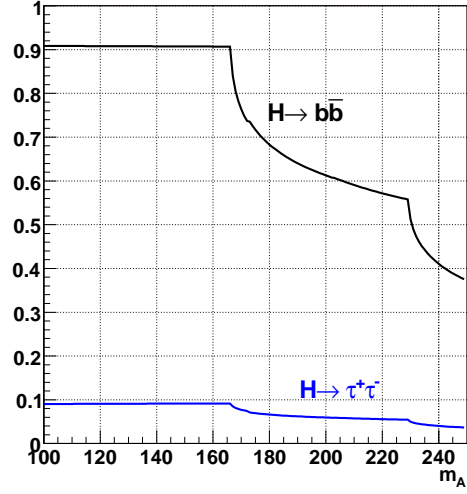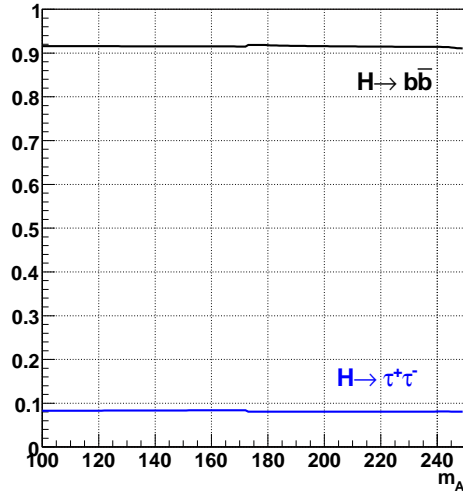
(c) $\tan\beta= 40$, $\mu < 0$
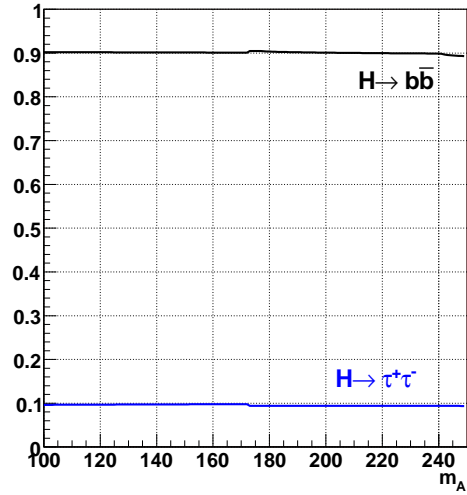
(d) $\tan\beta= 40$, $\mu > 0$

Figure 1.9. The MSSM Higgs (A state) decay branching ratios into $b\bar{b}$ and $\tau^+\tau^-$ (no-mixing scenario).

CHAPTER 2

EXPERIMENTAL APPARATUS

2.1   Fermilab Accelerator Complex

The Fermilab Tevatron Complex is currently the world's highest energy particle accelerator. It is capable of accelerating protons and anti-protons to the energy of 980 GeV. Protons and anti-protons collisions with the center of mass energy of 1.96 TeV are then studied at the two experiments. The aerial picture of the Tevatron complex is shown on Figure 2.1. Particle acceleration at the Tevatron complex (see Figure 2.2) is done in a series of steps described in this chapter.

2.1.1   The Preaccelerator

The first stage of the Tevatron complex is the preaccelerator. Hydrogen gas is released into a magnetron surface-plasma source. The magnetron's electric field strips the electrons from the hydrogen atoms. Protons are then attracted to cathode where they acquire electrons. Protons which acquire two electrons become H^- ions. The magnetron's magnetic field causes the ions to spiral out to the opposite side of the magnetron. Extractor electrodes accelerate the H^- ions to an energy of 18 KeV. After that, an electrostatic Cockroft-Walton device accelerates them to the an energy of 0.75 MeV.

Figure 2.1. Picture of the Fermilab's Tevatron accelerator complex (picture was taken on July 29 of 2003).

2.1.2 The Linac

The next stage of the Tevatron complex is the Linac. A linear accelerator of 500 feet consisting of a series of RF cavities accelerates the H^- ions to an energy of 400 MeV. After that, the ions pass through the debuncher which reduces the momentum spread and removes the Linac bunch structure from the beam. Finally the beam passes through a foil made of carbon which strips the electrons out of the ions leaving only protons.

2.1.3 The Booster

The 400 MeV protons from the Linac enter the next stage - the Booster. The Booster is a synchrotron accelerator 500 feet in diameter. Protons in the synchrotron accelerator are bound to travel in a circular orbit by a set of dipole magnets. A set
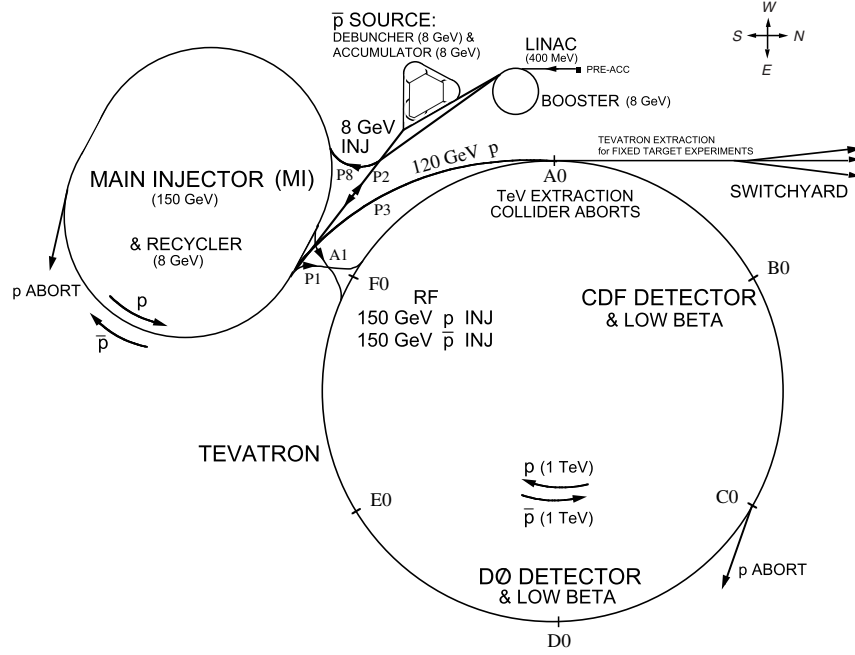
Figure 2.2. Schematic view of the Tevatron Complex

of RF cavities is used to accelerate the protons to an energy of 8 GeV while a set of quadrupole magnets prevents the proton beam from diverging. In the Booster the protons get separated into bunches again, with each bunch containing $5 - 6 \times 10^{10}$ protons.

2.1.4   Main Injector Synchrotron

At the next stage, the 8 GeV proton bunches from the Booster enter the Main Injector synchrotron where they coalesce into one large bunch containing up to about 5×10^{12} protons. The Main Injector is used for two tasks: accelerating protons and anti-protons to an energy of 150 GeV needed by the Tevatron, and accelerating protons to an energy of 120 GeV for feeding the anti-proton source.

2.1.5 Anti-proton Production

While protons are easy to produce from hydrogen, the production of anti-protons is much more difficult. A schematic view of the anti-proton source is shown on Figure 2.3. Protons of 120 GeV from the Main Injector are directed to strike a target made of nickel. Among other particles, the spray of secondary particles contain anti-protons. Next on the path of the secondary particles is a collection lens made of lithium. Low density lithium minimizes absorption and scattering of anti-protons. A large electric current (maximum is 670 kA) applied to the lens creates a circular magnetic field. This field bends the tracks of the secondary particles so that they become parallel to each other at the exit from the lens. To separate negatively charged anti-protons from the the other particles, a dipole magnet is used. The energy of the protons is selected as 120 GeV because in this case the energy of the produced anti-protons is peaked around 8 GeV. For every million protons hitting the target, only 15 anti-protons are created. Because the anti-protons are so hard to produce, the anti-proton beam intensity is one of main limiting factors of the Tevatron.

At the next stage, the 8 GeV anti-protons are sent to the Debuncher and subsequently to the Accumulator. The Debuncher and the Accumulator are both housed in the same "ring" with a triangular shape (Figure 2.2). The main purpose of the Debuncher is to reduce the momentum spread of the anti-protons. To achieve this, a series of RF devices and magnets is used. Transverse oscillations are reduced by applying stochastic cooling. The main purpose of the Accumulator is to accumulate anti-protons in large quantities. Also, it arranges them into the same bunch structure as the protons in the Main Injector. To achieve this, a series of RF elements is used. It takes a few hours to reach the desired amount of anti-protons. Once it is done, the anti-proton beam is sent to the Main Injector where, along with a proton
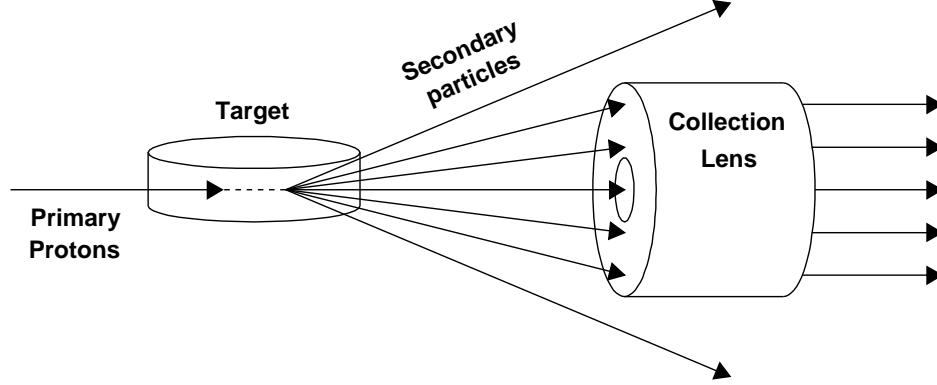
Figure 2.3. Schematic view of anti-proton source

beam it is accelerated to an energy of 150 GeV.

2.1.6   Tevatron

The last stage of the accelerator complex is the Tevatron. It features supercon-
ducting magnets which produce a magnetic field of 4 Tesla and has a circumference
of 4 miles. Protons and anti-protons from the Main Injector are accelerated from 150
GeV to 0.98 TeV. After this energy is achieved, quadrupole lenses squeeze the beams
into small transverse sizes at two collision points - B0 and D0. These two points
are where $p\bar{p}$ collisions occur. The DØ Detector is located at the D0 collision point
and the CDF Detector is at the B0 point. At all other points the two beams are
kept separated. A measure of the number of collisions which take place is known
as the instantaneous luminosity. The instantaneous luminosity is determined by
measuring the number of inelastic $p\bar{p}$ collisions that take place per second at the de-
tector. The DØ and CDF detectors have special sub-detectors just for this purpose.
Instantaneous luminosity units are $cm^{-2}s^{-1}$ and typical instantaneous luminosity in

17

Run IIa is about 30×10^{30} $cm^{-2}s^{-1}$. By integrating instantaneous luminosity over time, one gets the integrated luminosity.

2.2 The Run II DØ Detector

An overview of the DØ detector is presented here. The DØ detector (shown on Figure 2.4) is a nearly-hermetic multipurpose particle detector which started operation in 1992. In Run I, which took place between 1992 and 1999, the DØ detector along with the CDF detector were used in the top-quark discovery. For the Run II of the Tevatron, the DØ detector systems have gone through major upgrades. The tracking system was replaced with a silicon microstrip tracker, a central fiber tracker and preshower detectors. Additionally, a superconducting solenoid with 2 Tesla magnetic field was installed to allow charge and momentum measurement. The DØ Calorimeter in Run II remained the same as in Run I, with the exception of readout electronics which were replaced. The Muon System upgrade included hardware as well as readout electronics. The Data Acquisition System had to be upgraded to deal with increased event rates in Run II.

2.2.1 Coordinate System and Kinematic Variables

The DØ coordinate system is shown on Figure 2.5. DØ uses modified spherical coordinates r, ϕ, η where η is the pseudo-rapidity defined as

$$\eta = -\ln(\tan(\frac{\theta}{2}))$$

and θ is the polar angle with respect to the proton beam. The pseudo-rapidity is the relativistic limit of rapidity y:

$$y = \frac{1}{2}\ln(\frac{E + p_z}{E - p_z})$$
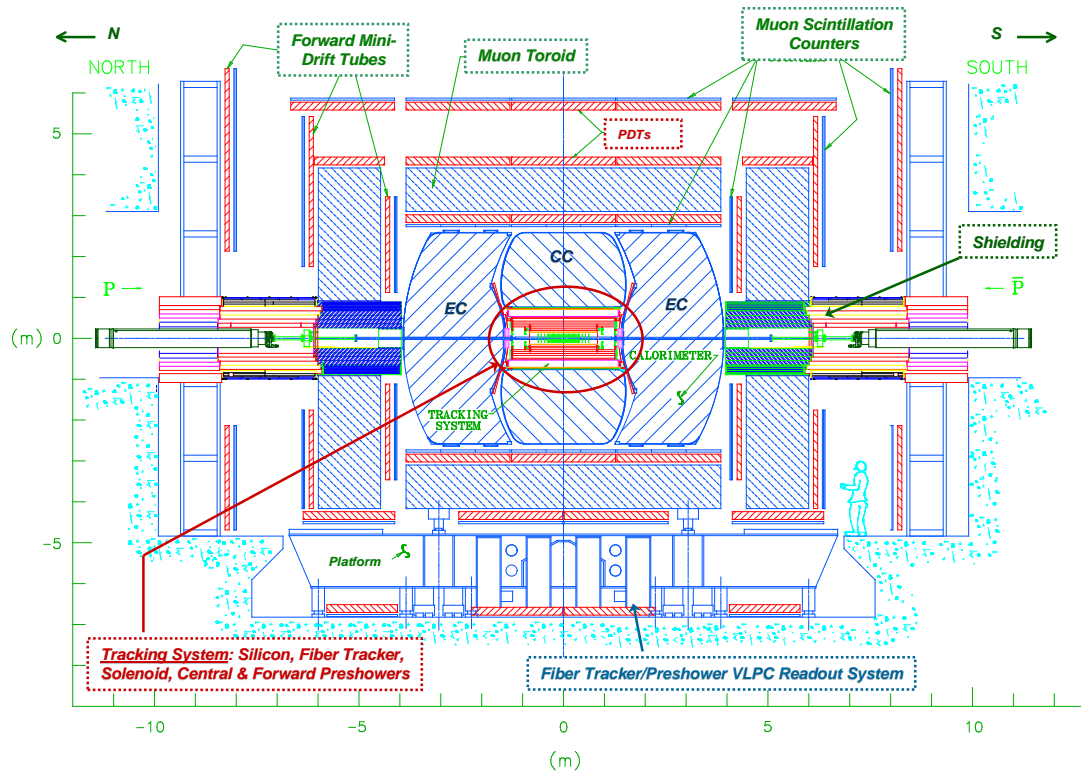
Figure 2.4. Run II DØ detector
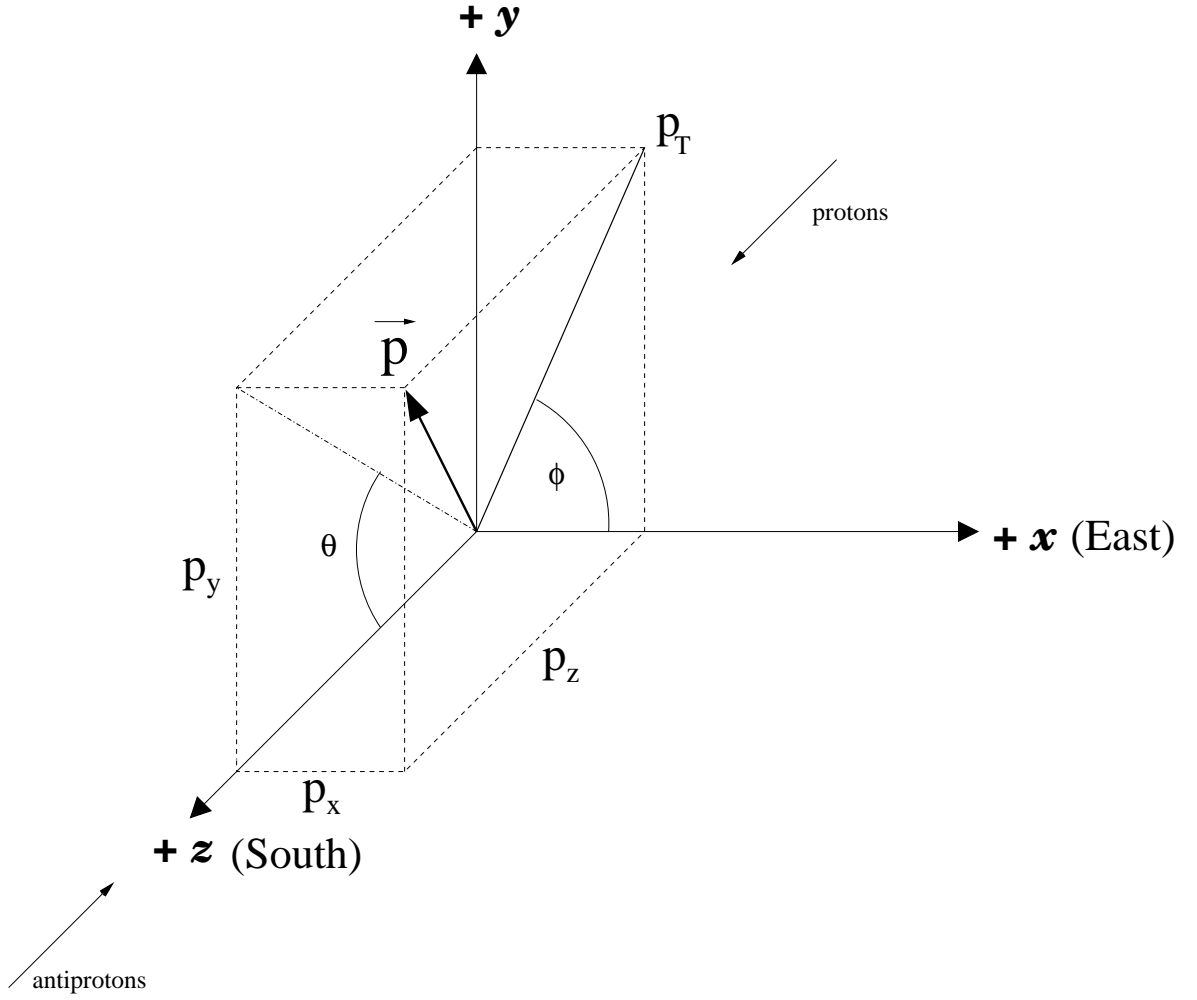
Figure 2.5. DØ coordinate system

The rapidity is invariant under boosts in the z-direction. Solid angles $\triangle R$ expressed in terms of ϕ and η :

$$\triangle R = \sqrt{(\triangle\phi)^2 + (\triangle\eta)^2}$$

are invariants in the high energy limit.
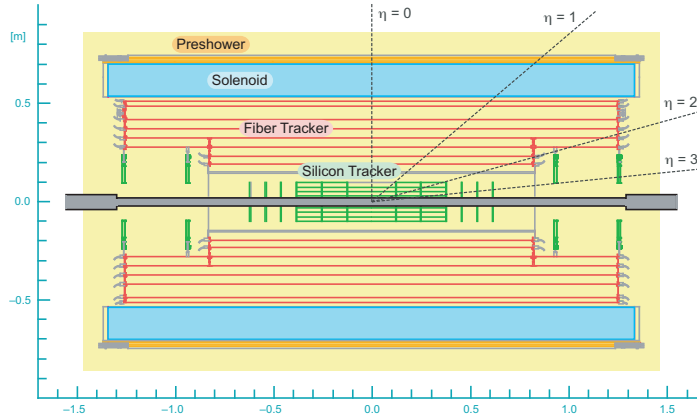
Figure 2.6. The DØ tracking system

Tracking

In Run I, the DØ tracking system consisted of a central transition detector and drift chambers in the central and forward regions. The Run I tracking did not provide momentum measurement of the tracks due to the lack of magnetic field. In Run II, these detectors were replaced with a silicon microstrip detector, a central fiber tracker, a superconducting solenoid, and preshower detectors. Schematic view of the DØ tracking system is shown on Figure 2.6.

The Silicon Microstrip Tracker: The subsystem closest to the Tevatron beam pipe is the Silicon Microstrip Tracker (SMT). An illustration of the Silicon Microstrip Tracker is shown on Figure 2.7. It is made of disks and barrels. Both disks and barrels have silicon strips with very fine cathode lines formed on their surfaces. These detectors are solid state devices. When a charged particle passes through them, it deposits a small amount of energy in the form of ionization. Electron-hole pairs produced from ionization are collected at the nearest cathode producing an electric signal. Cathode lines are spaced very closely allowing accurate measurement of the
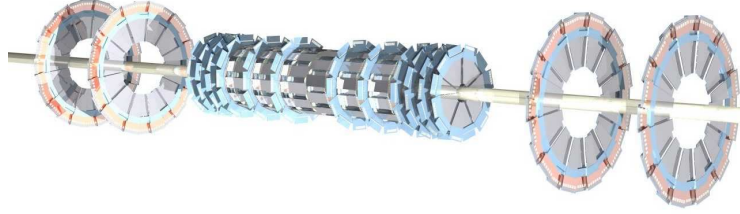
Figure 2.7. Silicon Microstrip Tracker

position at which the particle passed through the detector. By combining hits from different disks and barrels, tracks can be reconstructed. The position and layout of the silicon detectors is dictated by the structure of proton/anti-proton bunches which have a gaussian distribution in the z-direction with $\sigma_z = 28$cm. Such a large σ_z makes it impossible to design an arrangement of the detectors so that particles pass through them perpendicular to their surface for all η. A hybrid layout, where large $|\eta|$ tracks are predominantly reconstructed by the disks shown on Figure 2.7, was implemented. The main part of the structure is a set of 6 barrels. Each barrel has a length of 12.4 cm and contains four concentric layers with radii ranging from 2.6 cm to 10.0 cm. Layers 2 and 4 of all barrels have double-sided small-angle (2 degree) stereo detectors with a 62.5 μm pitch. Layers 1 and 3 are double-sided large-angle (90 degree) ladders with a 153.5 μm pitch. Layers 1 and 3 of the two outermost barrels have single-sided layers with strips in the axial direction at two degree to the axial and 50 μm pitch. Eight "F" disks are interspersed with the barrels. Each "F" disk is made of 12 double sided silicon wedges with ± 15 degree stereo pitch. Four larger disks called "H" disks are located further from the $z = 0$ point on both sides of the detector. Each "H" disk consists of 24 single sided wedges. The "H" disks extend the tracking coverage to $|\eta| = 3$.

The Central Fiber tracker: The SMT is surrounded by the Central Fiber Tracker (CFT) [5]. The CFT complements the SMT track reconstruction and, by measuring the tracks curvature in the magnetic field of 2 Tesla, allows the measurement of the charge and transverse momentum of charged particles coming from the interaction. The CFT also provides Level 1 triggering for $|\eta| < 1.6$.

The CFT consists of 76800 scintillating fibers forming concentric ribbons supported by cylinders made of carbon fiber (see Figure 2.8). There are eight cylinders of CFT. Each one of them contains two doublet layers of axial and stereo fibers. The axial layer fibers are parallel to the beam direction, whereas stereo layers have stereo pitch of three degrees. Each doublet layer consists of two mono-layers. To compensate for the gaps between adjacent fibers, mono-layers are offset by one half of the fiber spacing. This layout, as well as the measured position resolution, is shown on Figure 2.9. The radial size of the CFT cylinders ranges from 20 to 51 cm. The two inner cylinders are 1.7 m long, the remaining 6 cylinders are 2.5 m long. The space resulting from this length difference is occupied by the H-disks of the silicon microstrip detector.

The CFT scintillating fiber consists of a 775 μm diameter scintillating core and two layers of cladding, each 15 μm thick. The scintillating core is made of polystyrene doped with 1% P-terphenyl and 1500 ppm 3-hydroxyflavone. This scintillator has an emission maximum at 530 nm [6]. The first cladding is made of acrylic and the second one of fluoro-acrylic material. At one end of the scintillating fibers, an aluminum mirror coating reflects light back into the fiber. The other end is used for readout. Ribbons consisting of 256 scintillating fibers are inserted into custom-made optical connectors which couple scintillating fibers to the clear fiber optic waveguides which carry light to the photo-detectors. Clear fibers are made from the same material as scintillating fibers, the only difference is that

they do not contain fluorescent dyes. The ends of both scintillating and clear fibers are diamond-polished in order to maximize the amount of light transmitted to the photo-detectors.

VLPC cassettes: Wave guides which range in length from 7 to 12 meters transport light from the scintillating fibers to VLPC cassettes shown on Figure 2.10. Each of these cassettes contains the waveguides to transmit the light signal from 1024 CFT channels to the arrays of visible light photon counters (VLPCs), a silicon-avalanche based photon detector [6]. These detectors convert the photons to an electrical signal with a high quantum efficiency of over 80 percent and a gain in the range of 20,000-50,000. The VLPCs can sustain event rates of at least 20 MHz and have a noise rate below 0.1 percent. Typical VLPC spectra from the CFT calibration run are shown on Figure 2.11. The optimal operating temperature of the VLPCs is approximately 9 K. Before the cassettes were assembled, the VLPCs were tested and grouped according to their operating temperature and gain. Because axial channels are used for triggering, the VLPC chips with the highest gain were used for axial layers. Also, the waveguides used in the CFT have different lengths, so in order to compensate for the greater attenuation of the waveguides with longer length, the best VLPC were selected for the channels with longest waveguide length. The VLPC chips are located at the bottom of the cassettes within a cryostat held at 6 K. Resistive heaters mounted near the VLPC chips allow controlling of the temperature of the VLPC chips. Electrical signals from the VLPC chips are sent via flexible cables to the readout electronics which occupy the upper part of the cassette at room temperature. The mechanical design of the cassette is complicated by the need to keep the bottom part at low temperature. Analog signals from VLPCs are sampled by so called SIFT discriminator chips, which provide information for
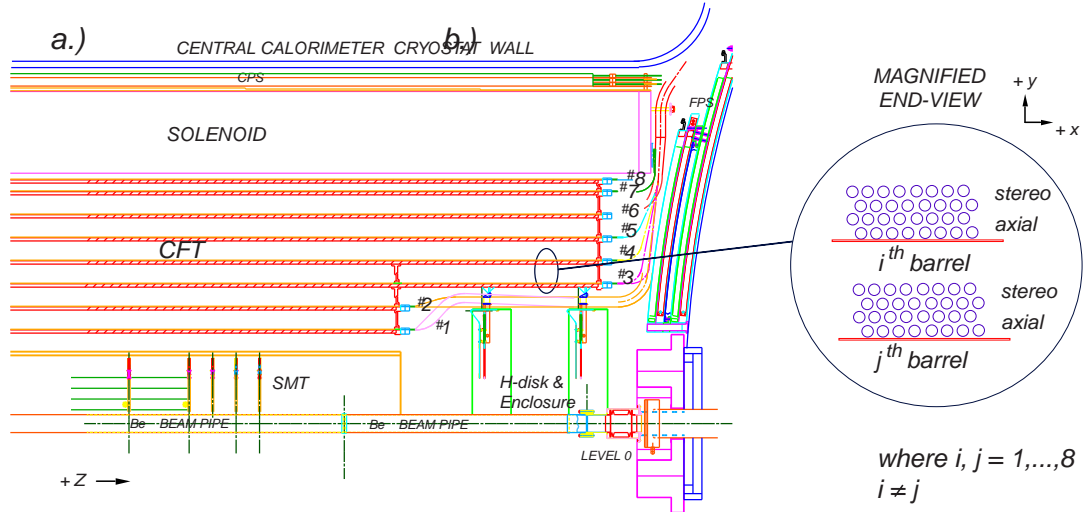
Figure 2.8. A quarter $r - z$ view of Central Fiber Tracker

the Level 1 trigger system. The VLPC signal is also sent to a Silicon VerteX (SVX) chips. SVX chips have analog pipelines for storing up to 32 beam crossings. If the trigger system issues an accept, then the SVX chips digitize analog signal and send it out along with information about SIFT hits.

Preshower Detectors

Beyond the tracking system and prior to the calorimeter are the preshower detectors [7]. They were added during the DØ detector upgrade for Run II. Preshower detectors are important for the following reasons:

- The position measurement in the preshower detector allows a better matching of the tracks in the tracking system to the objects in calorimeter.

- The preshower detector adds an extra layer of calorimeter with very fine segmentation which provides early sampling for particles which just passed through the solenoid.

- The shape of the preshower clusters helps in identification of electrons, photons (single cluster), and π^0 (two cluster close together).

25
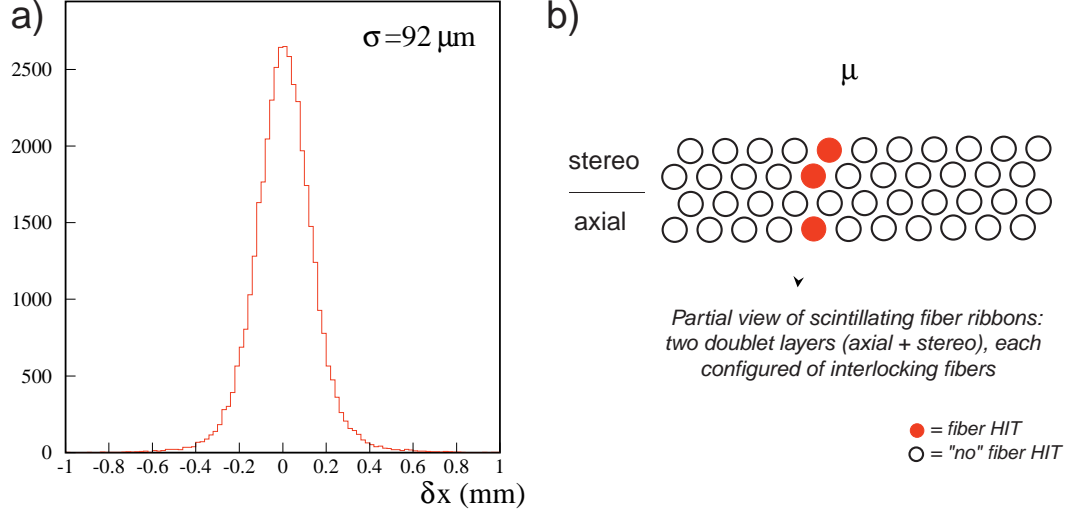
Figure 2.9. a) The position resolution distribution measured in the CFT cosmic ray test stand. b) Illustration of doublet ribbon configuration of CFT.

The preshower detector in the central region is called the Central Preshower Detector (CPS). Figure 2.12 shows the geometry of the detector. It consists of three layers of triangular strips made from scintillating material. The innermost layer is aligned along the z-direction, whereas the remaining two form stereo-layers at ± 23 degree angles. A layer of lead located between the solenoid material and the CPS layers increases the probability that an electron or photon will develop a shower before the detector. Every scintillating strip has a hole containing a wave-shifting fiber. Scintillating light from the CPS strips is wave-shifted and transmitted by clear fibers to the VLPC cassettes in the same way as for the CFT. There are a total of 7680 channels in the CPS which, from the readout point of view, form a ninth layer of the CFT.

The forward regions ($1.4 < |\eta| < 2.5$) are covered by Forward Preshower Detectors (FPS) [8]. The detector configuration is shown in Figure 2.13. It consists of four layers of scintillating strips separated by a layer of lead. There are two layers

Figure 2.10. Diagram of VLPC Cassette
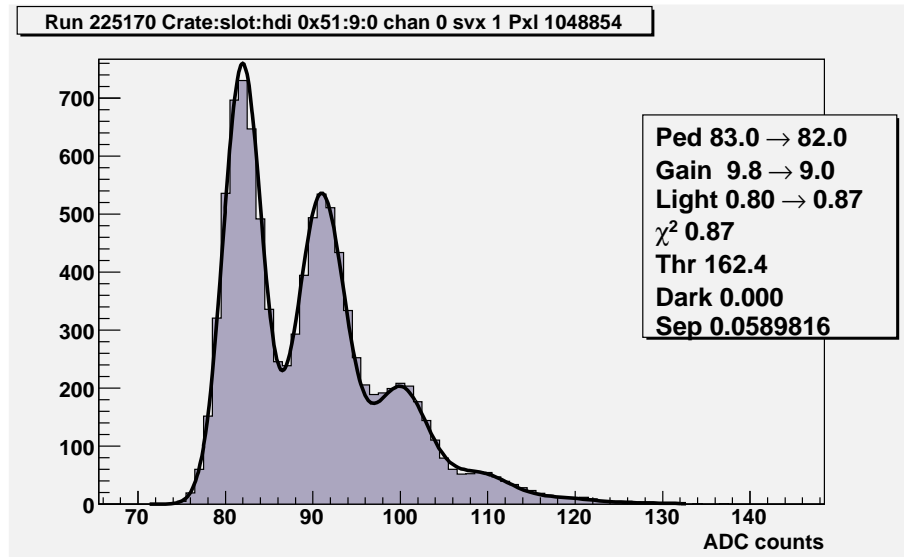
Figure 2.11. Typical VLPC spectra from the CFT calibration run

before the lead and two after. The innermost layers of the FPS are referred to as Minimum Ionizing Particle (MIP) layers, since there is not much material between the interaction region and these layers. The two outer layers are referred to as shower layers. The FPS layers are aligned at different pitches allowing reconstruction of three-dimensional position before and after showering. The readout of the FPS system is identical to the CPS and FPS.

The Calorimeter

The most important part of the DØ detector is the calorimeter. With the exception of the readout electronics, the DØ calorimeter has remained the same since Run I. It is a liquid argon-uranium sampling compensating detector. The main function of the DØ Calorimeter is to measure the energy of the particles and to provide the shower shapes for particle identification. The calorimeter is also used for triggering.

Electrons and photons passing through the calorimeter interact with the uranium

28

a.)

CC

CPS

SOLENOID

η=1.28 (31.0°)

η=1.40 (27.7°)

η= 1.6(25.16°)

FPS

η=2.50 (9.39°)

LEVEL 0

b.)

STEREO V

STEREO U

AXIAL

PRESHOWER
ASSEMBLY

CC

CPS

SOLENOID

CFT

END VIEW
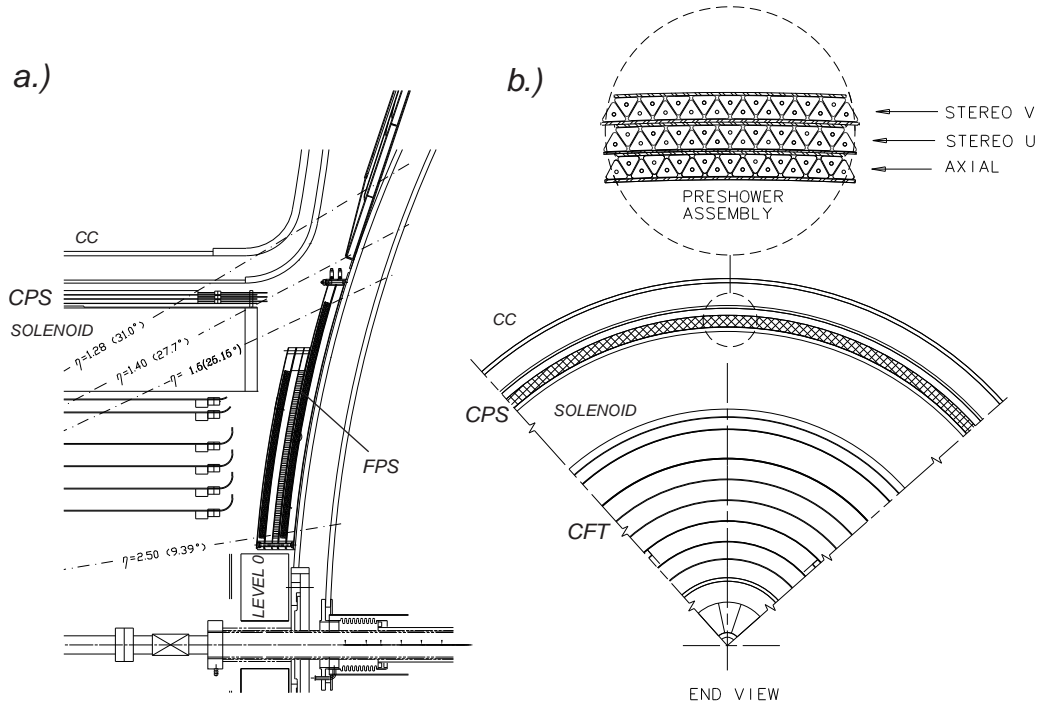
Figure 2.12. a) a $r - z$ semi-quarter view of the CPS detector. b) Cross-sectional $r - \phi$ view of the CFT and CPS detectors. The inset shows a magnified view of the nested triangular strips and layer geometry for the CPS. Adapted from [4].

29

LEAD 5.5mm

CC CRYOSTAT WALLS

ICD CHAMBER

ENDCAP CRYOSTAT WALL

CONNECTORS

CC

CPS

LEAD–SS–LEAD (11mm)

FPS

SOLENOID MAGNET

η=1.25 (31.0°)

η=1.40 (27.7°)

η=1.5(25.15°)

12.0

1 layer fiberglass cloth (0.3mm)

5.4   5.4

1 layer fiberglass cloth (0.3mm)

2.7 in.

"V" – LAYER

1.5 in.

η=1.65 (21.7°)

7.46

"U" – LAYER

EC

2 layers fiberglass cloth (0.6mm)

CFT

2.0 GAP

16.0 LAYER

η=2.50 (9.39°)

DIMENSION IN (mm)

LEVEL "0"

SCINTILLATOR LAYERS

SMT

$\overline{p}p$ beam (Beryllium Pipe)

+z

Figure 2.13. One quarter $r - z$ view of the FPS detector.The inset shows $u - v$ scintillator layers. Adapted from [4].

absorber primarily through bremsstrahlung ($e \to e\gamma$) and pair production ($\gamma \to e^+ e^-$) processes. Each interaction multiplies the number of particles, while the energy of the resulting particles decreases. The energy of the particles has a negative exponential dependence on the distance: $E(x) = E_0 e^{-x/X_0}$, where x is the distance a particle traveled in the media, E_o is the initial energy of the particle, and X_o is the radiation length of media (in our case it is uranium: $X_0 = 3.2$ mm [9]). Charged particles leaving the absorber ionize liquid argon atoms, resulting in an electric charge which is then collected by high voltage electrodes in each calorimeter cell.

Hadrons are much heavier than electrons, suppressing the bremsstrahlung process. As a result, the main interaction with the absorber media happens via the strong force. In this case, the secondary particles are hadrons; one third of them are neutral pions (π^0) which decay electromagnetically and produce subsequent electromagnetic showers. The rest of the secondary particles interact strongly. Strong interaction processes have smaller cross-section than electromagnetic; therefore, it takes a longer distance for the hadronic shower to develop. The nuclear radiation length (λ_0) for uranium is 10.5 cm [9]. This difference between electromagnetic and hadronic showers allows us to distinguish between electromagnetic and hadronic particles.

The idea behind a compensating calorimeter is to equalize the calorimeter response to hadrons and electrons. This is achieved by tuning the thickness and type of the absorber material. Copper, steel, and depleted uranium are used as absorbers, while liquid argon serves as an active medium. A schematic view of the DØ calorimeter is shown on Figure 2.14. To allow access to the central regions of the detector, the calorimeter is split into three vessels, a Central Calorimeter (CC) and a pair of end calorimeters , EC South and EC North. The CC covers the $|\eta| < 1.2$

region and the EC extend the calorimeter coverage up to $|\eta| = 4.5$. Within each vessel, the calorimeter is segmented into three sections, the electromagnetic section (EM), the fine hadronic section (FH), and the coarse hadronic section (CH), with EM being closest to the collision point where FH is farthest. The EM sections are divided into four separate layers EM1, EM2, EM3, and EM4. Each EM layer uses 3 or 4 mm thick depleted uranium plates as an absorber. The FH section consists of three or four layers with 6 mm thick uranium-niobium alloy plates as an absorber. The CH section has only one layer made of 46.5 mm thick plates of copper for the CC and stainless steel for the EC. Table 2.1 shows the depth of calorimeter layers expressed in units of radiation length (X_0) and absorption length (λ) [10].

From the readout point of view, layers are represented as a set of readout cells. Typical size of the cells is 0.1×0.1 rad^2 in $\eta \times \phi$. However, the EM3 layers have finer segmentation of 0.05×0.05, which allows better measurement of the EM shower centroid. Cells from different layers aligned along the outward direction make a tower (Figure 2.15 illustrates this geometry). For the trigger system, the calorimeter towers are summed up into 0.2×0.2 in $\eta \times \phi$.

A schematic view of a calorimeter readout cell is shown on Figure 2.16. As one can see from the illustration, the gap between the absorber plates is filled with liquid argon. Charged particles from the shower ionize the argon creating electron and ions. In the presence of a strong electric field, electrons are collected on electrodes. Metal absorbers serve as ground cathodes and resistive coating on the readout board serve as anodes. Charge collected on the anode induces a charge on the readout pads via capacitive coupling. Readout pads are made of copper and isolated from the anodes by 0.5 mm plates of G10 plastic.
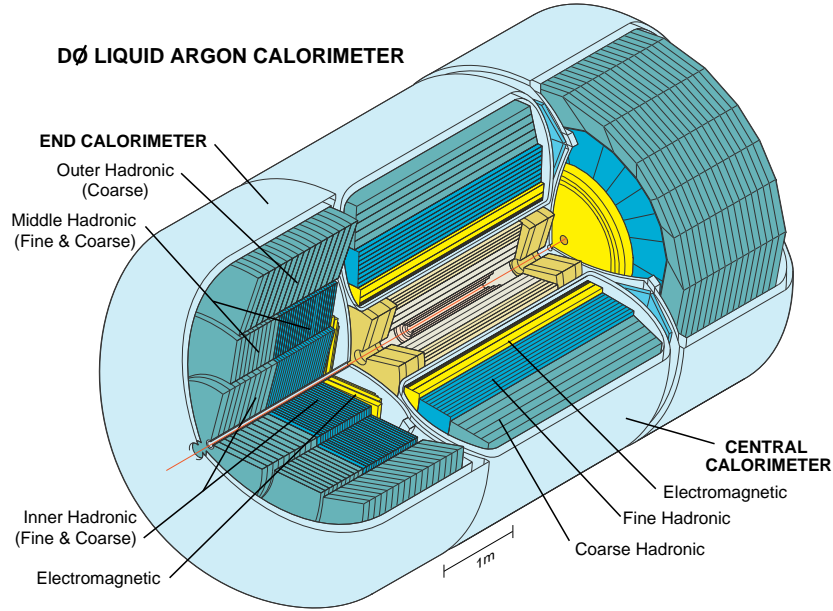
Figure 2.14. The DØ calorimeter. Adapted from [4].

Intercryostat and Massless Gap Detectors: The region of the detector between CC and EC vessels ($1.1 < \eta < 1.4$) contains a large amount of uninstrumented material such as calorimeter support, cabling, and cryostat walls. To help instrument this region, scintillating detectors were mounted on the face walls of each EC. Each intercryostat detector (ICD) has 386 scintillating tiles which match the calorimeter towers. Also, there are separate single calorimeter-like readout cell structures called massless gaps mounted in the EC and CC calorimeters. The ICD and massless gap detectors complement the standard calorimeter for this special region.

Muon System

The outermost layer of the DØ detector is the Muon System. Muons are ~ 200 times heavier than electrons and lose much less energy due to the Bremsstrahlung scattering. Muon energy loss in the DØ Detector material is about 3 GeV. Therefore,
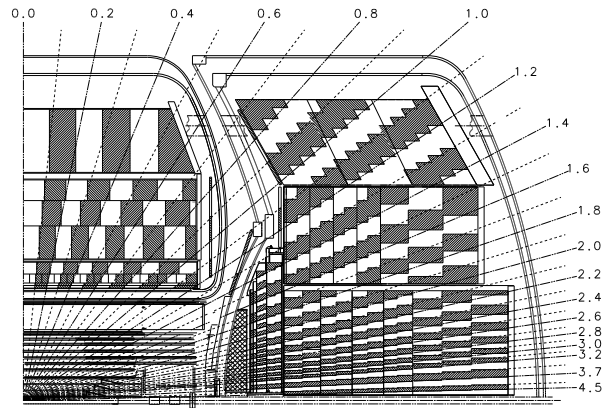
Figure 2.15. A one quarter $r - z$ view of the calorimeter adapted from [4].
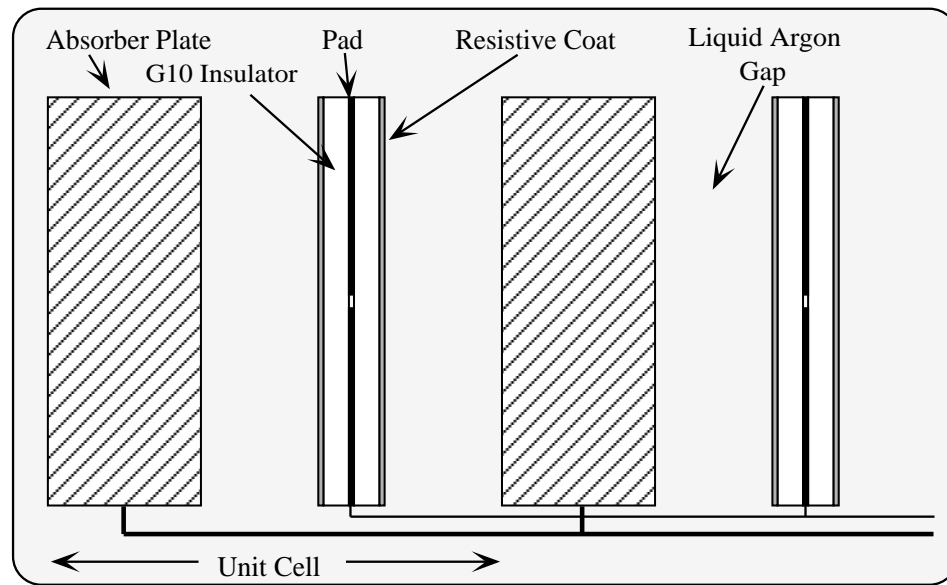
Figure 2.16. Calorimeter unit cell. Adapted from [10]

TABLE 2.1

DEPTH OF THE DIFFERENT CALORIMETER LAYERS

	EM	FH	CH
CC Depth	2, 2, 7, 10 X_0	1.3, 1.0, 0.9 λ	3.2 λ
EC Depth	0.3, 2.6, 7.9, 9.3 X_0	1.2, 1.2, 1.2 λ	3.6 λ

muons above this threshold can pass the detector and reach the Muon System where they can be registered. The Muon System is composed of scintillator (used for time measurement) and proportional drift tubes (used for fine position measurement).

Geometrically, the Muon System is divided into two parts (see Figure 2.17): The $|\eta| < 1$ region is covered by the Wide Angle MUon Spectrometer (WAMUS), whereas the $1 < |\eta| < 2$ region is covered by the Forward Angle MUon Spectrometer (FAMUS).

WAMUS: The WAMUS consists of three detector layers labeled as A, B and C (see Figure 2.17). An iron toroid of 1.9 Tesla, located between the A and B layers, provides local muon P_T measurement and absorbs nearly all the other particles which managed to exit the calorimeter volume. Each of the three layers consists of proportional drift tube (PDT) chambers and scintillators. Scintillators provide time measurement and PDTs provide accurate position measurement. PDT chambers are composed of decks of extruded aluminum tubes. The A-layer contains four decks of tubes, while the B-layer and the C-layer contain only three decks of tubes. One chamber contains around 24 PDTs which are 10.1 cm wide and 5.5 cm high. Anode wires inside the PDT are oriented along the magnetic field providing a measurement of the amount of bending of muon tracks in the toroid magnetic field. Two vernier

pads along the top and bottom of the tube serve as cathodes. PDTs contain non-flammable gas mixture of 80% argon, 10% CH_4 and 10% CF_4. This mixture have drift velocity about $10\,cm/\mu s$, with a maximum drift time of 500 ns [11]. Coordinate uncertainty due to the diffusion is about 400 microns.

There are two types of scintillator counters in the WAMUS, the A-ϕ scintilator counters and the Cosmic Caps scintillators. The A-ϕ scintilator counters cover A-layer of the PDTs and located between the calorimeter and the toroid. They are segmented into tiles of 4.5 degrees along ϕ direction and 85 cm along z direction. The signal readout consists of wave-shifting fibers coupled to the photo-multiplier tubes (PMT). The time resolution of the counters is about 4 ns [11]. Precise time measurement allows us to reject out-of-time cosmic muons, the fast signal from the scintillator counters is also used for the triggering. Cosmic Cap scintillators cover the B-layer and C-layer of the PDTs. Top and sides of Muon System are fully covered, whereas bottom coverage is only partial. The time resolution of these counters is ~ 5 ns [11] but offline corrections improve it to approximately 2.5 ns.

FAMUS: The FAMUS is also made of three layers called A, B and C (see Figure 2.17). Each layer consists of mini-drift tube (MDT) sections and scintillation pixel counters. MDTs, compared to PDTs, have a smaller cross-sectional area and are better suited for the high occupancy in the forward area of the detector. The MDT sections are made of three or four planes of tubes. The A-layer consists of four planes, the B-layer and the C-layer have three. The $r - \phi$ view of one plane of mini-drift tubes is shown on Figure 2.18. Each MDT plane is divided into eight octants and consists of tubes, each having eight cells. Tubes are filled with a gas mixture of 90% CF_4 and 10% CH_4. The maximum drift time for that mixture and operating voltage of 3.1 kV is 60 ns. The position resolution is around 0.7 mm [11].

The FAMUS scintillator pixel counter configuration is shown on Figure 2.19. The ϕ segmentation is 4.5 degrees. The η segmentation is 0.07 for three inner circles and 0.12 for the eight outer circles.

Trigger and Data Acquisition

Proton and anti-proton bunches cross each other approximately every 396 ns, or at the rate of 2.5 MHz. It is impossible for the detector to read out and record events at such a high rate. Most of the events coming from $p\bar{p}$ collisions are low transverse momentum, non-diffractive $p\bar{p}$ and parton scattering. These processes have been extensively studied in the past and are not interesting any more. The experiment must be triggered only if an event has signatures of interesting physics (for example the Higgs signature) produced at the collision. The DØ Trigger system is organized in three layers of logic (L1, L2, and L3). To get recorded, an event has to pass successively all three trigger levels. The DØ trigger layout and typical rates at different levels are shown on Figure 2.20.

The Level 1 trigger system logic is based on the simple algorithms implemented in Field Programmable Gate Arrays (FPGAs). Level 1 FPGAs process raw information from different detector systems in parallel, as shown on Figure 2.21. At this stage, the event rate has to be reduced from the beam crossing rate to approximately 1 kHz. If some L1 term is found to have a rate which is too high, it may get prescaled. Prescaling reduces the rate at which a certain L1 trigger may fire by only allowing triggers from some predetermined number of crossings. For example, a prescale of ten will randomly select one out of ten triggers from the Tevatron bunch crossings.

Level 2 (shown on the same Figure 2.21) correlates hits from different sub-detectors and constructs physics object candidates, such as muons and electrons. The L2 system physically consists of 500 MHz Alpha processors residing in VME

FORWARD
TRACKER (MDTs)

PDTs

MUON
TORIOID

NORTH

CENTRAL
TRIG
SCINT
(A-φ)

5

SHIELDING

P →

(m) 0

FORWARD
TRIG
SCINT
(PIXELS)

TRACKING
SYSTEM

−5

PLATFORM

BOOTOM B/C SCINT

−10   −5   0

(m)
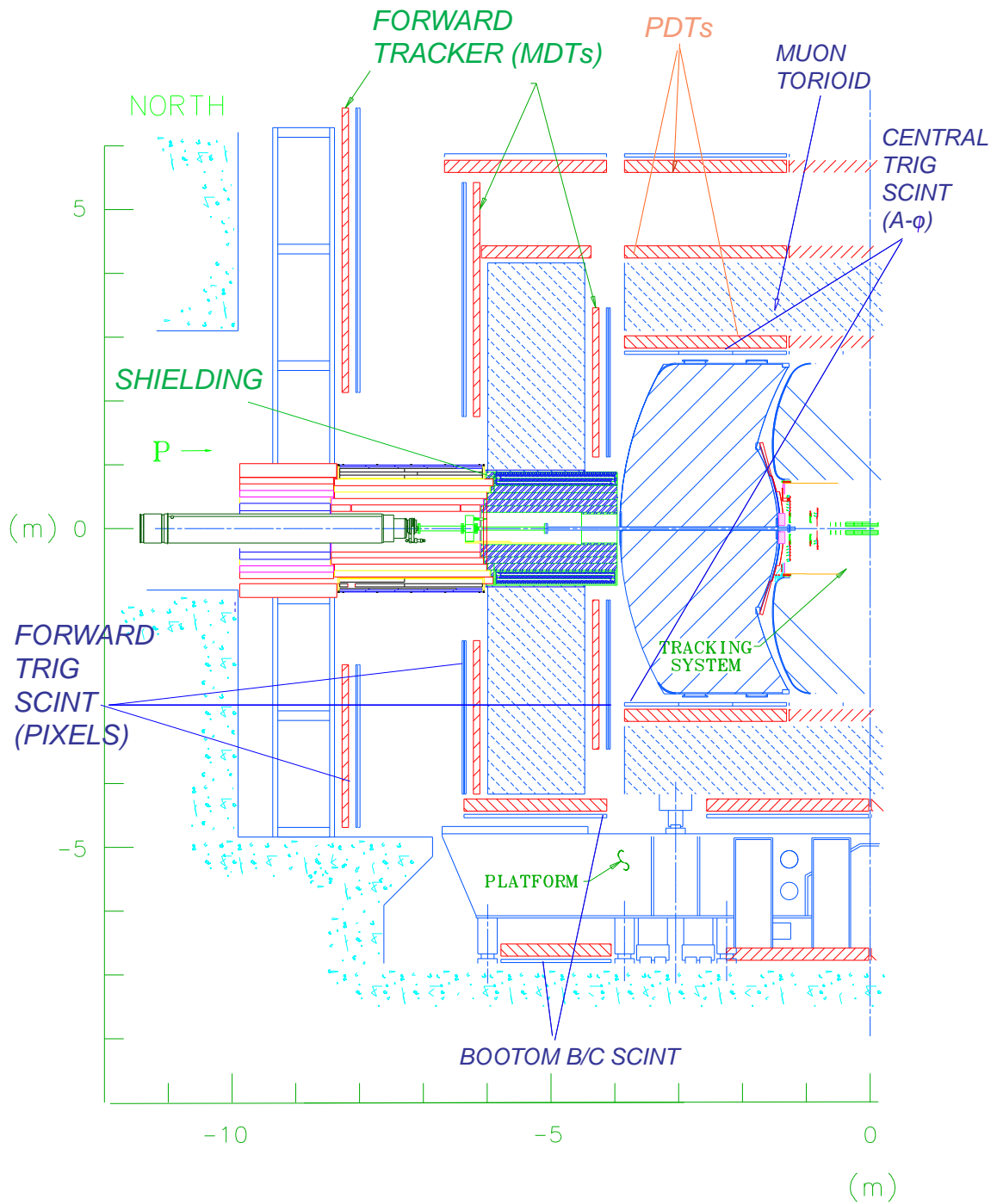
Figure 2.17. A $r - z$ half-view of Muon System
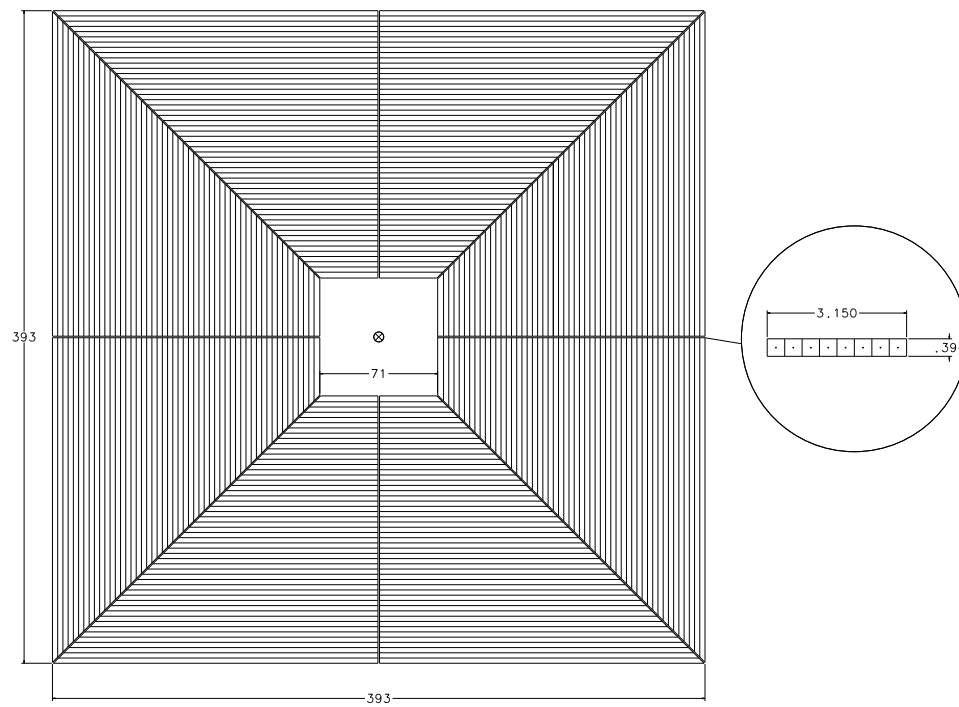
Figure 2.18. $r - \phi$ view of one plane of mini-drift tubes.
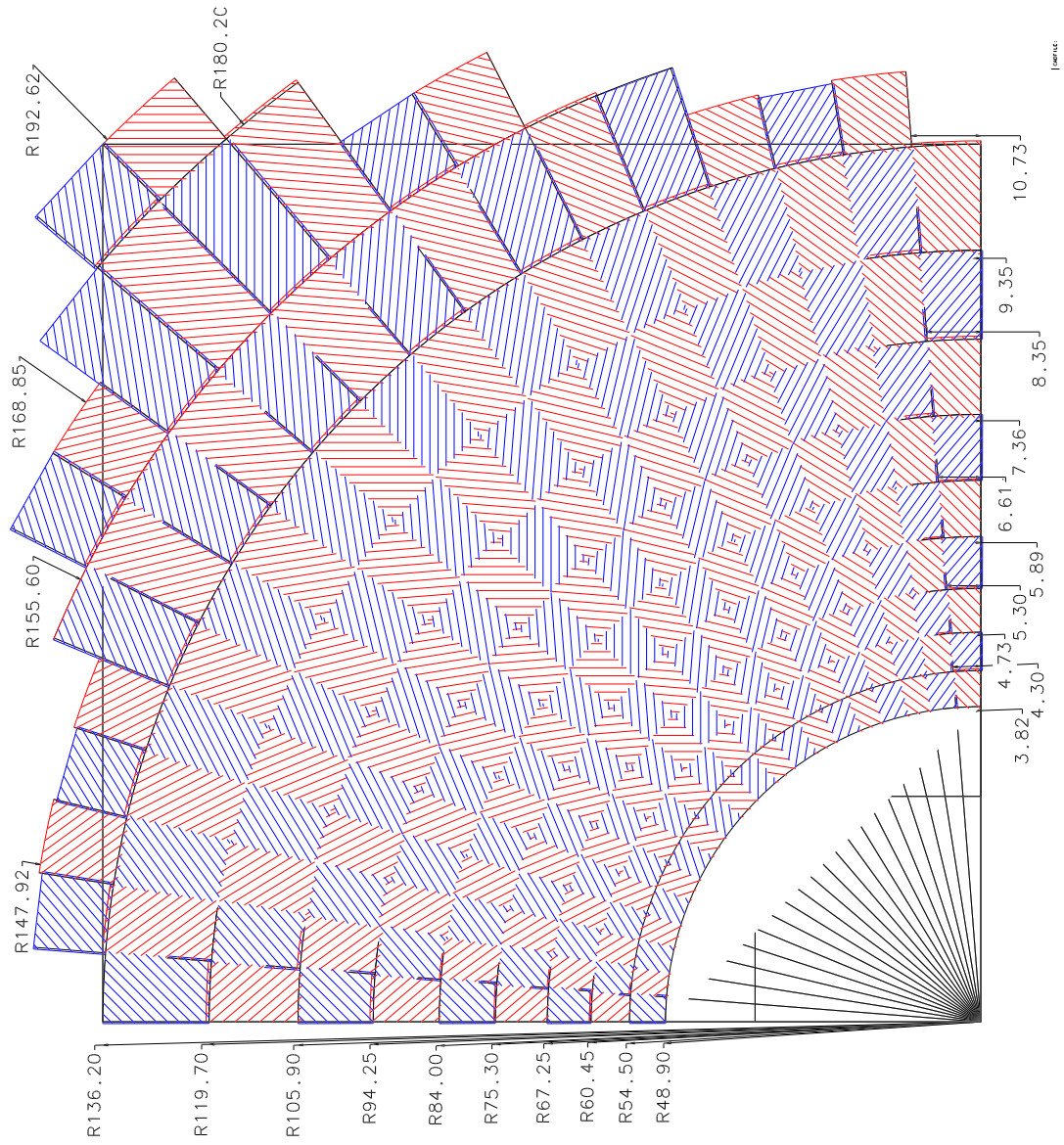
Figure 2.19. An $r - \phi$ view of the FAMUS scintillator pixel counters is shown.
Adapted from [4]

7 MHz:
Lum = 2 x 10^{32}cm^{-2}s,$^{-1}$
396 ns → 132 ns crossing time

L1
4.2 µs   L1: HARDWARE

FRAMEWORK

5-10 kHz
128 bits

L2
100 µs   L2: HARDWARE

1 kHz
128 bits

L3
100 ms
50 nodes   L3: SOFTWARE

• *Maintain low- & high-p$_T$ physics*
• *Implement fast algorithms,*
  parallel processing, pipelining/buffering
• *Trigger Deadtime < 5%*

50 Hz

TO DAQ &
TAPE
STORAGE
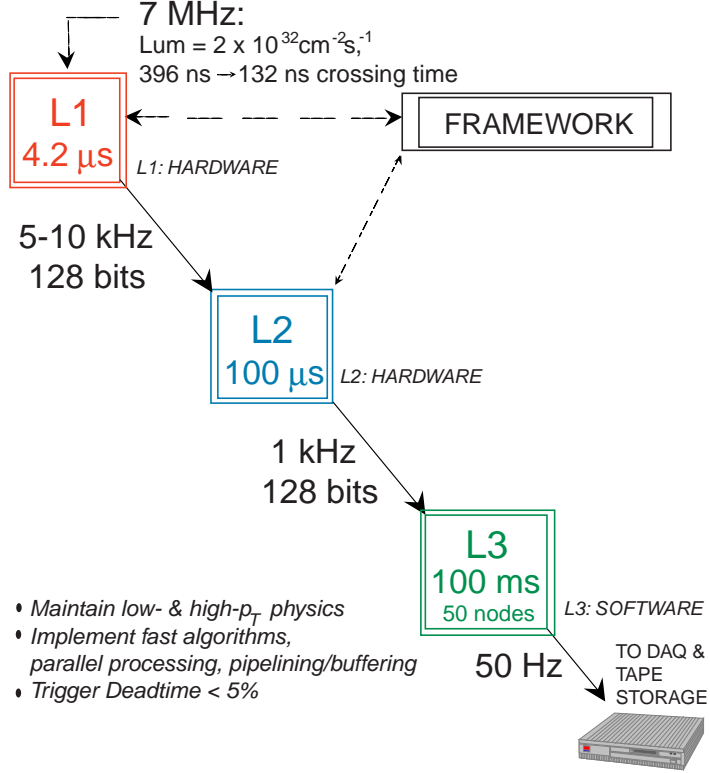
Figure 2.20. The DØ trigger layout and typical trigger rates. Adapted from [4].

crates on a VME bus, running Linux and using custom built Magic Bus interfaces for 320Mb/s data handling [10].

The next stage is L3/Data Acquisition System (DAQ). Whenever the Trigger System issues L2 'accept', the full data readout occurs. Information from all detector systems is collected by L3/DAQ. A schematic view of the L3/DAQ system is shown on Figure 2.22.

There are about 70 readout crates (ROCs), each of which corresponds to a section of sub-detector or trigger framework. Every ROC has a Single Board Computer (SBC), which is powered by 933 Pentium III processor with 128 MB of RAM. SBCs read out their crates and send information with typical size of 1-10 KB through the
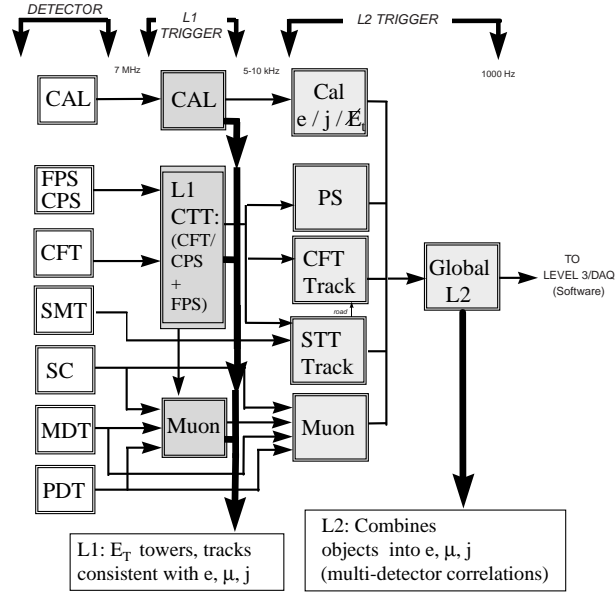
Figure 2.21. Level 1 and Level 2 trigger data flow illustration. Adapted from [4].
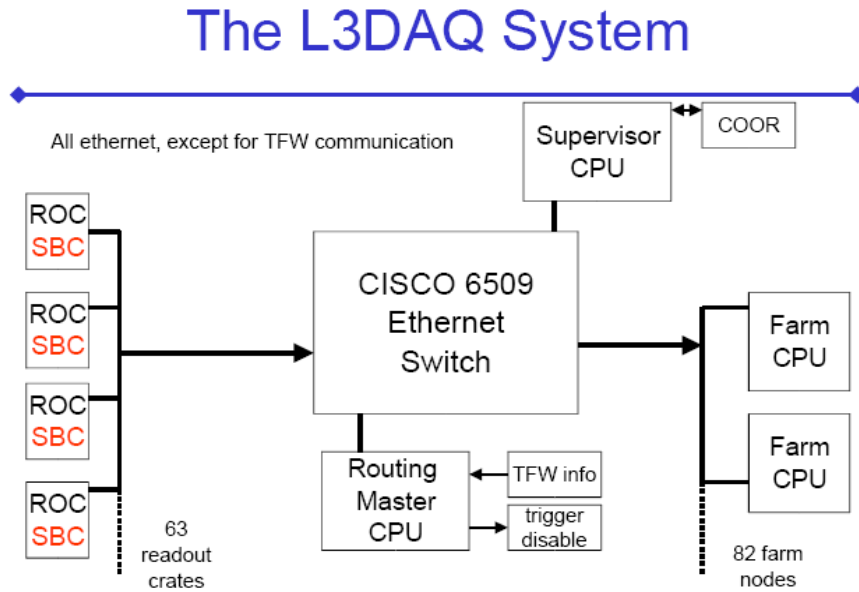
Figure 2.22. The L3 and DAQ system layout. Adapted from [10].

CISCO 6509 ethernet switch to one of the nodes of the L3 processor farm. The L3 processor nodes build complete events, perform fast reconstruction, and run a series of software filter tools. Each filter tool has a specific function related to the identification of a certain physical object (such as Jet, muon, EM object, tracks) or event characteristic (for example, scalar E_T, missing transverse energy) or some interesting event topology. Events which pass the L3 physics criteria are sent to the tape for the offline analysis.

Other types of events which get selected at L1 and subsequently recorded to the tape are zero-bias and minimum-bias events. The zero-bias trigger does not require anything and simply reads out the detector at crossing clock (at prescaled rate). The minimum-bias trigger requires some activity in the luminosity system. Such events have been shown to be very useful for examining the calorimeter data quality.

CHAPTER 3

RECONSTRUCTION ALGORITHMS

A description of reconstruction algorithms used at DØ is presented here. The goal of this chapter is not to give a full description of the algorithms, many of which are quite complicated and lengthy, but rather to give a short overview of common reconstruction algorithms and definitions of different quantities and objects used later in the analysis.

3.1 Muon Identification

Hits in the muon system are used for muon reconstruction. A combination of hits in the muon wire chambers is used to fit a straight line, called a segment. Then, segments from different (A,B and C) layers are matched with each other constructing a muon track (see [12] for detailed description of segment algorithm). The muon track is assigned a *nseg* (numbered segment) value, based on the set of layers which have hits. The correspondence between muon system layers being hit and *nseg* is shown in Table 3.1. Also, the *nseg* is assigned a sign. Muons with central track match have a positive *nseg*, whereas muons without central track match have negative *nseg*. In this analysis we require muons to have a central track match.

The DØ muon reconstruction algorithm defines three different muon qualities, loose, medium, and tight [13]. The definition of muon qualities is shown in the Table 3.2. In this analysis we use loose quality muons.

TABLE 3.1

MUON SYSTEM HIT CORRESPONDENCE TO *NSEG.*

nseg	Muon System layers being hit
3	A and BC-layer
2	BC-layer
1	A-layer
0	Any muon system hit

TABLE 3.2

DEFINITIONS OF *LOOSE, MEDIUM,* AND *TIGHT* MUONS

	nseg=3
medium	At least two A-layer wire hits A-layer scintillator hit At least two BC-layer wire hits At least one BC-layer scintillator hit
loose	*medium* but allow one of the criteria to fail
	nseg=2
medium	*loose* + located in the bottom part of the detector with $|\eta_d| < 1.6$
loose	At least one BC-layer scintillator hit At least two BC-layer wire hits
	nseg=1
medium	*loose* + located in the bottom part of the detector with $|\eta_d| < 1.6$
loose	At least one A-layer scintillator hit At least two A-layer wire hits

3.2   Jet Reconstruction

Jets are narrow cones of hadrons produced by the hadronization of the quarks or gluons created in the collision. The goal of the jet reconstruction is to find jet properties, such as p_T, η, and ϕ which can be compared to the properties of the initial quark or gluon.

3.2.1   Run II Cone Algorithm

The Run II "improved legacy cone algorithm" [14] is used for the jet reconstruction in data and Monte Carlo. The algorithm starts with finding jet "seeds". For each calorimeter tower, the transverse energy (E_T) is calculated using the total energy in the tower and the polar angle θ between the tower center and the beam axis, as seen from the primary vertex. Then, calorimeter towers with $E_T > 0.5$ GeV and total energy within an $R < 0.3$ cone greater than 1.0 GeV are used to form jet seeds. In the next step, the E_T within $R < 0.5$ around the seed center is calculated. The weighted center of the cone is also calculated. The new cone center is used for the next iteration. This process continues until the cone center becomes stable. Stable cones are called proto-jets. Proto-jets with $E_T > 8$ GeV are checked for overlaps; that is, if the overlap region region between two proto-jets contains more then half of proto-jet E_T, this proto-jet gets merged with the overlapping jet. The merged jet energy and position are consequently recomputed. Otherwise, the jets are split with towers being added to the closest cone, and the jet energies and positions are recomputed.

3.2.2   Jet Quality Quantities

To separate the real jets from the noise, the following quality quantities are used:

- EM Fraction: The fraction of the transverse energy deposited in the EM part of the calorimeter.

46

- Coarse Hadronic Fraction (CHF): The fraction of the transverse energy deposited in the Coarse Hadronic layer of the calorimeter.

- Hot Fraction: The ratio of the transverse energy of the most energetic cell to that of the next most energetic cell.

- n90: smallest number of towers which contain 90% of the jet energy

- f90: defined as n90/n_{item}, where n_{item} is the number of towers in the jet.

3.2.3 Jet Energy Scale

The energy scale of a jet is determined from data events which have a jet back-to-back with a photon. In this method, the jet energy is determined by requiring a balance between the photon and jet energies. The energy scale of the EM part of the calorimeter is set by using the Z boson mass. Jet Energy Scale corrections are defined for jets with $|\eta| < 2.5$ and $E_T > 15$ GeV. At low transverse energies, these corrections and their uncertainties are quite large. Since the jets used in this analysis have low transverse energies the Jet Energy Scale is a large source of uncertainty.

3.3 Missing transverse energy reconstruction

The missing energy is the energy which is expected (due the energy-momentum conservation law) but not detected in the detector. The missing energy is attributed to particles which escape the detector without interaction. The specifics of hadron colliders are such that the initial momentum of the colliding partons (quarks and gluons) along the beam axis is not known. This is due to the composite structure of the proton. The energy of the proton is constantly redistributed among its constituents and the total amount of the missing energy cannot be determined. However, transverse component of the initial energies of the partons is close to the zero, so any non-zero net momentum in the transverse direction indicates Missing Transverse Energy ($\not{E}_T$). Often, the missing transverse energy is due to the presence

of neutrinos in the particle decay. Also, missing transverse energy could indicate new physics.

The missing transverse energy is reconstructed by summing up the energy on a cell by cell basis:

$$\displaystyle{\not}E_{Tx} = -\sum_{i=0}^{Ncells} E_i \cdot cos\theta_i \cdot cos\phi_i \tag{3.1}$$

$$\displaystyle{\not}E_{Ty} = -\sum_{i=0}^{Ncells} E_i \cdot cos\theta_i \cdot sin\phi_i \tag{3.2}$$

$$\displaystyle{\not}E_{T} = \sqrt{{\not}E_{Tx}^2 + {\not}E_{Ty}^2} \tag{3.3}$$

where E_i is a cell energy, above a certain threshold, of all calorimeter layers excluding the coarse hadronic section, θ_i and ϕ_i are cell angles as seen from the primary vertex. Transverse energy in the x and y direction is calculated (Equations 3.1 and 3.2). The muons, passing through the calorimeter, deposit very little energy in the calorimeter, therefore missing transverse energy must be corrected for the momentum of the muons present in the event. To do that, momentum of the muons are subtracted from the missing transverse energy.

3.4   b-Tagging

The associated Higgs production search requires accurate b-jet identification. In this analysis, events having a b-jet have to be selected from the large number of events containing light-quark and gluon jets. The b-tagging algorithm used in the analysis based on the fact that b-hadrons decay weakly after traveling an average distance of 1-3 mm (for the transverse energy range of 20-50 GeV). Among particles coming from the b decay, there are on average 5 charged particles which can be reconstructed as tracks in the SMT and CFT. Tracks from the b decay tend to
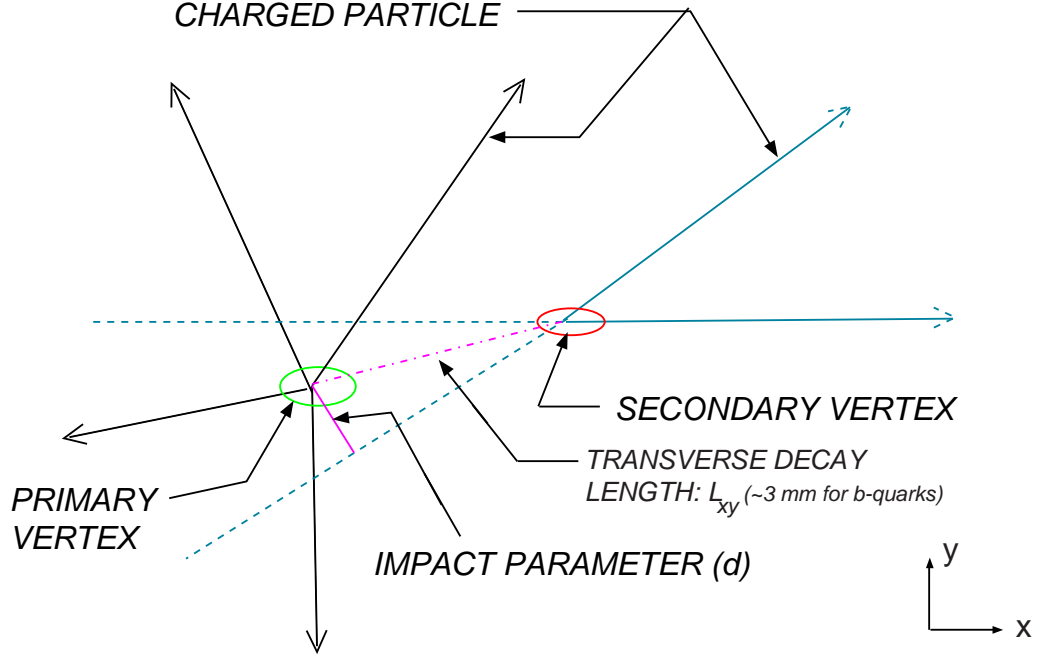
Figure 3.1. Displaced vertex. Adapted from [4]

have large Impact Parameter (IP) as well as high transverse momentum. Impact parameter is the distance between track and primary vertex (see Figure 3.1). Track Impact parameter is signed by using perigee coordinates of the track relative to the primary vertex and the jet momentum vector

3.4.1 Taggability

The b-tagging algorithm is based on the tracking information. Therefore for the algorithm to be able to tag a jet, the jet has to meet certain criteria: at least two associated tracks with $p_T > 0.5$ GeV within $\Delta R < 0.5$ cone of the jet axis, and ≥ 3 hits in the SMT and ≥ 7 hits in the CFT. A jet which meets these criteria is called taggable.

Taggability in the data and Monte Carlo differ. This difference is shown on Figure 3.2. To account for this difference, the taggability derived from the data is

applied to the Monte Carlo later in the analysis.

3.4.2 The Jet Lifetime Probability Tagger

The Jet LIfetime Probability (JLIP) tagger is used for b-tagging in this analysis [15]. This tagger combines impact parameters of the tracks associated with a jet into single a variable - the Jet Lifetime probability $(\mathcal{P}_{jet})$ which is the probability that all tracks associated with a jet come from the primary vertex. $\mathcal{P}_{jet}$ of light jets (jets originated from u,d,s-quarks and gluons) is distributed between 0 and 1, whereas $\mathcal{P}_{jet}$ of heavy jets (originated from c and b quarks) is peaked at very low value (see Figure 3.3). Therefore, b-jets can be selected by placing cut on JLIP. The $\mathcal{P}_{jet}$ calculation requires knowing the resolution of the impact parameter. The IP resolution function is derived from the data using tracks with negative IP.

3.4.3 JLIP performance in Data

The b-tagging efficiency is defined as ratio between the number of tagged b-jets and the number of taggable b-jets. Obtaining pure samples of b-jets or light-jets in the data for studying efficiencies is impossible, which makes measuring b-tagging efficiency in data quite difficult. The efficiency to tag light quark jets (also called the mistag rate) can be measured on emqcd or track in jet trigger data using tracks with negative Impact Parameter. Since the signed $\mathcal{P}_{jet}$ is distributed symmetrically around a zero value, the mistag rate can be estimated as:

$$\varepsilon_{light} = \varepsilon_{data}^- \cdot F_{hf} \cdot F_{ll}$$

where

- ε_{data}^- is the negative tag rate in jet trigger or emgcd data

- $F_{hf} = \varepsilon_{QCDlight}^- / \varepsilon_{QCDall}^-$ is the ratio between the number of negative tagged light jets over the total number of negative tagged jets in the QCD Monte Carlo.
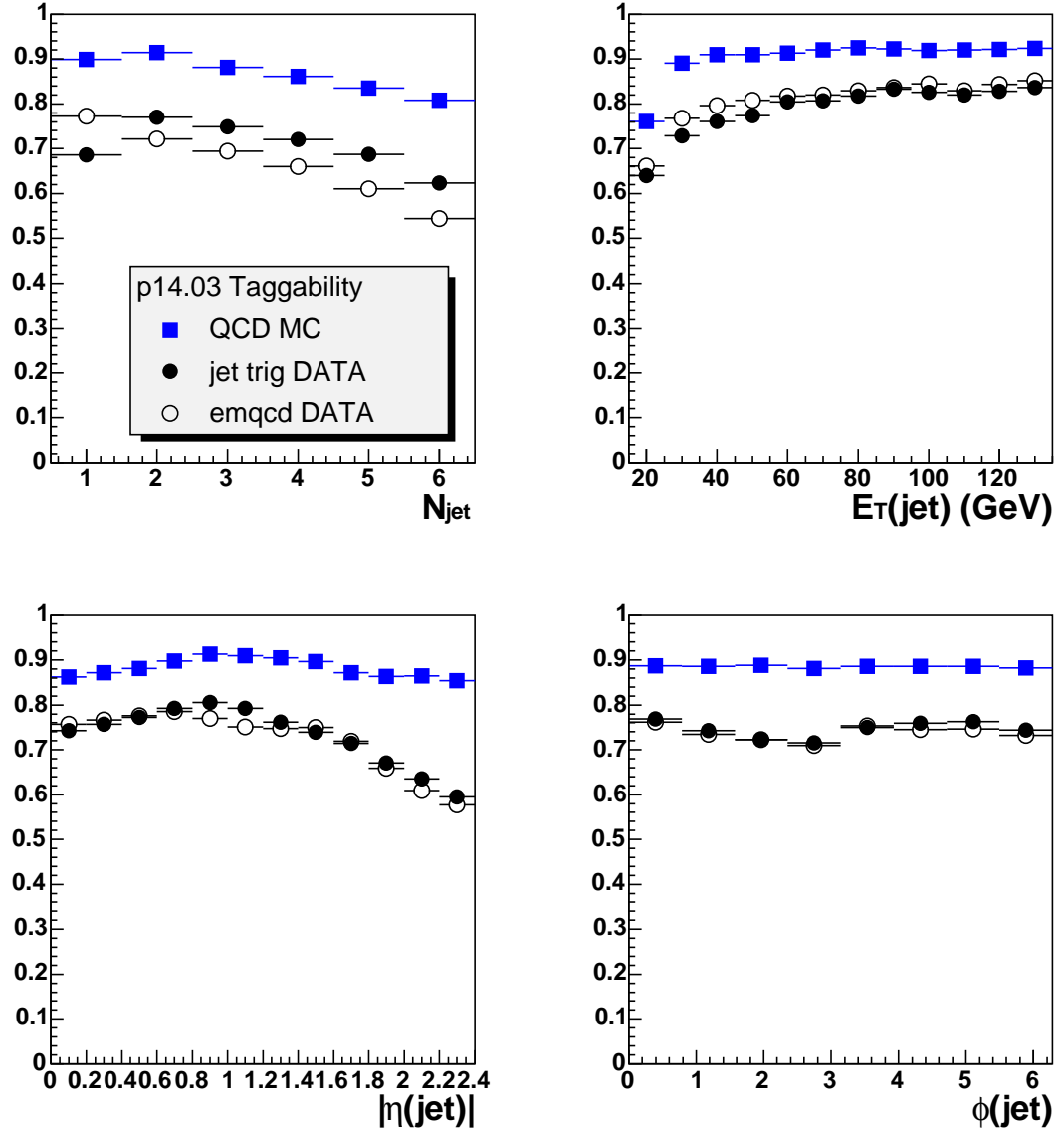
Figure 3.2. Taggability in the Data and Monte Carlo. Adapted from [15].
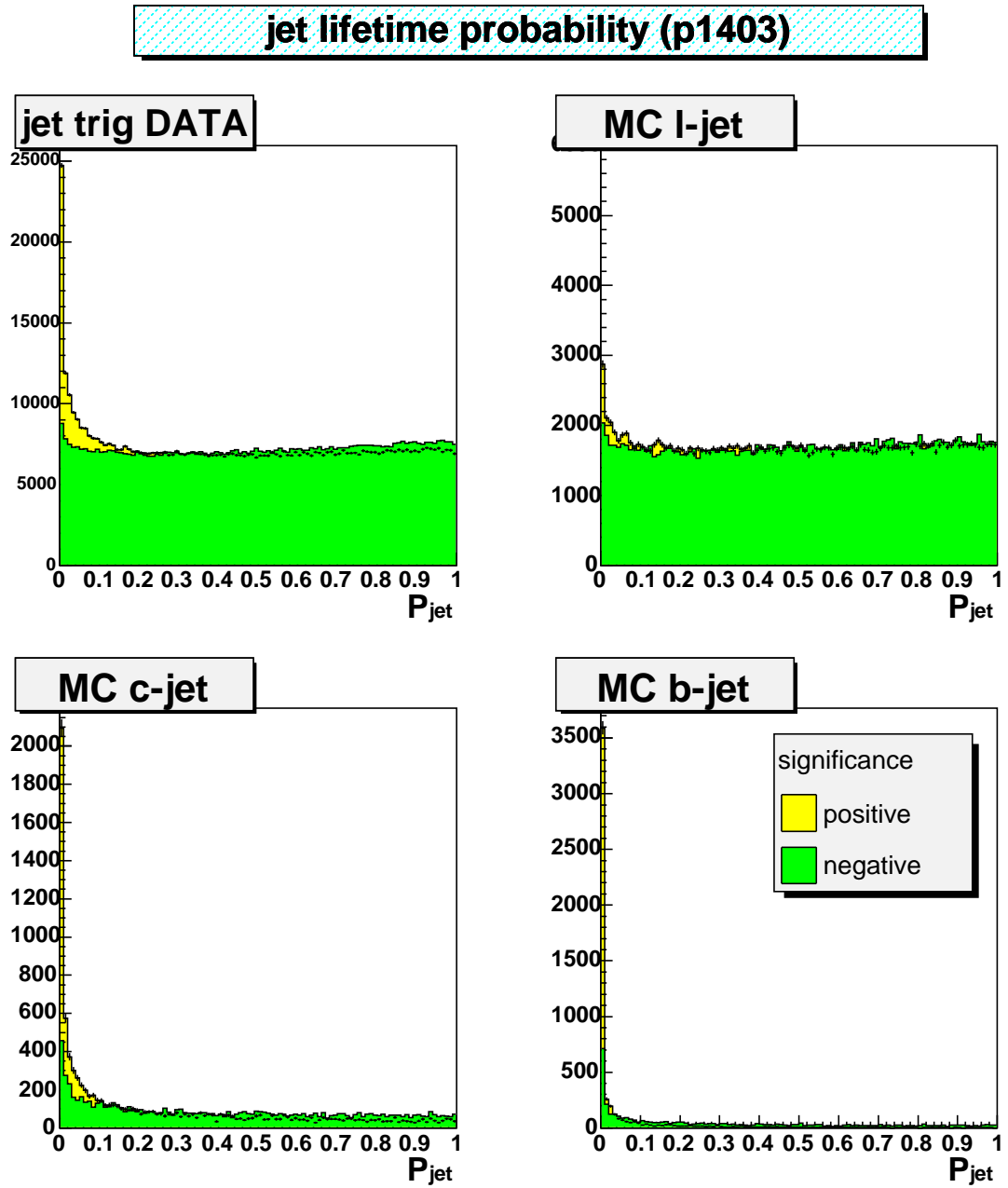
Figure 3.3. Jet Lifetime Probability in data and Monte Carlo. Adapted from [15].

- $F_{ll} = \varepsilon^{+}_{QCDlight}/\varepsilon^{-}_{QCDlight}$ is the ratio between the number of positive tagged jets from light quark over the number of negative tagged jets from light quarks in the QCD Monte Carlo.

Mistag rates derived from data are shown on Figure 3.4 and 3.5.

About 20% of b-jets have a muon. Three methods are used to measure the tagging efficiency on b-jets using muon-in-jet data sample. The first two methods rely on the fit of the muon p_{Trel} distribution in the muon-in-jet sample to p_{Trel} templates obtained from Monte Carlo simulation. The p_{Trel} is the transverse momentum of the muon relative to the combined jet and muon axis. Muons from the b-quark decay, due to the higher b-quark mass, tend to have higher p_{Trel} than muons from the light quark jets. The fit of p_{Trel} distribution using Monte Carlo templates allows measurements of the fractions of the b-jets in the sample before and after JLIP b-tagging. The first method uses single tag and no tag samples for evaluating tagging efficiency, the second one relies on the double tag and single tag samples.

The third method (*SystemD*) requires very little Monte Carlo and does not use the p_{Trel} templates. The SystemD method needs two data samples with different b-quark fractions: the muon-in-jet sample and the subsample where jet have a tagged jet in the opposite direction (opposite tag) are used. Also, two different taggers are required: The JLIP tagger and muon with $p_{Trel} > 0.7$ GeV requirement are used as taggers. In the SystemD a system of equations is composed which can be solved after making few assumptions. The solution provides b-fractions in both samples as well as tagging efficiency for b-quark and light jets. The b-tagging efficiency for the loose cut measured in the data is shown on Figure 3.6. The tagging efficiencies differ in the data and Monte Carlo, therefore tagging efficiencies or Tag Rate Functions (TRFs) derived from the data are applied to the jets in Monte Carlo simulations.
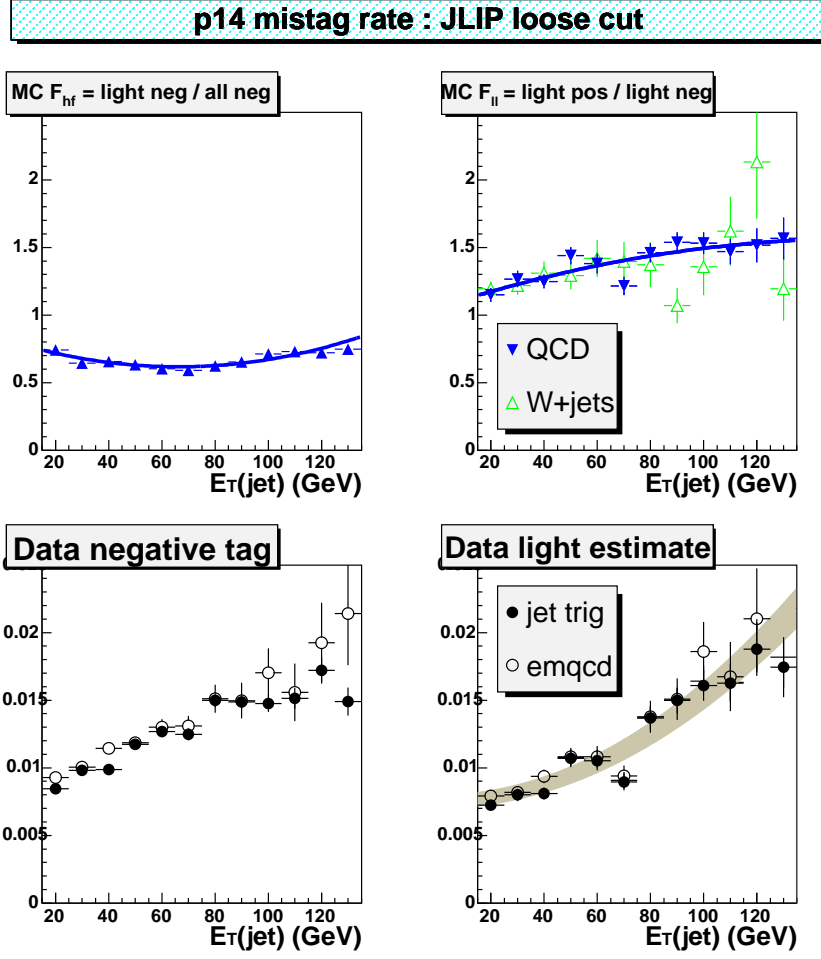
Figure 3.4. Jet E_T dependence of the mistag rate for the loose JLIP cut.
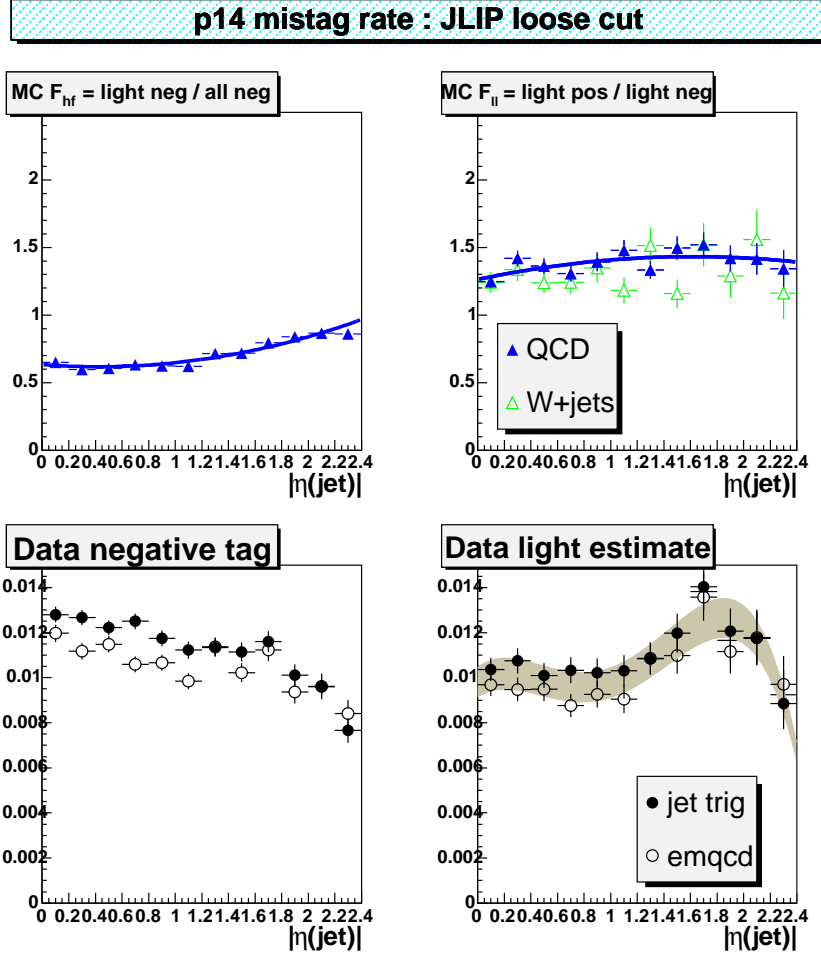
Figure 3.5. Jet η dependence of the mistag rate for the loose JLIP cut.
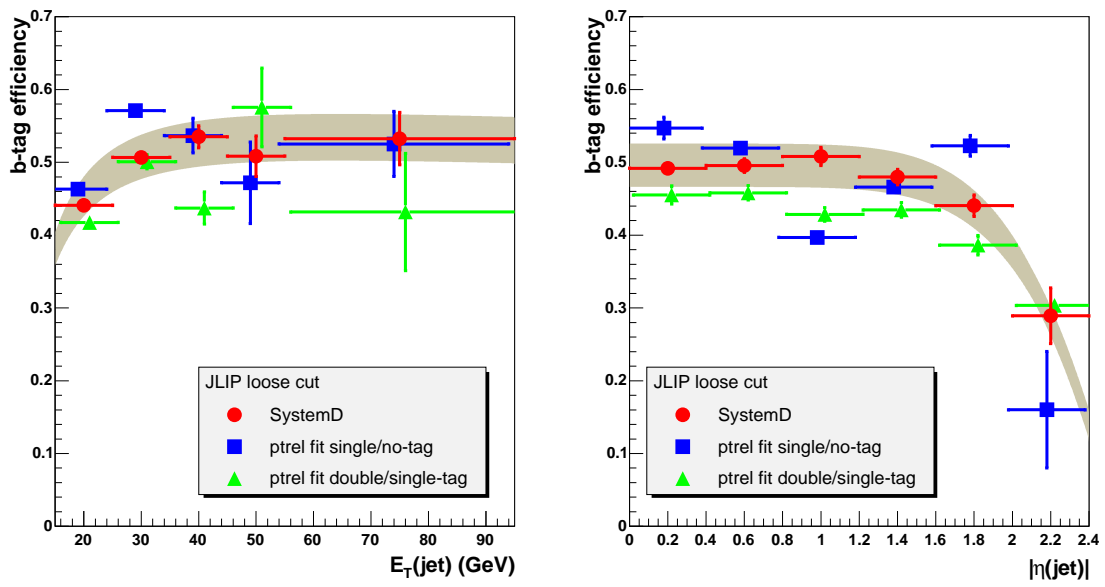
Figure 3.6. Loose b-tagging efficiencies in data using three different methods (SystemD, muon p_{Trel} single and double b-tag)

3.5   Tau Identification

Taus that originate from Z-boson decays have an energy of about 45 GeV. For such energy, the τ-leptons average travel distance before decaying is about 2.2 mm. Therefore, one can not directly detect it; instead, information from the calorimeter and tracking system is used for identification of the decay products of the τ-lepton. The following is the list of properties of a reconstructed τ-candidate:

- Calorimeter Cluster, found using simple cone algorithm with cone size $R = 0.3$ and isolation cone size $R_{iso} = 0.5$.

- EM Sub-clusters, which are individual neutral pions from τ decay, found by a nearest neighbor algorithm in the EM3 layer of the calorimeter. If such clusters are found, then EM cells in other layers and preshower hits are attached to them.

- Tracks, which are likely to have been produced by the τ decay products.

Based on the the τ decay mode, the reconstructed taus are divided into 3 types:

1. $\tau \rightarrow \pi^- \nu_\tau$ - one track with calorimeter cluster and no associated EM sub-cluster,

2. $\tau \rightarrow \rho^- \nu_\tau \rightarrow \pi^0 \pi^- \nu_\tau$ - calorimeter cluster, one track and at least one associated EM sub-cluster,

3. $\tau \rightarrow \pi^- \pi^+ \pi^- (\pi^0) \nu_\tau$ - calorimeter cluster, two or more tracks, any number of associated EM sub-clusters including zero.

Type 1 and 2 taus are referred to as "1-prong", whereas type 3 are referred to as "3-prong". One should note that taus decaying leptonically to electrons are most likely reconstructed as type 2. Discrimination of the taus from the background utilizes a Neural Net. Depending on the signal signature one is interested in, the electrons coming from τ's can be considered as a background as well as a signal. Tau reconstruction defines the following Neural Nets:

- NN_I , trained on the Monte Carlo sample without $\tau \rightarrow e$ decay,

- NN_{II}, trained on the Monte Carlo sample where $\tau \rightarrow e$ decay is allowed.

The following is a list of NN input variables and their descriptions:

Variables used for both NN's:

- $profile = (E_{T1} + E_{T2})/E_T^\tau$, where E_{T1} and E_{T2} are the transverse energies of the two most energetic calorimeter towers. Used for all τ-types.

- $caliso = (E_T^\tau - E_T^{core})/E_T^{core}$. A calorimeter isolation. Used for all τ-types.

- $trkiso = \sum p_T^{trk}/\sum p_t^{\tau trk}$, where $p_T^{\tau trk}$ (p_T^{trk}) is the p_T of a track within within $R < 0.5$ cone associated (not associated) with τ candidate. Used for all τ-types.

- $em12isof = (E^{EM_1} + E^{EM_2})/E^\tau$ in the $R < 0.5$ cone, where E^{EM_1} and E^{EM_2} are the energies of the first two EM layers of the calorimeter. Variable used for τ-type 1 to reject jets with one energetic charged track and soft neutral pion.

- $\delta a = \sqrt{(\Delta\phi/sin\theta)^2 + (\Delta\eta)^2}$, where differences are between $\sum\tau$-tracks and $\sum EM$-clusters. For small angles, the observed τ mass is equal to $e_{12} \cdot E_T^\tau \cdot \delta\alpha$. This variable is used for τ-types 1 and 2.

Variables used only for NN_I:

- $e_{12} = \sqrt{\sum p_T^{\tau trk} \cdot E_T^{EM}}/E_T^\tau$, where E_T^{EM} is the EM part of the transverse energy. Used for τ-types 2 and 3.

- $p_T^{\tau trk1}/E_T^\tau$, where $p_T^{\tau trk1}$ is the p_T of the highest-p_T track associated with the τ. Used for τ-type 1.

- $p_T^{\tau trk1}/(E_T^\tau \cdot caliso)$. A variable used for τ-type 2 that measures the amount of correlation between the track and the energy deposition in the isolation annulus.

Variables used only for NN_{II}:

- $rms_\tau = \sqrt{\sum_{i=1}^{n}[(\Delta\phi_i)^2 + (\Delta\eta_i)^2]E_{T_i}/E_T}$. A τ-cluster width. Used for all τ-types.

- fhf. Fine hadronic fraction of the E_T^τ. Used for τ-types 1 and 2.

- E_T^{em}/E_T^τ, where E_T^{em} is the transverse energy of the EM subclusters. Used for τ-types 2 and 3.

- $prf3$. Transverse energy of the leading EM subcluster divided by the transverse energy in layer 3 of the calorimeter in the $R < 0.5$ cone.

- $E_T^\tau/(E_T^\tau + \sum p_T^{\tau trk})$. Used for τ-types 2 and 3.

3.6 Tracking

3.6.1 SMT and CFT hit reconstruction

Track finding starts with reconstructing hits in the SMT and CFT systems.

In the SMT, signals from a group of adjacent strips above a certain threshold are used to construct a *silicon cluster*. The center of the cluster is defined as the strip weighted average:

$$\bar{n} = \frac{1}{c} \sum n_i \cdot c_i$$

where c_i is charge of the strip, n_i is position of the strip, and c is total charge in the cluster of strips. Due to the presence of magnetic field in the tracker volume electrons and holes do not drift in the direction of the electric field, but rather at a *Lorentz angle*. This angle depends on the strength of the magnetic field and carriers *Hall-mobility*. This Lorentz angle was measured and is about 4 degrees for for the holes and 18 degrees for the electrons. The centers of clusters in the SMT are corrected for the Lorentz angle. Opposing sides of the silicon detectors have stereo-pitch. Using this stereo information allows us to reconstruct a *silicon hit*, i.e., point in space through which a charged particle has passed. The hit position is reconstructed with 10 μm resolution in the axial direction and 35 μm in the z-direction.

In the CFT, similarly to the SMT, a group of adjacent fibers above certain threshold form a CFT cluster. Since the CFT doublet layers have only two sublayers, CFT clusters usually contain one or two fibers. Each of the eight CFT super-layers contains axial and stereo doublet-layers. Combining CFT clusters from axial and stereo layers allows reconstruction of z-coordinate of the CFT hit. The axial resolution of the CFT detector is about 100 μm and z-coordinate resolution is about 2 cm.

3.6.2 Track reconstruction

The DØ track reconstruction algorithm attempts to find tracks by creating a pool of all possible track hypotheses and filtering them according to well defined criteria until no track hypothesis is left in the pool [16].

The initial track hypothesis is constructed from three hits in the SMT. Hits are selected starting from the innermost layer and proceeding to outer layers. The first measurement can be any hit in SMT barrels or F-disks. The second measurement is any hit in the following layers provided that the axial angle between the first and second hits is smaller than $\Delta\phi = 0.08$. The third measurement can be in any layer which follows the second hit, provided that the radius of the circle drawn through the three selected hits is greater than 30 cm (30 cm corresponds to $p_T = 180$ MeV). The axial impact parameter (distance of the closest approach to the beam spot) of the track must be less than 2.5 cm and the χ^2 of the track fit is required to be smaller than 16. All track hypotheses which passed these requirements are extrapolated to the outer layers of SMT and CFT using a $\chi^2 < 16$ window. If there is more than one hit within this window, the track hypothesis is split into two or more. Construction of the track hypothesis continues until the end of tracker or when three consecutive missing hits *(misses)* are found.

The track filter requires the following conditions:

- At least four detectors (SMT or CFT) with both stereo and axial hits.
- There are no more than 3 inside misses.
- There are no more that 6 (forward and backward) misses
- There are no more than 2 inside SMT misses.
- $N_{hits}/5 > N_{miss}$
- Hypothesis with 1 or more inside misses must not have more than 4 (inside and forward) or 3 (inside and backward) misses.

60

The selected track hypotheses are then sorted according to the following (in the order of preference) criteria:

- the number of hits.
- lesser number of misses (inside+forward+backward).
- better χ^2.

The track hypothesis is declared as a *reconstructed track* if the number of shared hits with already selected reconstructed tracks satisfies the following conditions.

- $N_{shared} \leq (2/3)N_{tot}$
- $N_{shared} \leq N_{tot}/5$ or $N_{tot} - N_{shared} > 3$

3.7 Primary Vertex Reconstruction

Reconstructed tracks are used to find primary vertexes. These are the points where $p\bar{p}$ collisions have taken place. The primary vertex position along the z-axis is important for the reconstruction of the transverse energies of particles. A primary vertex is also required for b-tagging. The DØ primary vertex reconstruction utilizes a two-pass method described in [17].

In the first pass, a fitter runs over all tracks and clusters them in the z-direction. The parameters of the associated tracks are then used to determine the position of the primary vertex. Vertex fitting is done by Modified Kalman Fitter algorithm. In the first pass, a very loose cut of $dca/\sigma_{dca} < 100$ with respect to the center of the detector is applied to the tracks, where dca is a distance of closest approach in the xy plane. In the second pass, a tight cut of $dca/\sigma_{dca} < 3$ is used, where the dca is measured with respect to the beam spot position calculated from the first pass-list of vertexes.

For the typical instantaneous luminosity, about 0.5 inelastic $p\bar{p}$ collisions are expected in addition to the hard-scattering event which fired the trigger. If event has

more than one primary vertex, the hard-scattering primary vertex has to be selected among the list of reconstructed primary vertexes. On average, the tracks from a minimum-bias $p\bar{p}$ collision have smaller p_T than tracks from the hard-scattering interaction. Each track attached to the primary vertex and having $p_T > 0.5$ GeV is assigned a probability to have come from the minimum bias event:

$$P(p_T) = \frac{\int_{log_{10}(p_T)}^{\infty} F(p_T)dp_T}{\int_{log_{10}(0.5)}^{\infty} F(p_T)dp_T}$$

where $F(p_T)$ is the minimum-bias $log_{10}(p_T)$ distribution obtained from Monte Carlo simulation [18]. Then, the probability that the primary vertex came from the minimum-bias event is calculated by taking the product of the individual track probabilities weighted by the number of tracks associated with the primary vertex. In the end, the vertex with the lowest minimum-bias probability is selected as the primary vertex of the event.

CHAPTER 4

ANALYSIS

In this chapter, details on the neutral Higgs search in the channel with associated b-hadron, muon and tau-lepton in the final state using data collected in Run II are presented. Before getting into details, it is often useful to get basic a idea of the analysis.

The signature of a Higgs boson in this analysis is very similar to the signature of the Z boson with associated jet, that is: relatively high-p_T back-to-back muon-tau pair, low-p_T associated jet, and possibly missing transverse energy. The main difference in the kinematics is the invariant mass of the muF-tau pairs. However, since the tau decay produces missing energy, the invariant mass distribution is very wide and therefore, there is significant overlap between the Z-boson and Higgs-boson distributions. Thus, looking at invariant mass alone is difficult, especially for Higgs masses close to the Z-boson mass and require very precise normalization of the Monte Carlo.

Another way to search for a Higgs boson is to look at the b-tagging rate for the associated jet. For the Z-bosons decaying into mu-tau pairs, the b-tagging rate is small, whereas for the Higgs in the MSSM it is large. Moreover, the b-tagging rate for jets in $Z + jets \rightarrow \tau^+\tau^- + jets$ process must be the same as in the process where the Z-boson decays directly into muons, $Z + jets \rightarrow \mu^-\mu^+ + jets$. We also know that the $h \rightarrow \mu^-\mu^+$ branching ratio is negligible compared to $h \rightarrow \tau^-\tau^+$. Therefore,

the Higgs does not contribute meaningfully into the b-tagging rate measured in the $\mu^+\mu^-$ channel. Thus, the idea is to compare the b-tagging rates in these two ($\mu^+\mu^-$ and $\tau^+\tau^-$) channels. Presence of the Higgs boson will manifest itself in the higher b-tagging rate in the $\tau^+\tau^-$ channel. It must be noted that in this analysis we do not compare the b-tagging rates directly; instead, we use the b-tagging rate measured in the $\mu^+\mu^-$ channel to estimate the background from the Z production.

4.1   Data Sample and quality

This analysis was performed on 400 pb^{-1} of Run II data, corresponding to physics runs 162006 through 194556. These runs were recorded between August 2002 and July 2004. The data were processed with p14.03.00, p14.03.01, p14.03.02, p14.05.00, p14.05.02 and p14.06.00 versions of the DØ reconstruction software (D0 RECO). Using different versions of reconstruction software creates problems with consistency of data as well as the possibility of duplicating events. These problems were solved by the DØ Common Sample Group, which ran the data through the pass2 fixer program and created different skim samples. The fixer program fixes data reconstructed with older versions to be compatible with the latest version of reconstruction. In this analysis the single muon (1MUloose) skim was used. This skim requires at least one *loose* quality muon with $p_T > 8$ GeV, the latter measured either from the local muon system, or from a global fit of a central track and the local muon system. This skim is quite large (about 80 million events). To reduce the data sample to a manageable size, events from the 1MUloose skim were required to have a tau-candidate, and $p_T > 12$ GeV for the muon. Also, events were required to fire one of the two selected single muon triggers (see Section 4.3 for the triggers used in the analysis). After this selection, the sample was reduced to the 278 thousand events.

The Offline Run Quality Database contains data quality information for different

sub-detectors. Runs declared as having bad quality for Muon, Calorimeter, CFT or SMT were removed from the data sample. Figure 4.1 shows the run number distribution for the sample. The total reconstructed luminosity for the selected triggers (described in Section 4.3) was 328 pb^{-1}.
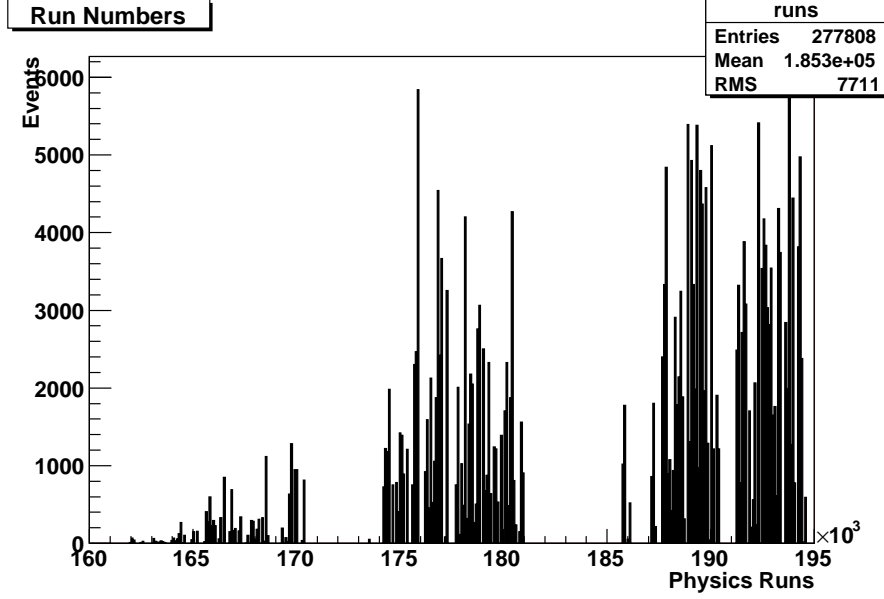
Figure 4.1. Run numbers used in in the analysis.

4.2   Monte Carlo Samples

For the signal, the Standard Model process $p\bar{p} \rightarrow bH \rightarrow b\tau^{+}\tau^{-}$ were used. To reduce the amount of MC generation, one of the τ's was forced to decay leptonically into a muon, whereas the second τ was free to decay to all allowed modes. The signal events were generated using the PYTHIA [19] generator in version p17.09.01 of the DØ software and with $p_T > 15$ GeV and $|\eta| < 2.5$ cuts on the partons. The τ-leptons were decayed using the Tauola package. The events were then reconstructed using version p14.07.00 of the reconstruction software.

The $t\bar{t}$, $W + jj$, $W + c\bar{c}$, $W + b\bar{b}$ and WW backgrounds were simulated using

65

ALPGEN [20] with PYTHIA. PYTHIA minimum bias events were added to all generated events, according to a Poisson distribution with a mean of 0.4 events. The simulated events were processed through the DØ detector and electronics simulation before being reconstructed with the same software as the collider data.

4.3 Trigger

4.3.1 Trigger Definitions

Two single muon triggers from trigger lists v10.30 through v12 were used in this analysis: MU_W_L2M5_TRK10 and MUW_W_L2M3_TRK10 with 29 and 299 pb^{-1} recorded luminosities, respectively.

Trigger MU_W_L2M5_TRK10 requires:

- L1: at least one muon trigger in the "wide" CFT region (i.e., for detector $|\eta| < 1.5$) with *tight* scintillator only.

- L2: at least one muon with $p_T > 5$ GeV satisfying *medium* quality requirements (no region requirement).

- L3: at least one Level 3 central track with $p_T > 10$ GeV.

Trigger MUW_W_L2M3_TRK10 requires:

- L1: at least one muon trigger in the "wide" CFT region with *tight* scintillator and *loose* PDT wire requirements. Calorimeter readout must not be unsuppressed.

- L2: at least one *medium* muon with $p_T > 3$ GeV.

- L3: at least one Level 3 central track with $p_T > 10$ GeV.

4.3.2 Trigger Efficiencies

The muon trigger efficiencies were determined from $Z \rightarrow \mu^+\mu^-$ data using the tag-and-probe method [21]. One of the muons is required to have medium quality and to match to the trigger information. The other muon is required to have a track which is used to 'probe' different parts of the muon system. The matching of the

'tag' muon to the trigger prevents a possible trigger bias, since the recorded events are required to have fired some trigger.

- A 'tag' muon is a *medium* quality muon matched to the a central track with $p_T > 30$ GeV.

- The 'tag' muon must not be cosmic.

- A 'probe' track is identified as a track with at least 8 CFT hits, $p_T > 20$ GeV, $\chi^2/d.o.f. < 4$, and $|dca| < 0.02$ (0.2) cm for a track with (without) SMT hits.

- Both muons have to be isolated in calorimeter and tracker.

- $\Delta R > 2$ between tracks.

- The acollinearity, defined as $A = \pi - |\phi_1 - \phi_2| + |\theta_1 + \theta_2 - \pi|$ must be greater than 0.05.

- The event is required to fire one of the following single muon triggers: MU_W_L2M0_TRK3, MU_W_L2M0_2TRK3, MU_W_L2M3_TRK10, MU_W_L2M5_TRK10, MUW_W_L2M3_TRK10, MUW_W_L2M5_TRK10, or MUW_A_L2M3_TRK10.

- The 'tag' muon has to be associated with L1 and L2 triggers.

- The L3 tracking efficiency is measured with respect to all reconstructed tracks that are isolated from the 'tag' muon.

The L1 and L2 trigger efficiencies as a function of the A-layer detector-η and detector-ϕ are shown in Figures 4.2 and 4.3, respectively. Low efficiency region corresponds to the bottom part of the muon system which is not fully instrumented. At Level 3, the L3 tracking efficiency parametrized as a function of track p_T, track η, and vertex-Z (Z_{vtx}) position. The L3 triggers, used in the analysis, do not require matching between track and muon object, which means that the L3 trigger can be fired by any track. The Efficiency parametrization has to reflect this fact. Ten Z_{vtx} bins were used to parametrize the L3 tracking efficiency as a function of track p_T and η in each bin. Tracks which are associated with a 'tag' muon were excluded, in order to prevent any bias from the trigger. Figures 4.4 and 4.5 show these parametrizations in four Z_{vtx} bins (for brevity). The product of all three trigger efficiencies is assigned as a weight to the Monte Carlo events. In order to account

67

for efficiency differences between the two muon triggers, the two trigger efficiency parametrizations are weighted according to the recorded luminosity of each trigger, and their weighted average is used as the trigger weight in the Monte Carlo. For the signal and $t\bar{t}$ Monte Carlo samples, this trigger parametrization gives an average trigger efficiency of 62±1.1% and 63±1.1%, respectively.
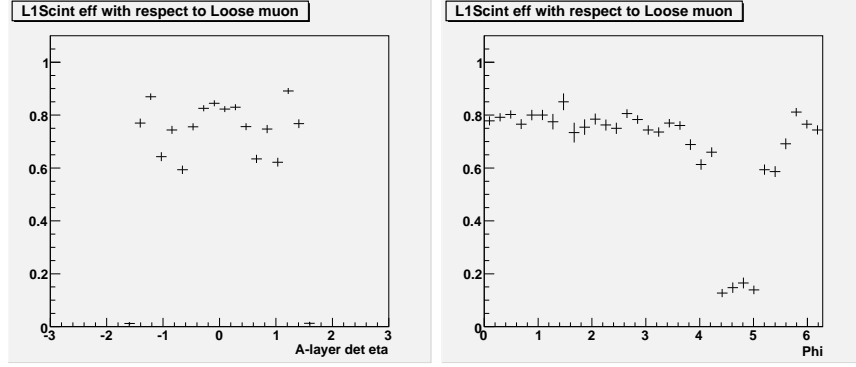
(a) L1 scintillator efficiency as a function of the A-layer detector η.

(b) L1 scintillator efficiency as a function of detector ϕ.
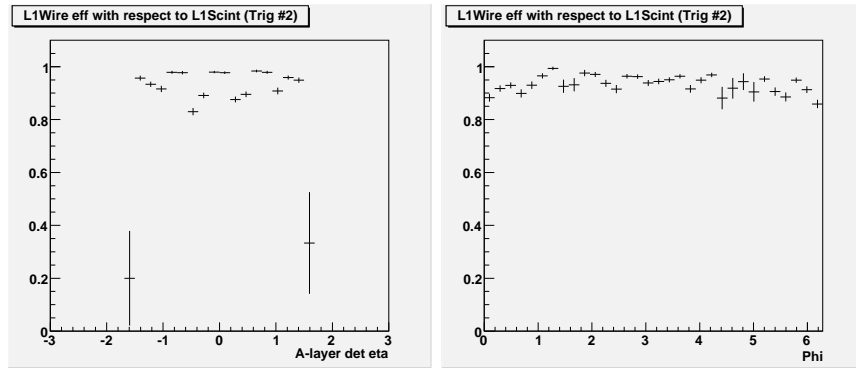
(c) L1 wire efficiency (with L1 scintillator) as a function of the A-layer detector η.

(d) L1 wire efficiency (with L1 scintillator) as a function of detector ϕ.
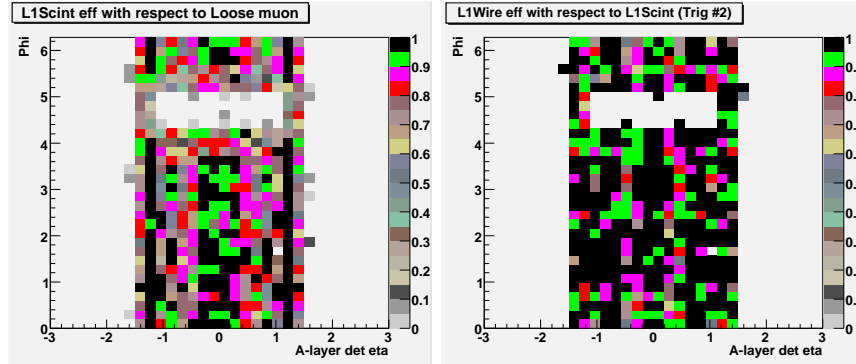
(e) L1 scintillator efficiency as a function of the A-layer detector η and detector ϕ.

(f) L1 wire efficiency (with L1 scintillator) as a function of the A-layer detector η and detector ϕ.

Figure 4.2. L1 scintillator and wire trigger efficiencies with respect to a *loose* reconstructed muon.
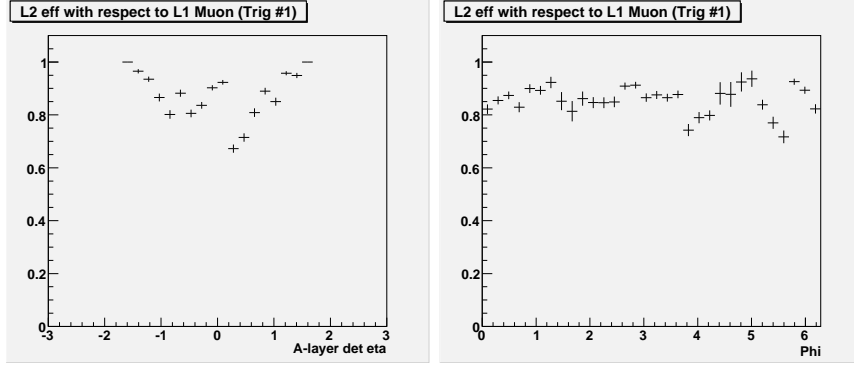
(a) L2 (L2M5) efficiency as a function of the A-layer detector η.

(b) L2 (L2M5) efficiency as a function of detector ϕ.
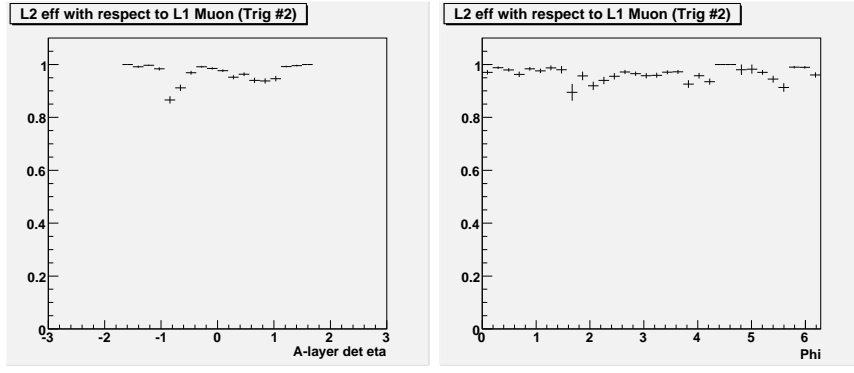
(c) L2 (L2M3) efficiency as a function of the A-layer detector η.

(d) L2 (L2M3) efficiency as a function of detector ϕ.
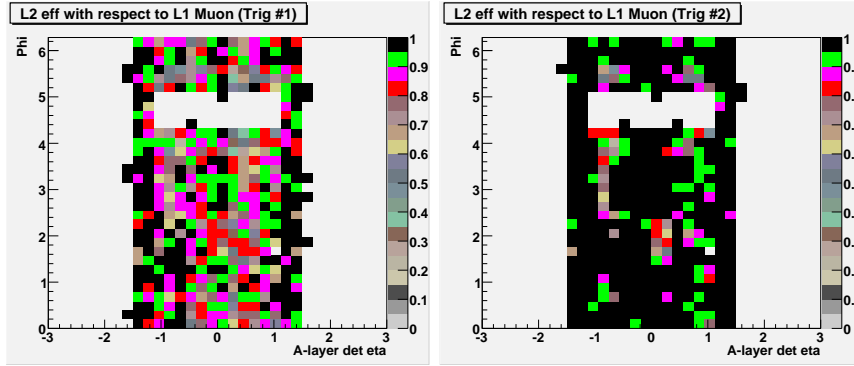
(e) L2 (L2M5) efficiency as a function of the A-layer detector η and detector ϕ.

(f) L2 (L2M3) efficiency as a function of the A-layer detector η and detector ϕ.

Figure 4.3. L2 trigger efficiencies for the L2M5 and L2M3 triggers with respect to a *loose* reconstructed muon which passes L1.

(a) L3, $-40 < Z_{vtx} < -16$ cm.

(b) L3, $-16 < Z_{vtx} < 0$ cm.

(c) L3, $0 < Z_{vtx} < 16$ cm.

(d) L3, $16 < Z_{vtx} < 40$ cm.
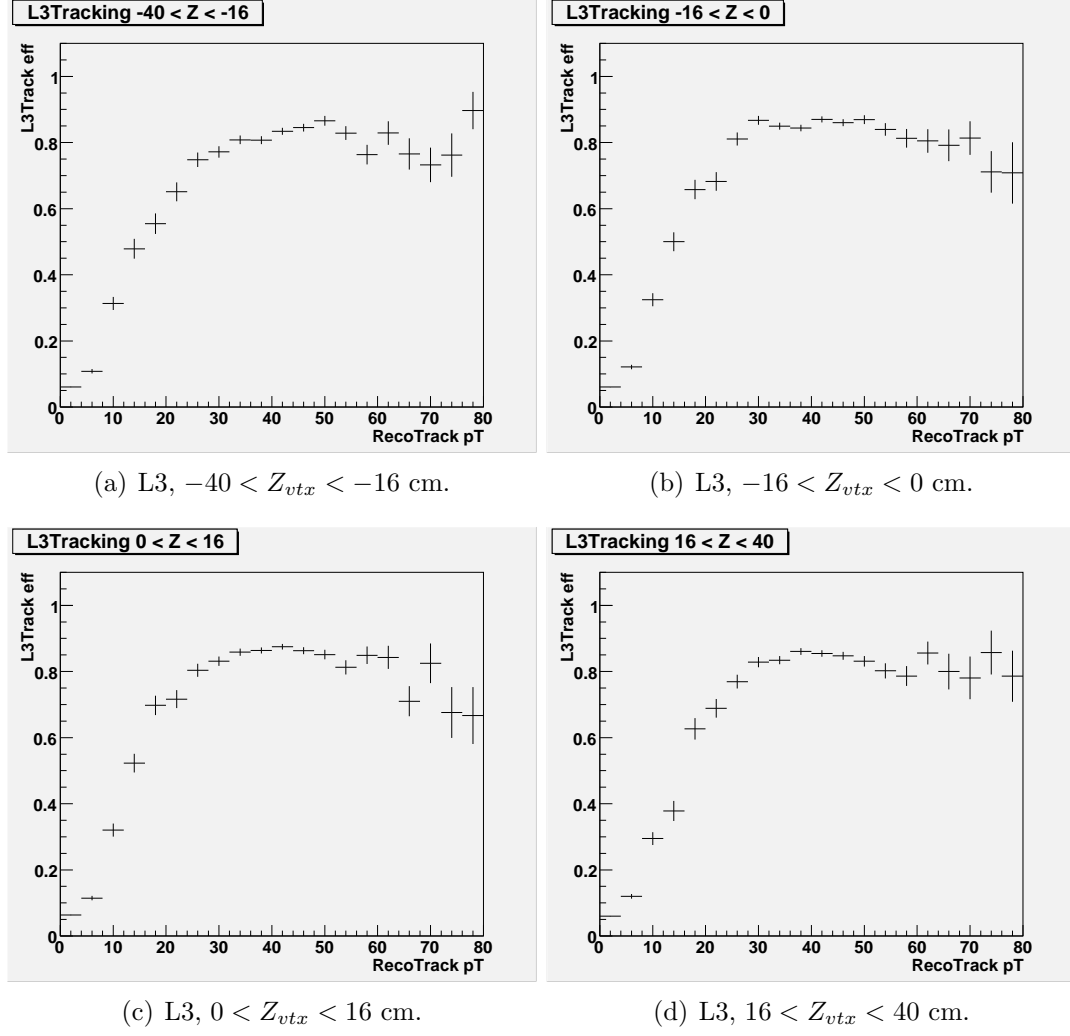
Figure 4.4. L3 trigger efficiency as a function of track p_T in separate Z_{vtx} bins, for track $|\eta| < 1.5$ (note that L3 trigger require track with $p_T > 10$ GeV)

71

(a) L3, $-40 < Z_{vtx} < -16$ cm.

(b) L3, $-16 < Z_{vtx} < 0$ cm.

(c) L3, $0 < Z_{vtx} < 16$ cm.

(d) L3, $16 < Z_{vtx} < 40$ cm.
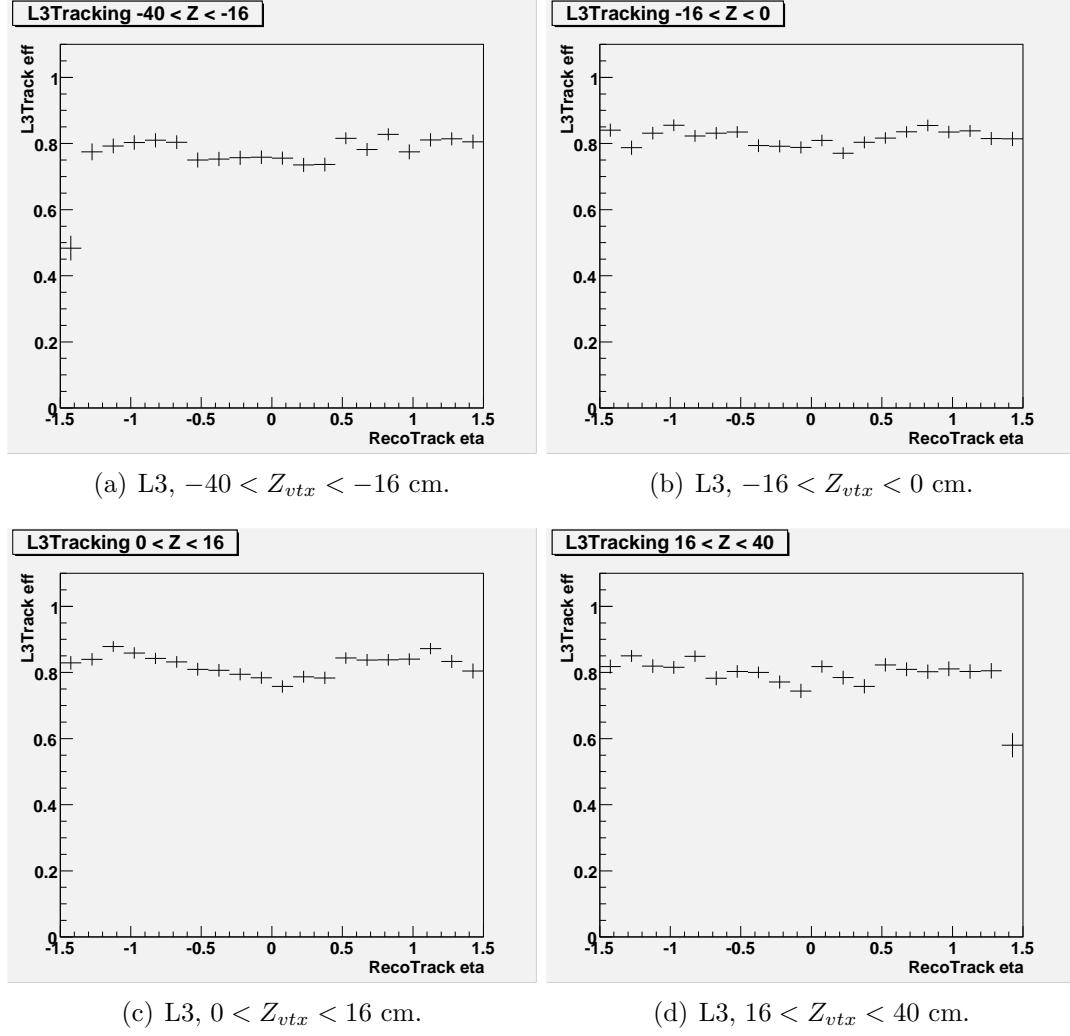
Figure 4.5. L3 trigger efficiency as a function of track η in separate Z_{vtx} bins, for track $p_T > 10$ GeV.

4.4 Object Selection

There are three types of physics objects used in this analysis: muons, hadronic taus, and b-jets. All selected objects are required to be associated with the same primary vertex within $\Delta Z_{vtx} < 1$ cm. The selection for each object type is described in the following.

4.4.1 Muons

The muon selection consists of the following requirements [22]:

1. *loose* quality muon with $p_T > 12$ GeV matched to a central track

2. E in cone of R=0.1 < 4 GeV

3. E(R=0.4)-E(R=0.1)<4 GeV

4. track isolation: $\sum_{\Delta R < 0.5} p_T(trks) < 2.5$ GeV

5. if there are two or more isolated muons in the event, the muon with the highest p_T is selected.

4.4.2 Hadronic Taus

As was discussed earlier there are three τ-types [23]:

1. $\tau^{\pm} \to \pi^{\pm} \nu_{\tau}$: one track with calorimeter cluster and no associated EM sub-cluster;

2. $\tau^{\pm} \to \rho^{\pm} \nu_{\tau} \to \pi^{\pm} \pi^0 \nu_{\tau}$: one track with calorimeter cluster and at least one associated EM sub-cluster (there can be more than one π^0 in the final state);

3. $\tau^{\pm} \to h^{\pm} h^+ h^- (\pi^0) \nu_{\tau}$: more than one track, with calorimeter cluster, and with or without associated EM sub-clusters (h refers generically to a hadron).

An object reconstructed as τ according to the above definitions, is considered as a τ-candidate if it satisfies the following requirements:

1. $E_T^{\tau} > 10$ GeV for type 1 and type 3 τ-candidates and $E_T^{\tau} > 5$ GeV for type 2 τ-candidates, where E_T^{τ} is the E_T of the calorimeter cluster associated with the τ-candidate (τ-cluster)

2. $\sum p_T^{\tau_{trk}} > 7$ GeV for type 1 and type 3 τ-candidates and $\sum p_T^{\tau_{trk}} > 5$ GeV for type 2 τ-candidates, where $\sum p_T^{\tau_{trk}}$ is the sum of the p_T's of all the tracks associated with the τ-candidate

3. τ-rms<0.25, with τ-rms defined as $\sqrt{\eta_{rms}^2 + \phi_{rms}^2}$, where $\eta_{rms} = \sum E_T^{tower} \cdot (\eta^{\tau} - \eta^{tower})/E_T^{\tau}$, and similarly for ϕ_{rms}

4. for type 1 and type 2 τ-candidates: $R^{\tau}_{trk} > 0.7$, with $R^{\tau}_{trk} = (E^{\tau} - E^{trk}_{CH})/p^{trk}_{T}$, where E^{trk}_{CH} is the energy deposited in a window of 5×5 towers around the τ-track in the coarse hadronic (CH) section of the calorimeter. This cut reduces the instrumental background from μ's misidentified as τ's.

5. $\Delta R(\mu, \tau) > 0.5$ (i.e., τ is not matched to μ)

6. $|\phi_{\mu} - \phi_{\tau}| > 2.0$ radians

After the above selection, the τ-candidates are passed through a τ-identification Neural Network (NN$_{\tau}$). The NN$_{\tau}$ has been trained separately for each τ type. The output of the NN$_{\tau}$ for reconstructed τ-candidates matched to a generated τ in the signal MC sample is shown in Figure 4.6.

Signal significance differs between different τ-types. Therefore, simply adding events of different types into one channel is not an efficient way to discriminate signal from background. Instead different τ-types have to be treated as separate sub-channels. The cuts on NN$_{\tau}$ are optimized separately for each τ type in the data (see Section 4.9.3). Optimal cuts were found to be:

- for type 1 τ's: NN$_{\tau}$>0.8

- for type 2 τ's: NN$_{\tau}$>0.8

- for type 3 τ's: NN$_{\tau}$>0.98

Type 3 channel suffer from a large QCD background and as a result the optimal NN$_{\tau}$ cut is tighter than for type 1 and 2. In the following sections, we will refer to the minimum NN$_{\tau}$ requirement for each τ type by $minNN_{\tau}$.

4.4.3 Jets

An event is required to have one or more jets satisfying the following standard quality criteria:

1. Jet is isolated from μ and τ_h ($\Delta R > 0.5$)

2. jet $E_T > 15$ GeV
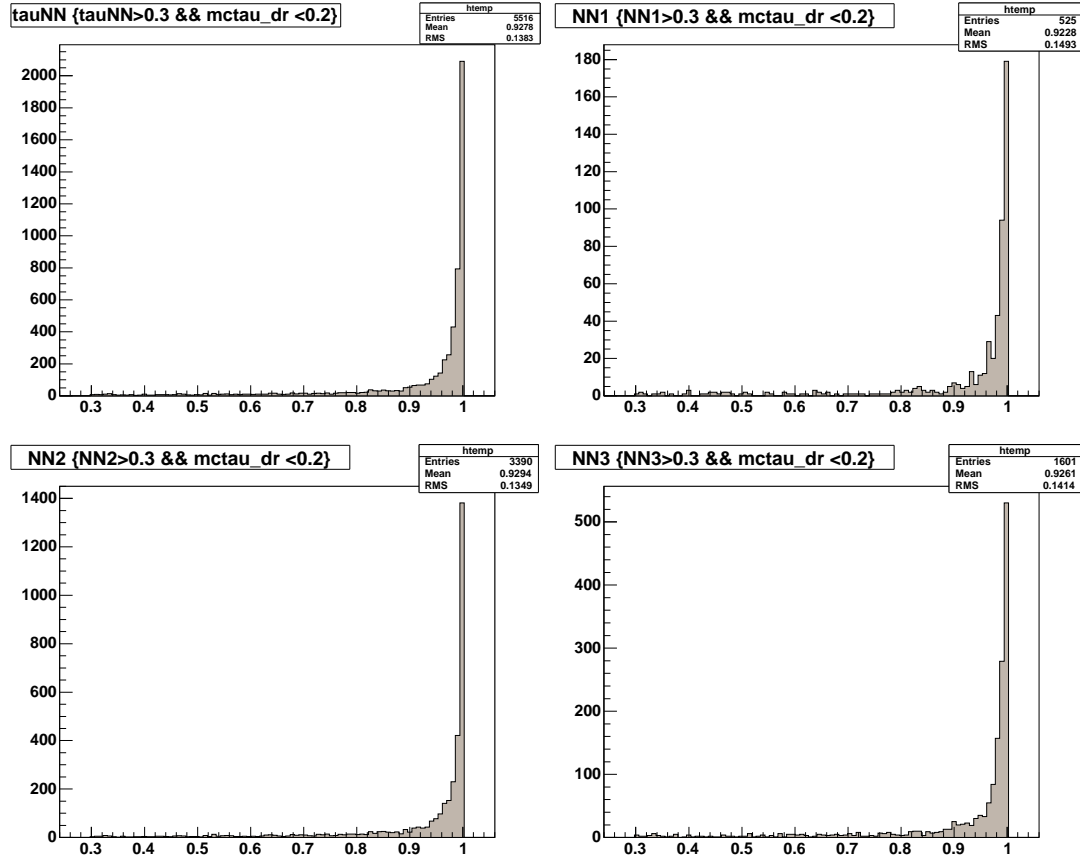
Figure 4.6. Output of the NN$_\tau$ for τ candidates matched to generated τ's in signal MC. The NN$_\tau$ outputs are shown separately for each τ type, as well as for the inclusive sample (in the upper left plot). The τ-candidate pre-selection included a NN$_\tau$>0.3 requirement, as is evident from the plots.

3. jet detector-$|\eta| < 2.5$

4. EM fraction between 0.05 and 0.95

5. (CHF<0.4 and F90<0.5) or (CHF<0.15)

6. (Hot cell fraction < 10) and (n90 > 1)

7. L1 confirmation: $(L1\ Scalar\ E_T)/(E_T^{reco} \cdot (1 - CHF)) > 0.4$

4.4.4 b Tagging

For b-jet identification, the Jet Lifetime Probability tagger (JLIP) [24] with *loose* tag is used in this analysis. The Monte Carlo events are weighted by the jet taggability and b-tagging efficiencies. The jet taggability parametrization is derived from $Z + jets \rightarrow \mu^+\mu^- + jets$ data. To do that, a sample of clean di-muon events from Z decay was created. The jet taggability E_T and η dependencies are shown in Figure 4.7. For the b-tagging efficiencies, Tag Rate Functions (TRF's) from the "btag_cert" package were used.

An event is required to have one or more jets satisfying the following criteria:

1. Jet has to be taggable.
2. Jet is tagged as a b-jet if it satisfies the JLIP *loose* requirements.

4.5   Signal Kinematic Distributions

In the following (Figures 4.8-4.14), the kinematic distributions (p_T or E_T, η, ϕ) for the muon, hadronic τ, and leading jet are shown for the signal Monte Carlo sample, after all selection criteria described in the previous section are applied, with the exception of the $|\phi_\mu - \phi_\tau| > 2.0$ cut and the b-tagging requirement. Also shown are the distributions of $\Delta\phi$ between the muon and the hadronic τ (Figure 4.15), and the invariant mass constructed from the 4-vector momenta of the μ, the τ_h and the missing E_T of the event (Figure 4.16). All plots are made using the data trigger efficiency as a weight applied to the Monte Carlo events (see Sec. 4.3.2).
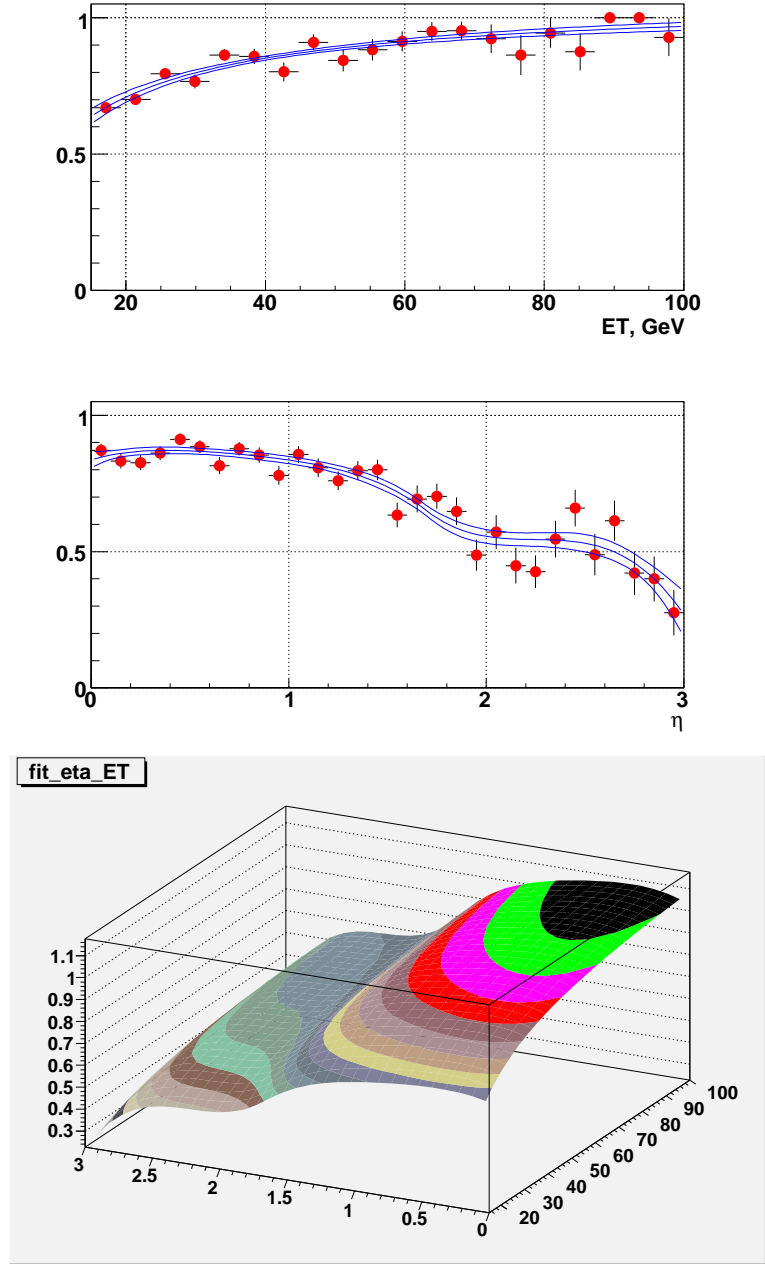
Figure 4.7. Jet taggability as a function of jet E_T and η and 2-dimensional parametrization; derived from $Z + jets \rightarrow \mu\mu + jets$ data.
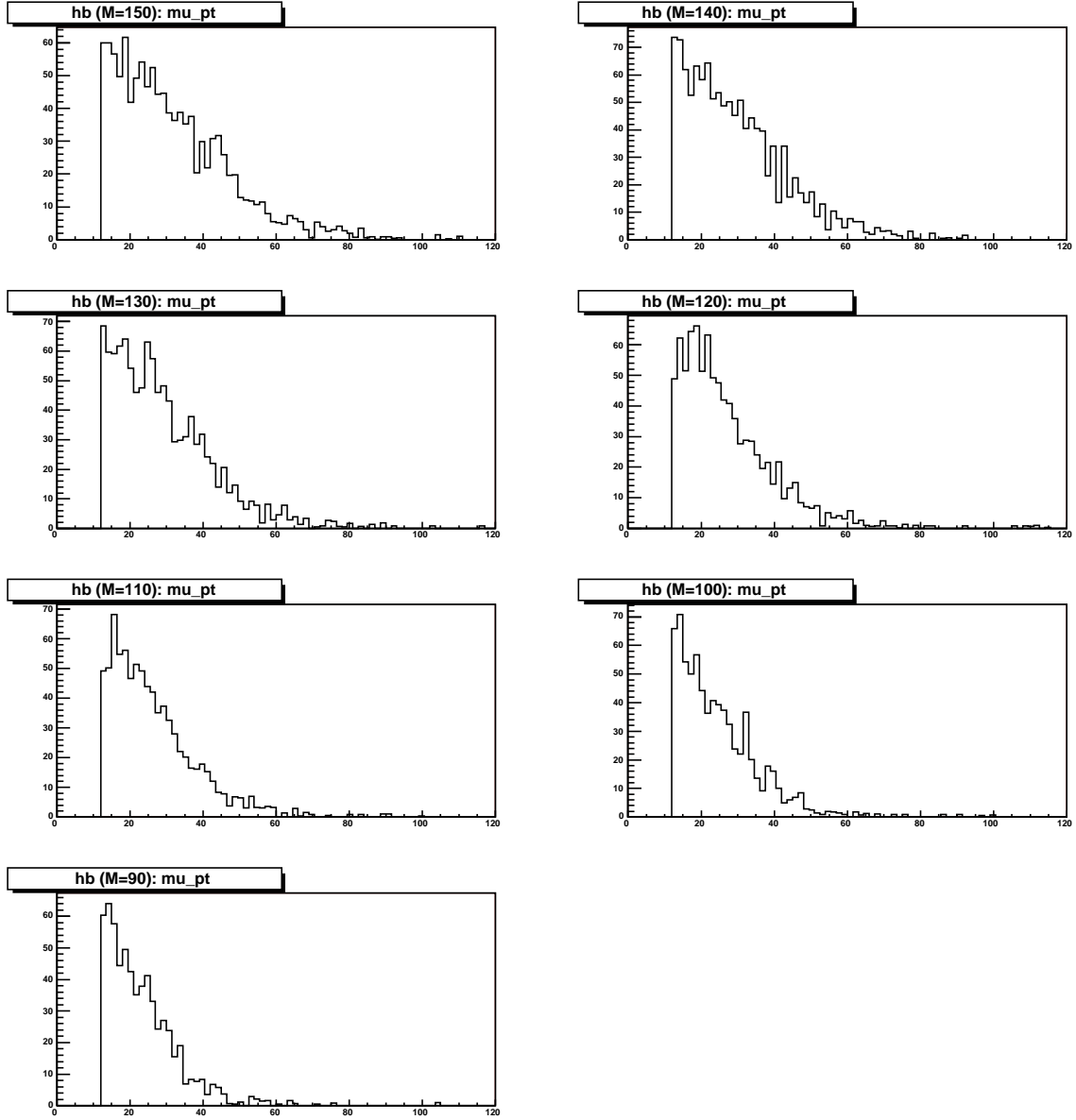
Figure 4.8. Signal Muon p_T distribution for the different Higgs masses (Pythia Monte Carlo). Drop in the distribution around $\phi = 4.5 \, rad$ is because bottom part of the muon system is not fully instrumented.
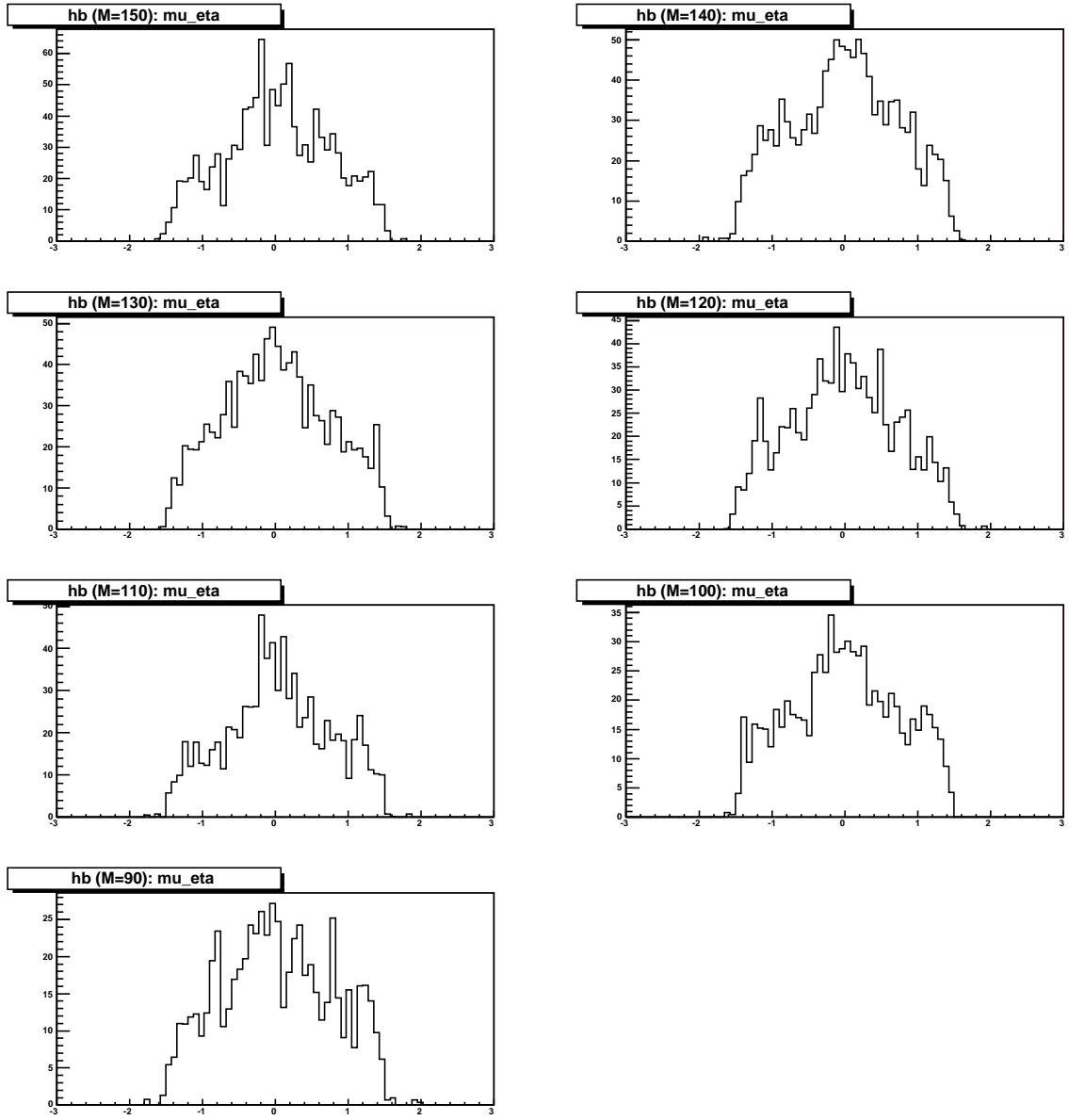
Figure 4.9. Signal Muon η distribution for the different Higgs masses (Pythia Monte Carlo).
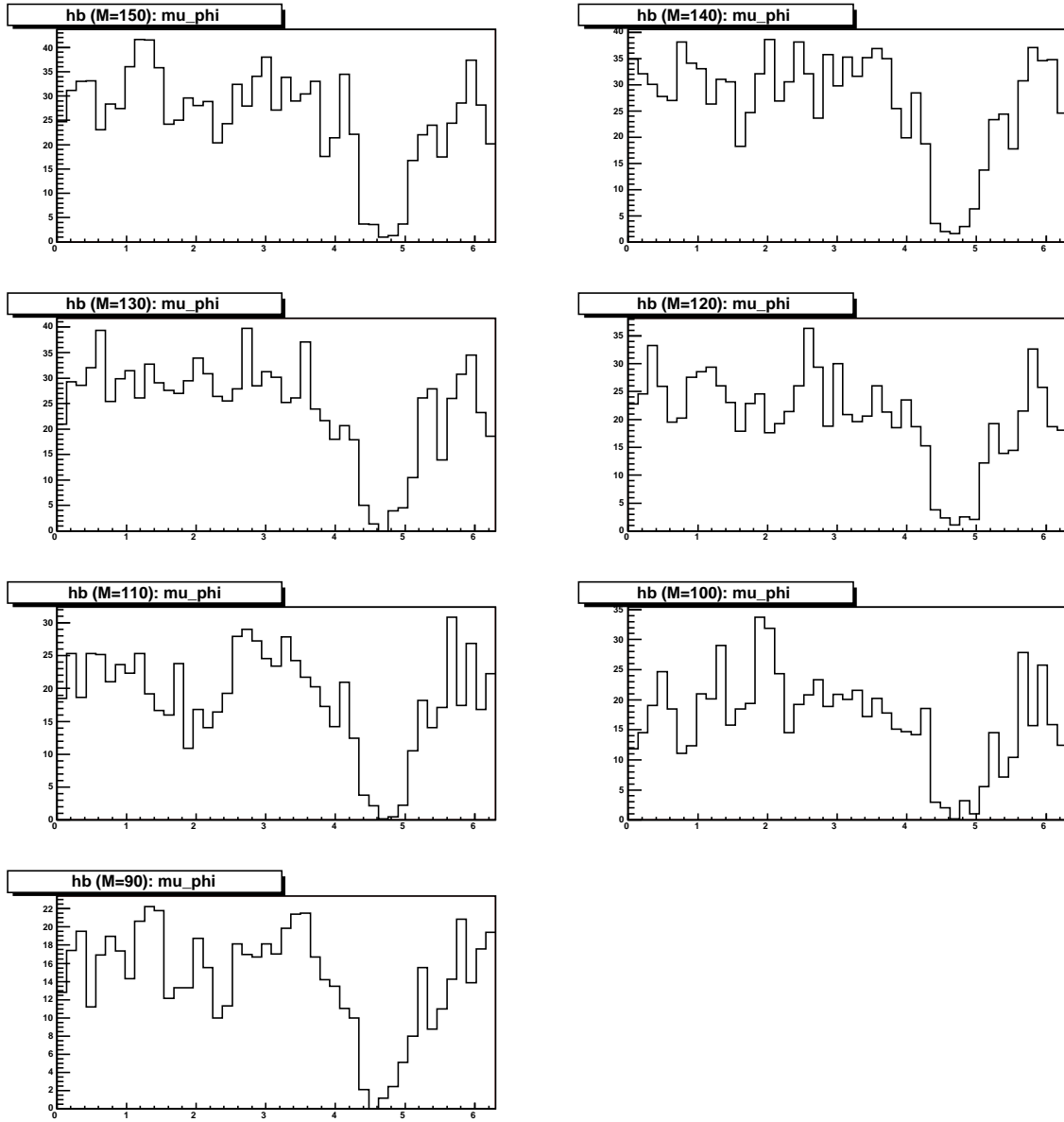
Figure 4.10. Signal Muon ϕ distribution for the different Higgs masses (Pythia Monte Carlo).
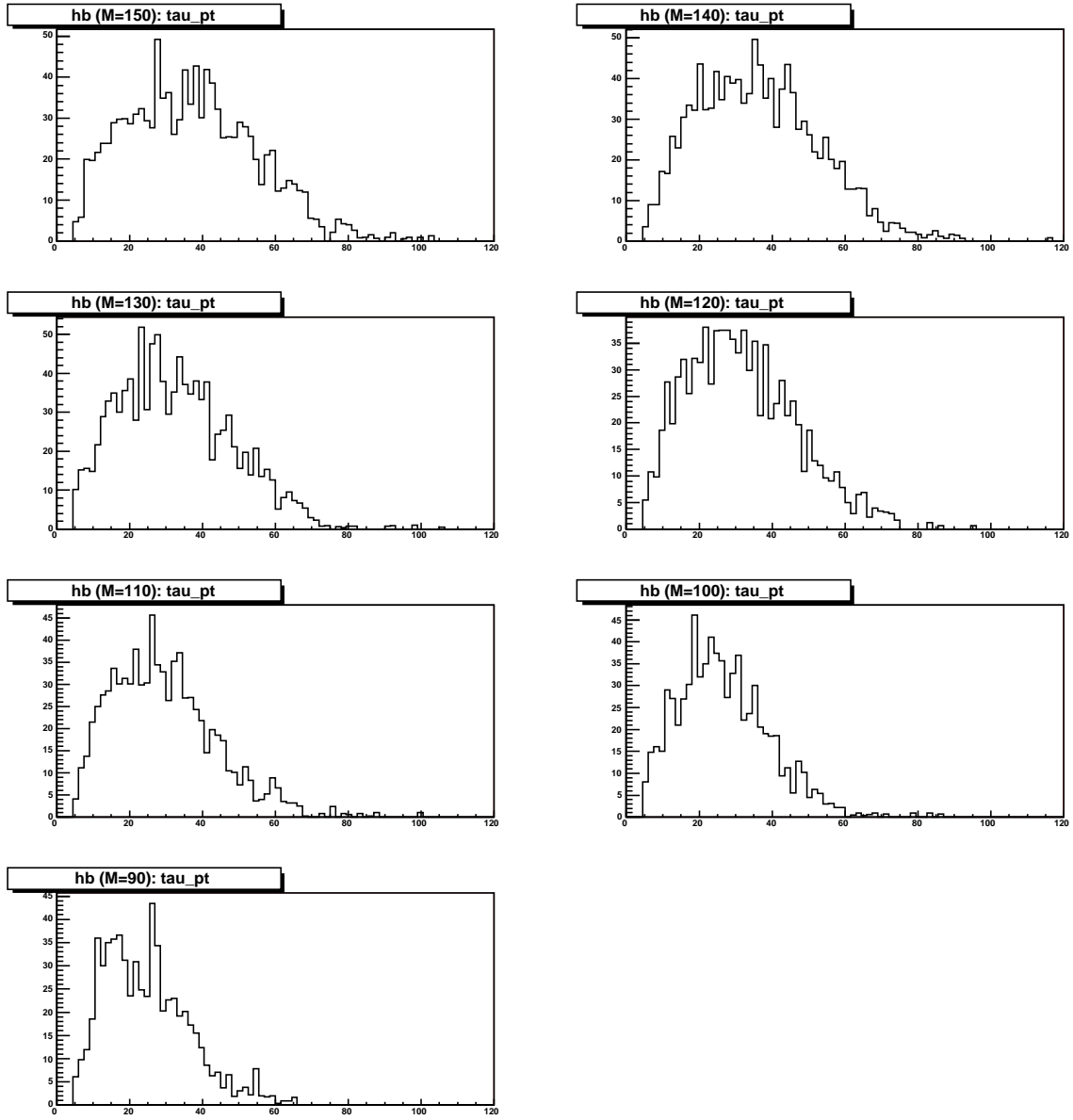
Figure 4.11. Signal Hadronic Tau E_T distribution for the different Higgs masses (Pythia Monte Carlo).
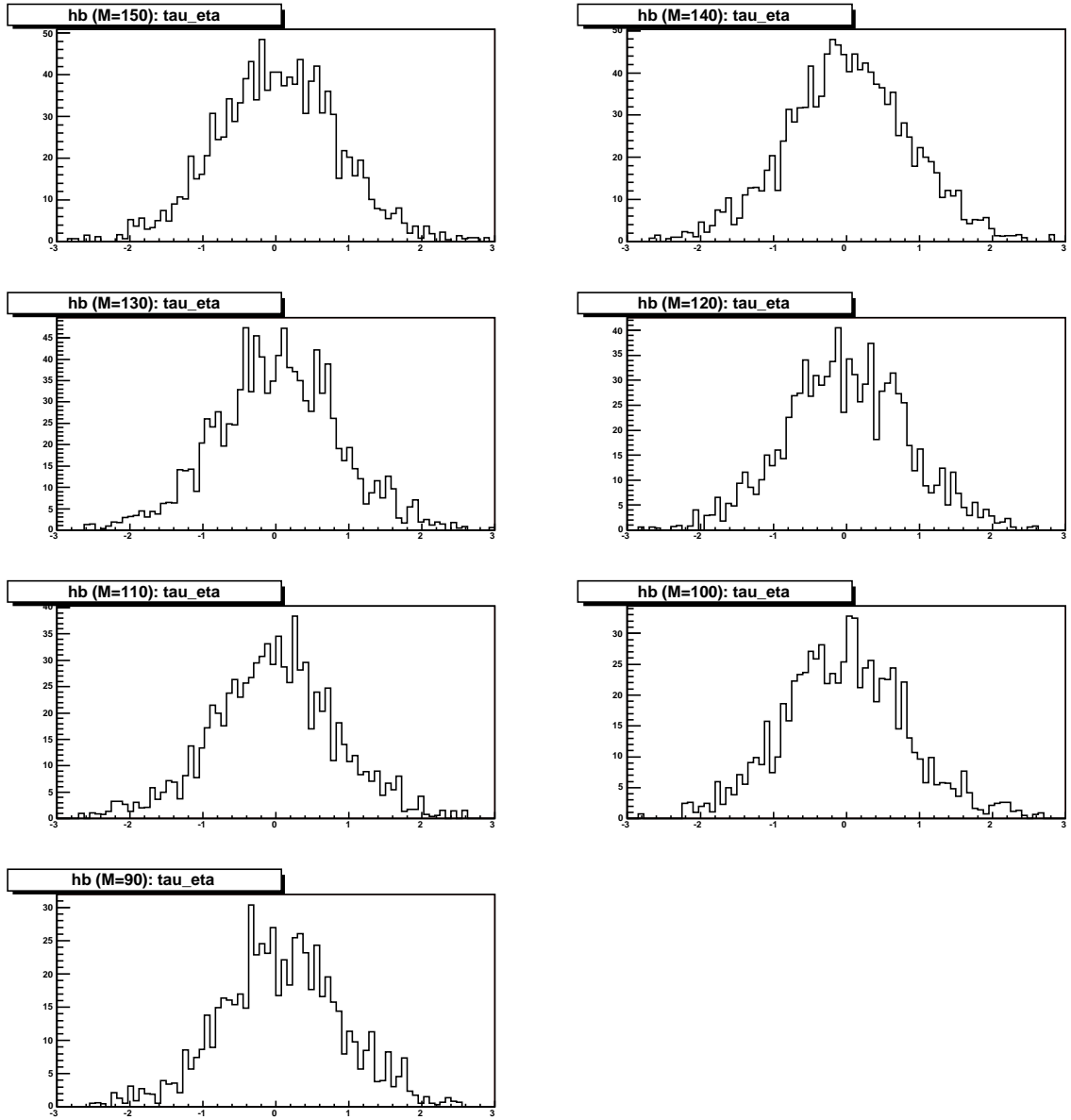
Figure 4.12. Signal Hadronic Tau η distribution for the different Higgs masses (Pythia Monte Carlo).
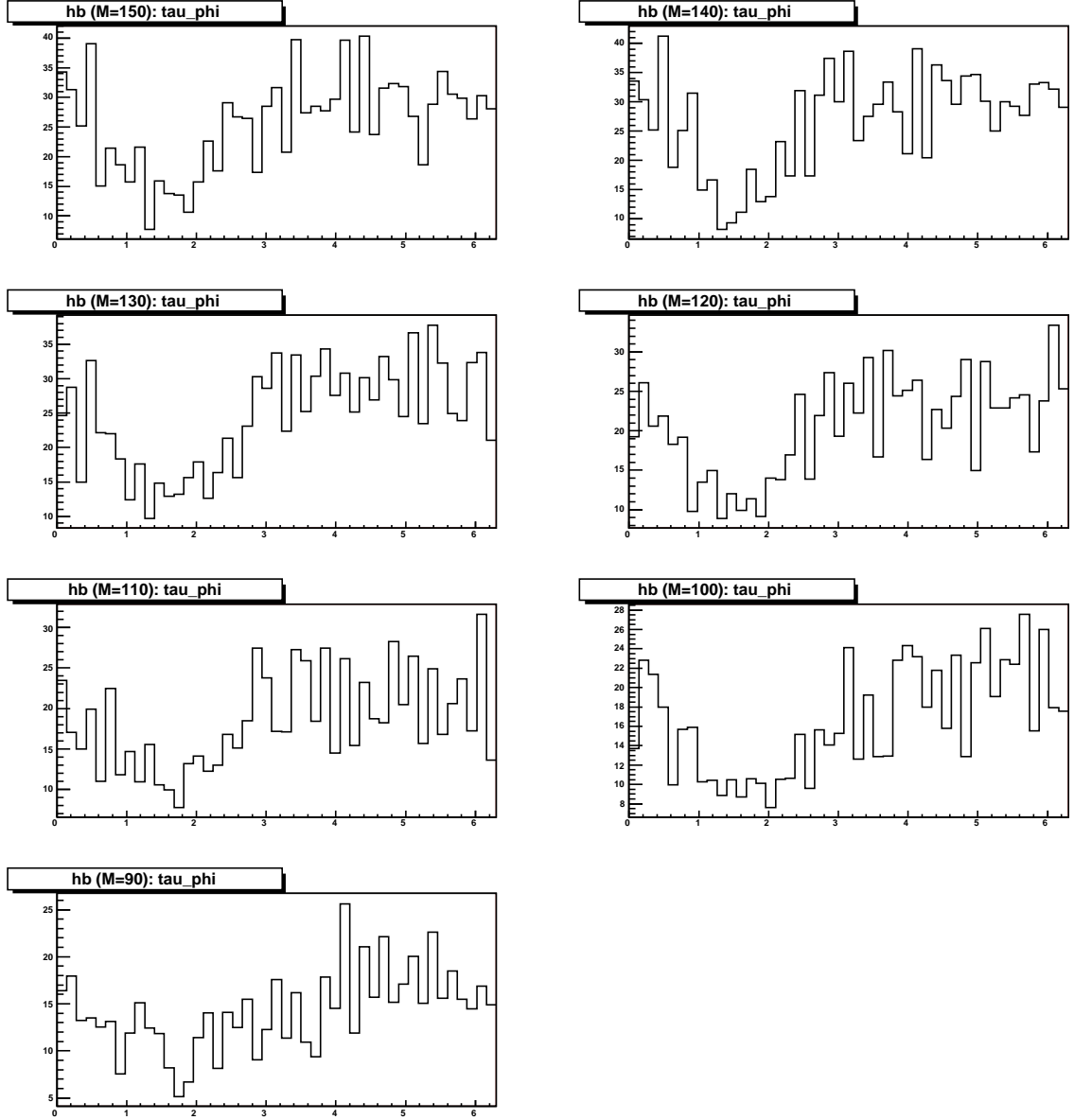
Figure 4.13. Signal Hadronic Tau ϕ distribution for the different Higgs masses (Pythia Monte Carlo). The deficit of events around 1.5 rad is a direct consequence of the back-to-back requirement between the μ and the τ_h, and the related deficit of muons around 4.5 rad.
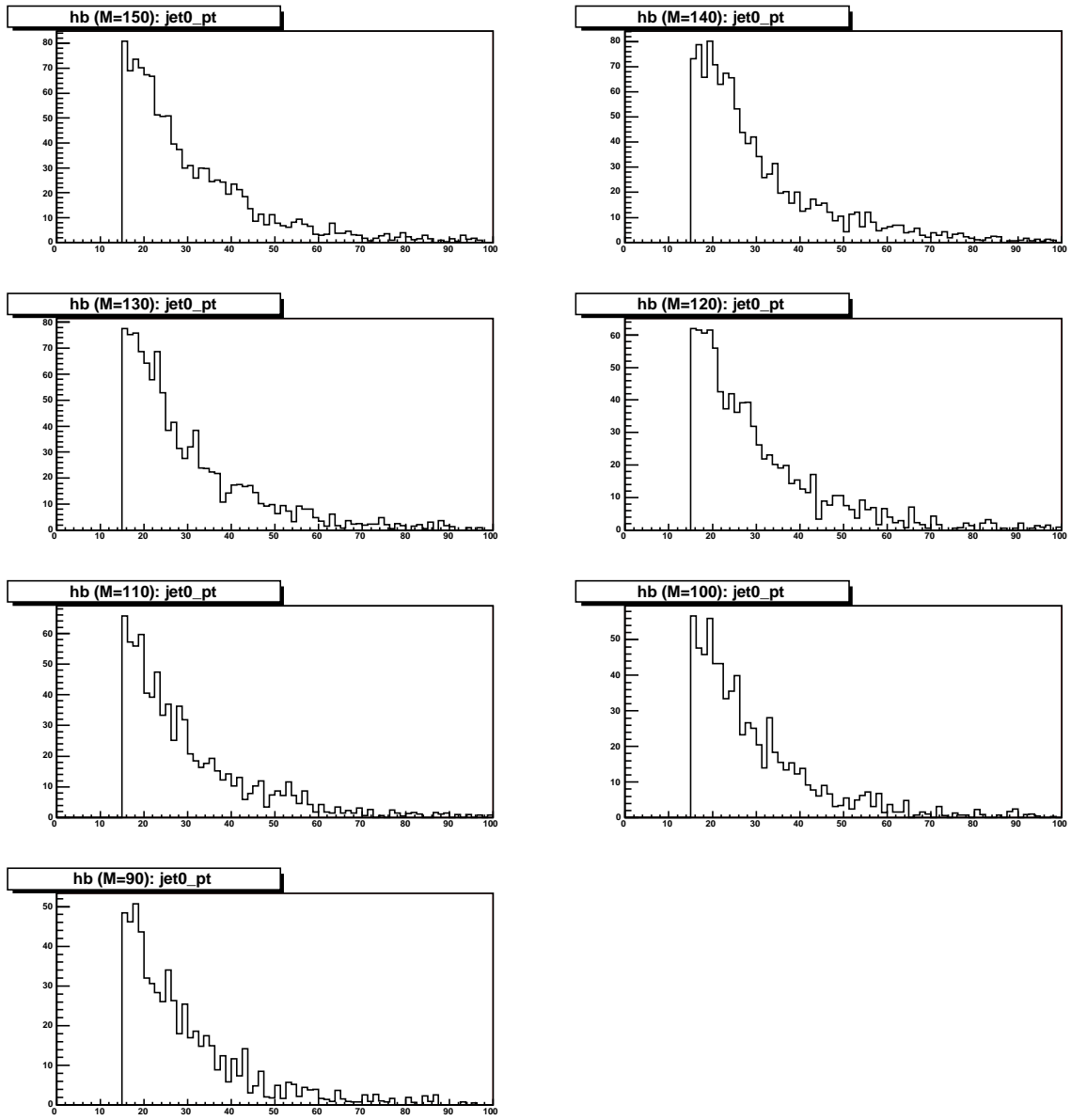
Figure 4.14. Signal Leading Jet E_T distribution for the different Higgs masses (Pythia Monte Carlo).
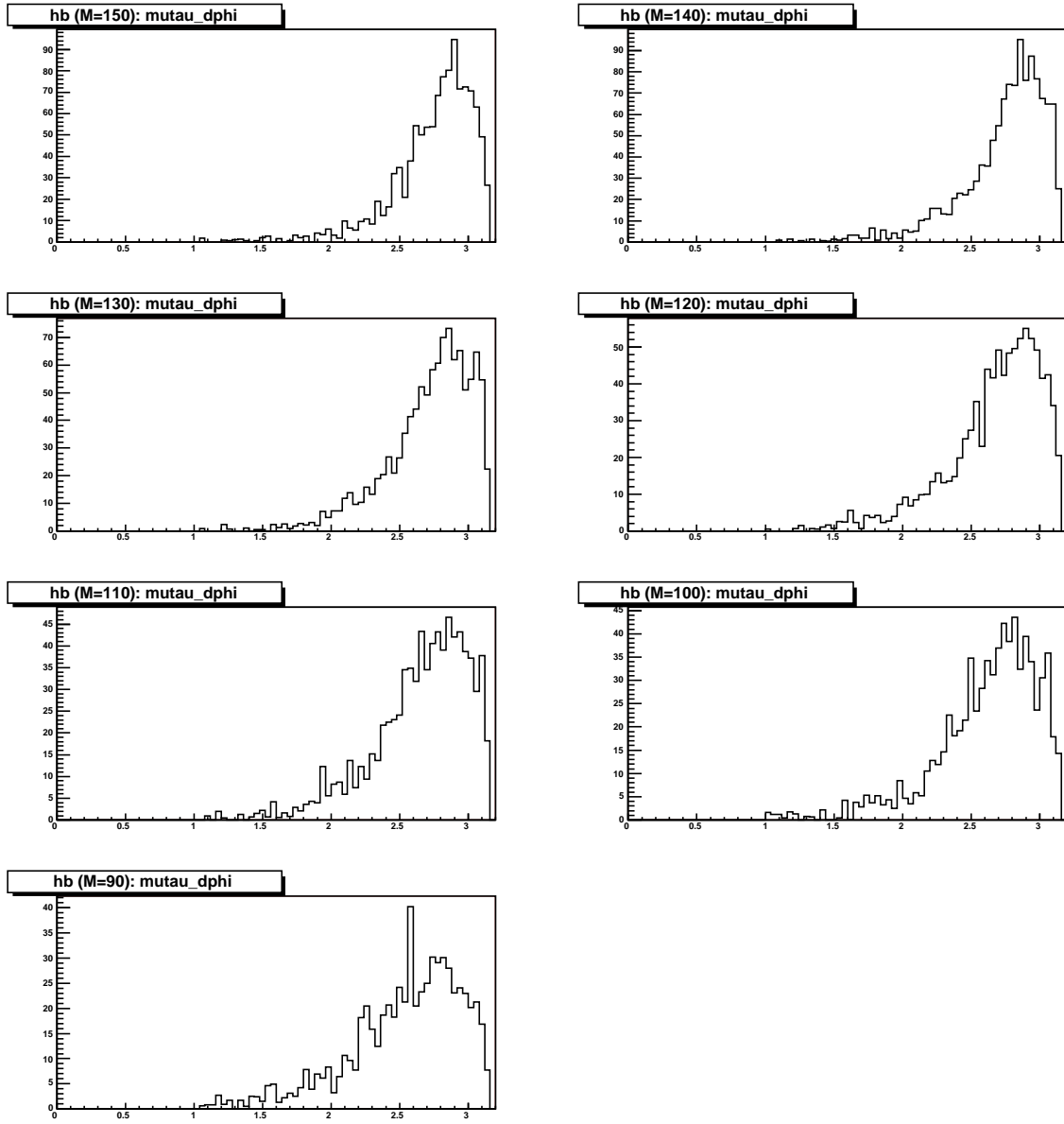
Figure 4.15. Signal $\Delta\phi$ between μ and τ_h distribution for the different Higgs masses (Pythia Monte Carlo).
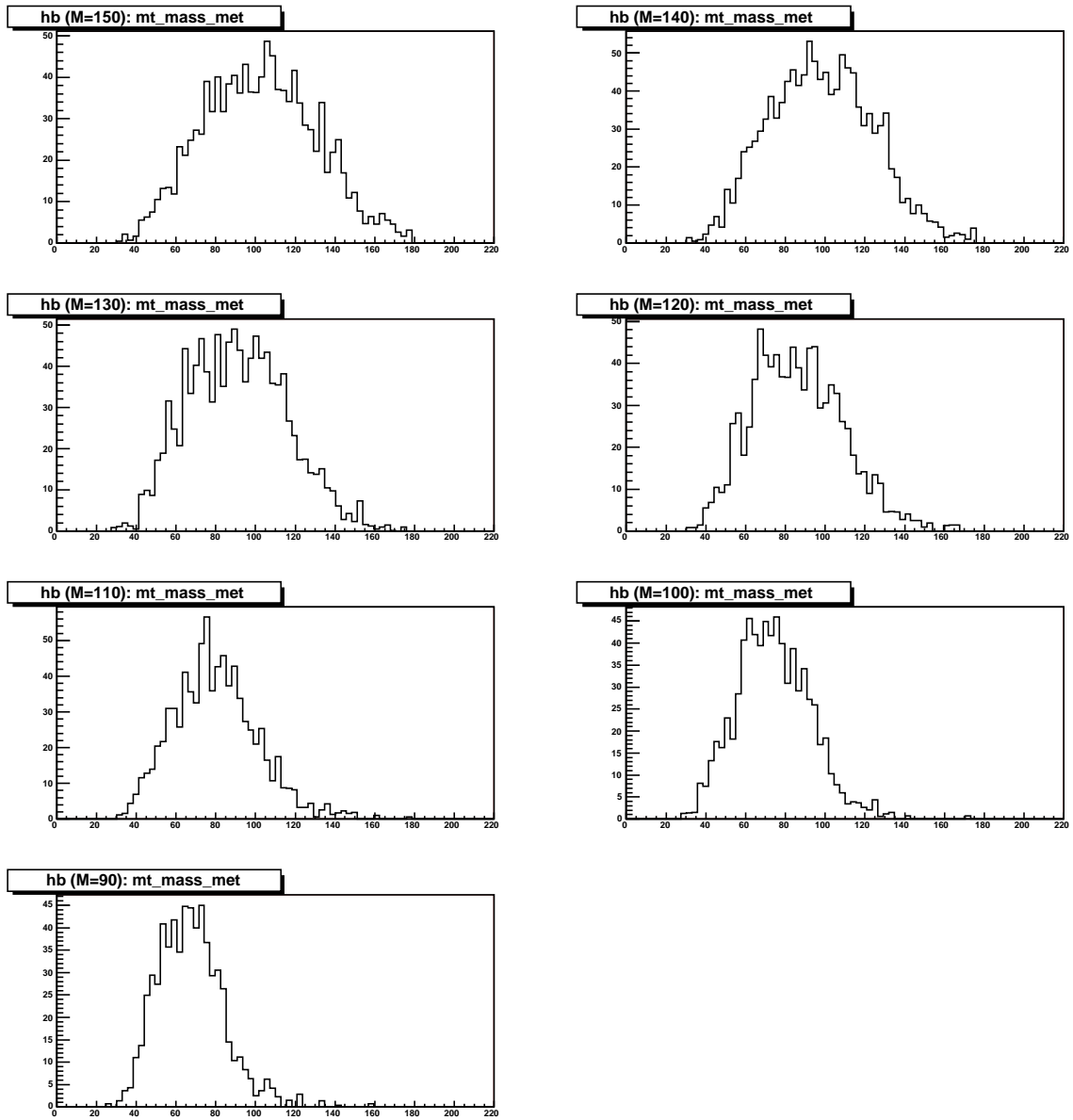
Figure 4.16. Signal invariant mass constructed from μ, τ_h and missing E_T distribution for the different Higgs masses (Pythia Monte Carlo).

4.6   Backgrounds

There are three major backgrounds for the $bh \to b\mu\tau_h$ process. These are QCD multijet production, $Z + (b)jets \to \mu\tau_h + (b)jets$, and $t\bar{t} \to b\bar{b}\mu\tau_h$.

There is also background that originates from $W + 2(bc)jets \to \mu + 2(bc)jets$ and WW production, but this is heavily suppressed by τ-ID and/or by b-tagging. The $W + 2(bc)jets$ and WW backgrounds were estimated from Monte Carlo. Backgrounds originating from WZ and ZZ production are already included in the $Z + (b)jets$ estimation from the data (because they contain a Z boson); therefore, they are not taken separately from Monte Carlo.

4.6.1   QCD estimation

A QCD event with three or more jets can have an isolated muon from a misreconstructed jet, a fake τ_h, and a real or fake b-jet. Since the sign of a fake muon is not correlated with the sign of a fake τ_h, the QCD background tends to have equal amounts of opposite sign (OS) and same sign (SS) $\tau\tau$ events. Other backgrounds (as for example $W + jets$, where there is a real, isolated muon but a jet fakes a τ_h) also contribute to the number of SS events. In contrast, the signal should contain only opposite sign $\tau^+\tau^-$ events coming from the Higgs decay.

To estimate the number of QCD events out of the total number of SS events, first the *QCD fake rate* was measured using event sample with a fake muon, i.e., a muon that fails the isolation criteria:

$$QCD\ fake\ rate = \left(\frac{N_{SS,NN_\tau > minNN_\tau}}{N_{SS,NN_\tau > 0.4}} \right)_{non-isolated\ \mu}. \tag{4.1}$$

The amount of the QCD background in the data sample can be estimated, by multiplying the number of SS events, with an isolated muon, before the NN_τ cut,

corrected for the non-QCD backgrounds (taken from MC), by the QCD fake rate:

$$N_{QCD,SS} = (N_{data} - N_{MC})_{SS,NN_\tau>0.4,isolated\,\mu} \cdot (QCD\ fake\ rate). \qquad (4.2)$$

In the above, we have assumed that the QCD background contains precisely equal amounts of OS and SS events. In order to test this assumption, a sample with a fake (i.e., non-isolated) muon and a fake τ_h-candidate was created. Fake tau is defined as a τ_h-candidate with $0.4<NN_\tau<0.8$. The E_T distributions for the leading jet and the τ_h-candidate in this sample are shown in Figure 4.17. The OS and SS distributions have indeed similar shapes, but the total amount of OS events exceeds the amount of SS events by a factor of 4-9%, depending on the τ_h type (see Table 4.1). Therefore, when estimating the QCD background in the data using Eq. (4.2), the number of SS events are corrected by the above factor:

$$N_{QCD,OS} = N_{QCD,SS} \cdot \left(\frac{OS}{SS}\right)_{non-isolated\,\mu,fake\,\tau}. \qquad (4.3)$$

For comparison, the corresponding OS and SS plots for the signal candidate events (i.e., with the muon isolation cuts and the τ_h-candidate high NN_τ cuts) are shown in Figure 4.18. Requiring $E_T^\tau > 14$ GeV removes a significant amount of the low-E_T QCD background.

Finally, the estimated number of QCD multijet OS events is multiplied by the b-tagging rate measured in the QCD sample. The b-tagging rate is defined as the fraction of events with at least one taggable jet that have at least one b-tagged jet. The measured b-tagging rates in the QCD sample for the three τ_h types are given in Table 4.1.
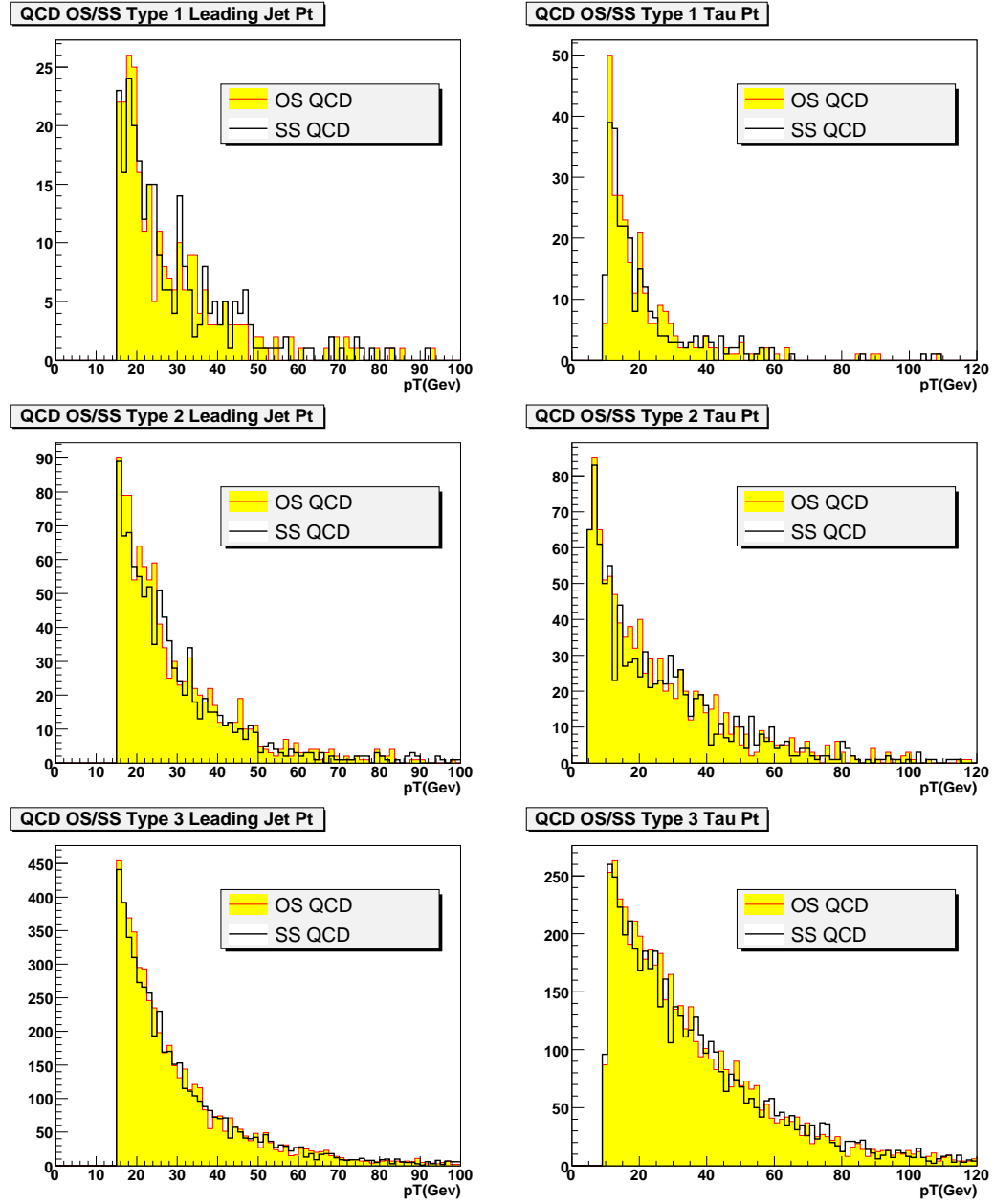
Figure 4.17. Leading jet and τ_h-candidate E_T distributions for the sample with the fake μ and τ.

89
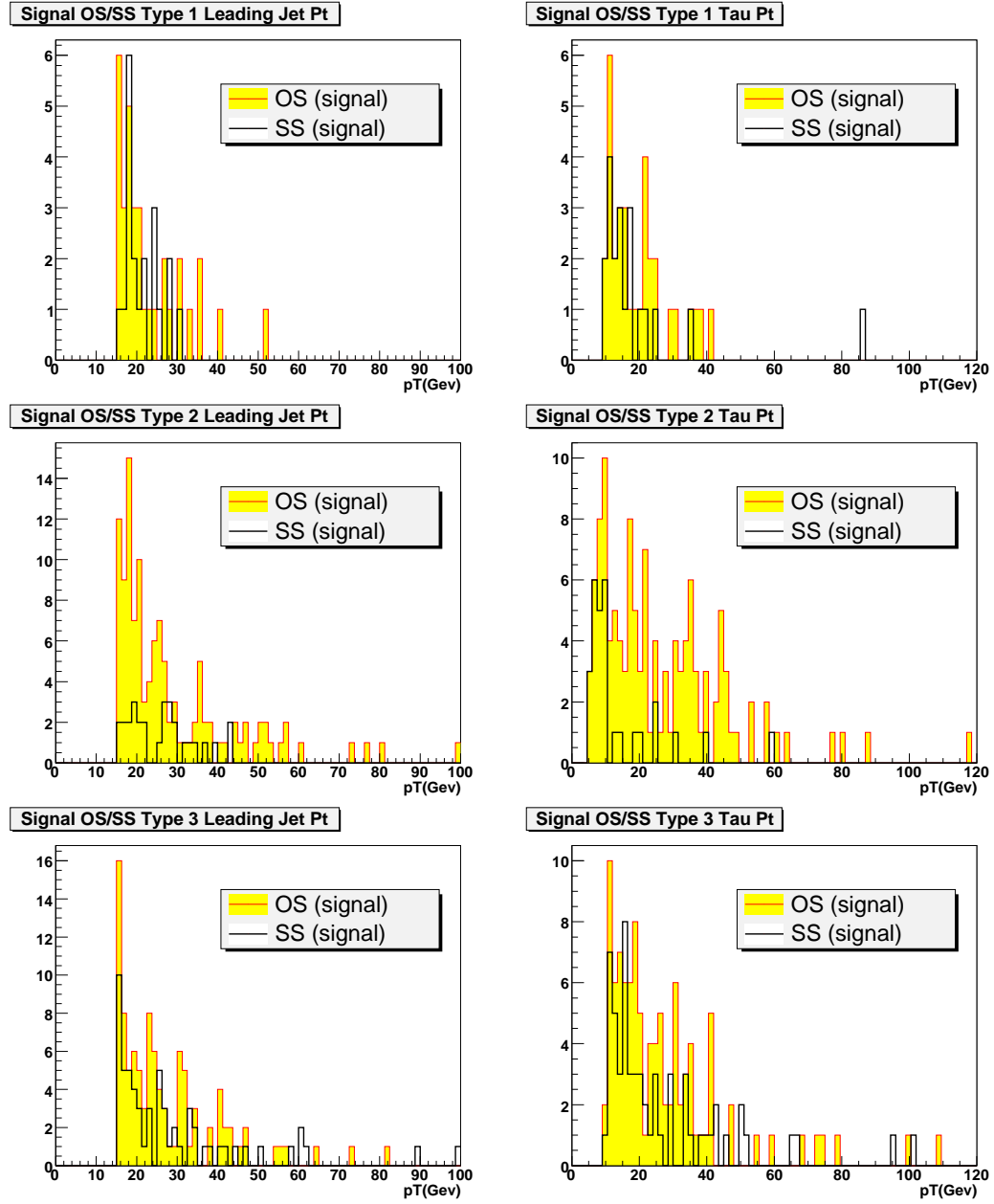
Figure 4.18. Leading jet and τ_h-candidate E_T distributions for the sample with the real μ and τ.

TABLE 4.1

OS VS SS ASYMMETRY AND b-TAGGING RATE IN THE QCD DATA
SAMPLE

	Type 1	Type 2	Type 3
QCD OS/SS ratio	1.07±0.12	1.09±0.07	1.04±0.02
QCD b-tag rate (%)	7.2±1.5	5.4±0.7	8.5±0.32

4.6.2 Data vs Monte Carlo

As a cross-check, we compare some kinematic distributions between the data and the simulation. The data selection used for this comparison is the same as in 4.4 with the exception of not requiring a jet in the event. Figure 4.19 shows the comparison for the muon p_T, hadronic tau p_T, missing E_T of the event, and invariant mass of the $(\mu, \tau_h, \not{E}_T)$ system. For this comparison, all cross sections are taken from Monte Carlo:

- $\sigma(Z \to \tau^+\tau^-) = 254$ pb
- $\sigma(Z \to \mu^+\mu^-) = 254$ pb
- $\sigma(W + j) = 840$ pb
- $\sigma(t\bar{t} \to dilepton) = 0.61$ pb
- $\sigma(t\bar{t} \to l + jet) = 0.82$ pb

Figures 4.20 and 4.21 show the effect of systematic uncertainties on the background prediction. There is an 1.7σ discrepancy between data and Monte Carlo, which can be attributed to the tau energy scale. There is no available tau energy scale correction for p14 data. To account for that, an 10% systematic uncertainty on acceptances taken from MC (signal and backround) were assigned (see Sec. 4.8).

(a) Muon ϕ (b) Hadronic tau ϕ

(c) Muon η (d) Hadronic tau η

(e) Muon p_T (f) Hadronic tau p_T

(g) Missing E_T (corrected for the muon)   (h) Invariant mass
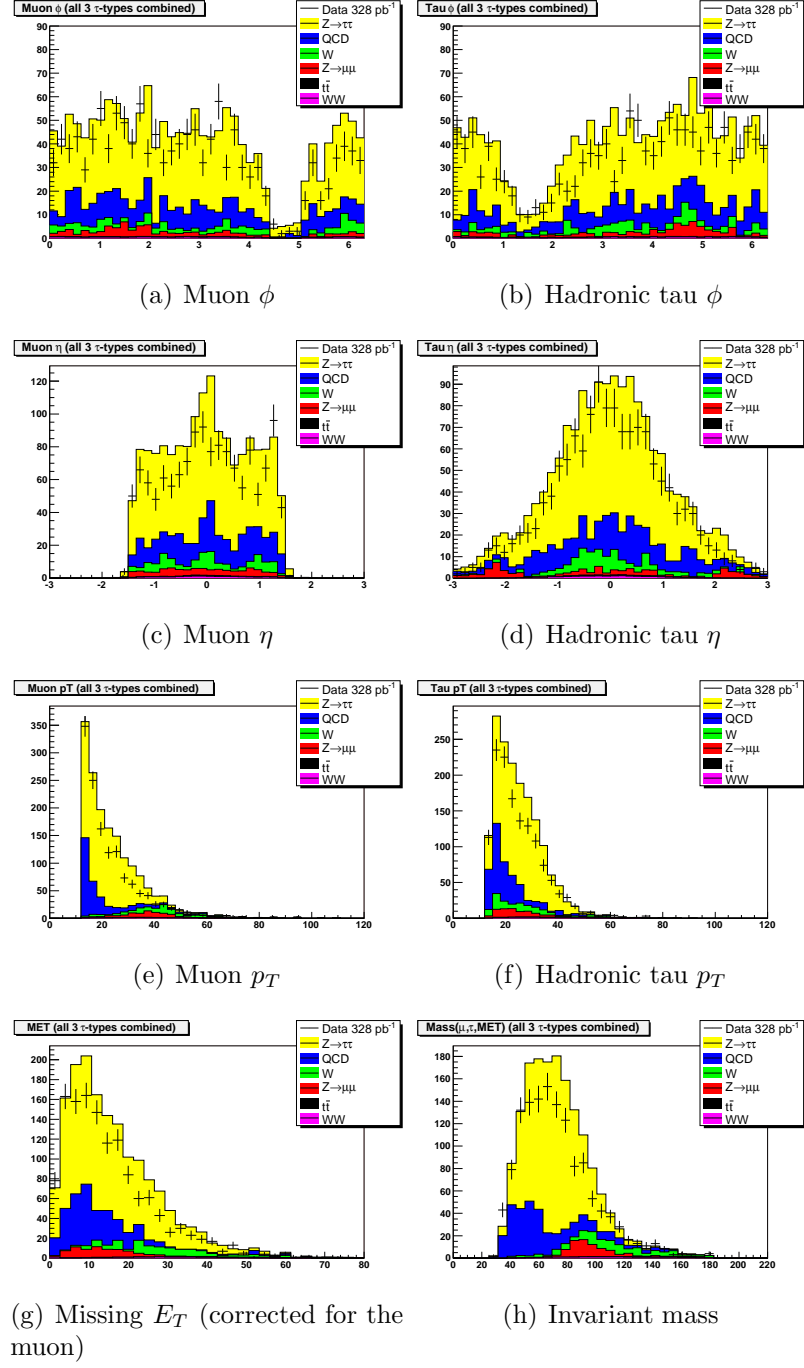
Figure 4.19. Comparison of kinematic distributions between data and Monte Carlo.

(a) Muon ϕ (b) Hadronic tau ϕ

(c) Muon η (d) Hadronic tau η

(e) Muon p_T (f) Hadronic tau p_T

(g) Missing E_T (corrected for the muon)   (h) Invariant mass

Figure 4.20. Effect of -1σ systematic uncertainty on the comparison of the kinematic distributions between data and Monte Carlo.

94

(a) Muon ϕ

(b) Hadronic tau ϕ

(c) Muon η

(d) Hadronic tau η

(e) Muon p_T

(f) Hadronic tau p_T

(g) Missing E_T (corrected for the muon)

(h) Invariant mass
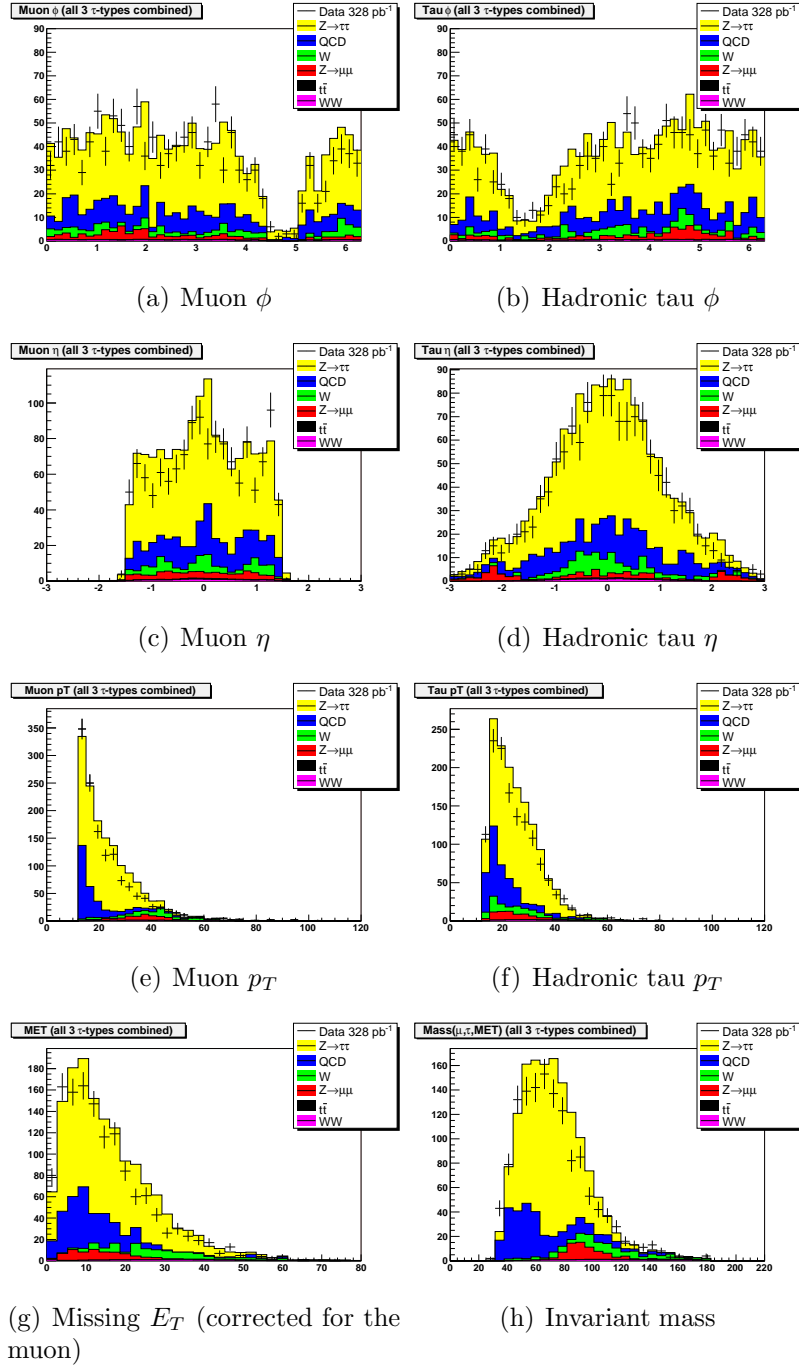
Figure 4.21. Effect of $+1\sigma$ systematic uncertainty on the comparison of the kinematic distributions between data and Monte Carlo.

4.6.3 Z+(b)jets

Production of a Z with an associated b-jet is a physical background for the bh process. Both $Z \to \mu\mu$ (with one muon faking a hadronic tau) and $Z \to \tau\tau \to \mu\tau_h$ decays contribute to this background. The b-tagging rate is the same in both cases; therefore, the contribution from these two channels can be estimated together. In addition, light-quark jets associated with a Z can be mistagged as b-jets.

The contribution from both real and fake b-jet backgrounds, in either Z decay channel, is estimated by measuring the b-tagging rate in $Z + jets \to \mu^+\mu^- + jets$ events in the data. Using the same $Z + jets \to \mu\mu + jets$ that was used for the taggability parametrization (see Sec. 4.4.4), a b-tagging rate was measured to be 0.025 ± 0.004 . $\mu^+\mu^-$ invariant mass distributions of the sample used for measuring b-tagging rate in data are shown on Figure 4.22. To reduce non Z contribution (such as $t\bar{t}$), events which pass the $80 < M_{\mu^+\mu^-} < 100$ mass window cut were used for b-tagging ratio calculation.

This measured b-tagging rate is then applied to the estimated number of $Z + jets \to \mu\tau_h + jets$ events in the data, which is calculated as:

$$N_{Zj,OS} = N_{OS} - N_{QCD,OS} - (N_{t\bar{t}} + N_{W2j} + N_{WW})_{OS} - N_{signal,OS} , \qquad (4.4)$$

where N_{OS} is the number of OS events events in the data, $N_{QCD,OS}$ is taken from Eq. (4.3), and the rest of the backgrounds, as well as the signal, are estimated from MC. All variables in Eq. (4.4) refer to number of events *before* b-tagging. Then:

$$N_{Zb,OS} = N_{Zj,OS} \cdot (b-tagging\ rate) . \qquad (4.5)$$

4.6.4 $t\bar{t}$ background

After b-tagging, the $t\bar{t} \to \mu\tau_h + b\bar{b}$ is the largest background. $t\bar{t}$ events have two high p_T b-jets, a high p_T muon and a high p_T hadronic tau. By contrast, b-jets in
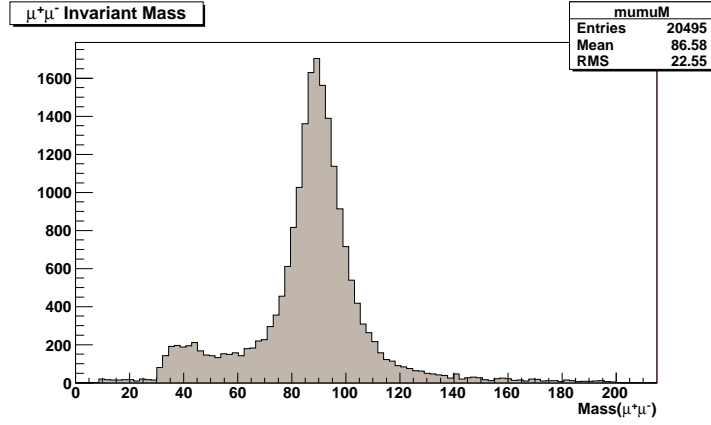
(a) $\mu^+\mu^-$ Mass
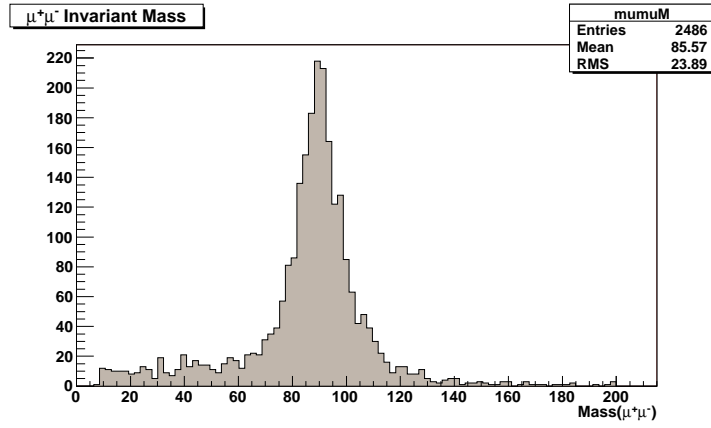
(b) $\mu^+\mu^-$ Mass, after taggable jet is found
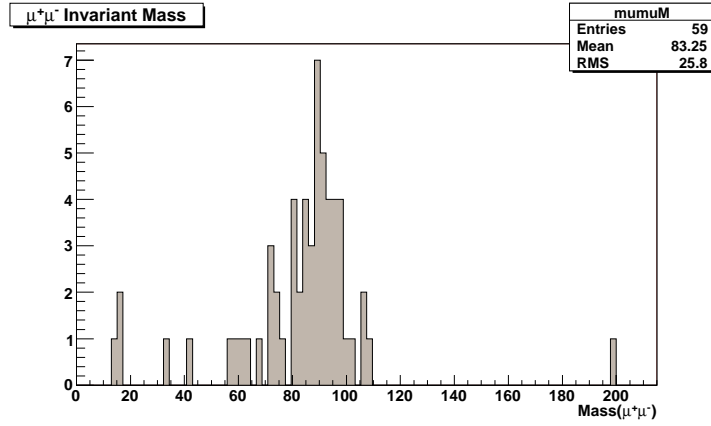
(c) $\mu^+\mu^-$ Mass, after b-jet is found

Figure 4.22. Invariant mass of the $\mu^+\mu^-$ pairs before requiring taggable jet, after requiring taggable jet, and after b-tagging

97

the signal events have relatively low p_T. In order to remove the $t\bar{t}$ background, we use a kinematic neural network (KNN).

The KNN has four input variables and one hidden layer with nine neurons. The input variables are the following:

- htb: Sum of the E_T's of the jets in the event (excluding the τ-jet)
- mht: Missing HT constructed from the jets and selected μ and τ_h
- Njet: Number of jets in the event
- mutau_dphi: $\Delta\phi$ between μ and τ_h

The background sample used for training was $t\bar{t} \rightarrow \mu\tau_h$ events from a $t\bar{t} \rightarrow ll$ sample, which passed all selection cuts except b-tagging. The signal sample used for training was a mixture of $bh \rightarrow b\tau\tau \rightarrow b\mu\tau_h$ events with different Higgs masses, which also passed all cuts except b-tagging. The trigger weight (see Sec. 4.3.2) was used as a weight during the training. The KNN input variable distributions are shown in Figure 4.23. Figure 4.24 shows the absolute difference on the KNN output when each of the variables is changed by 1 rms. Also shown in this figure is the structure of the neural network. Figure 4.25 shows the KNN outputs for different Higgs masses.

The KNN was tried separately for each τ_h type (see Section 4.9.4). Events with type 1 and 3 τ's did not benefit from KNN; therefore, no cut was used for those types. A cut of KNN>0.4 was applied for events with type 2 τ's (which dominate the result).
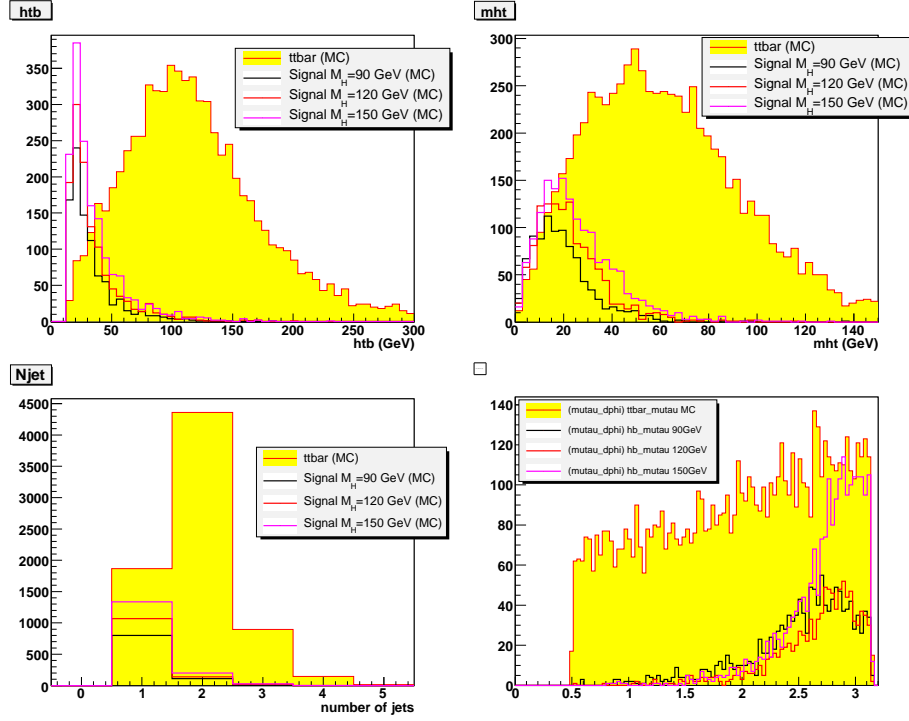
Figure 4.23. KNN input variable distributions for the signal and $t\bar{t}$ background training samples.
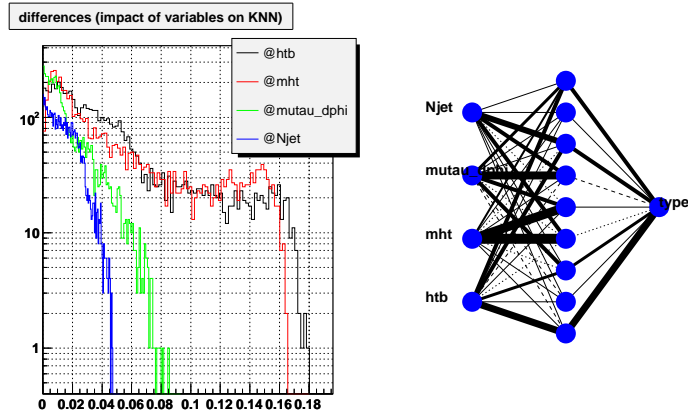
Figure 4.24. Absolute difference on the KNN output when each variable is changed by 1 rms (left), and structure of the KNN (right).
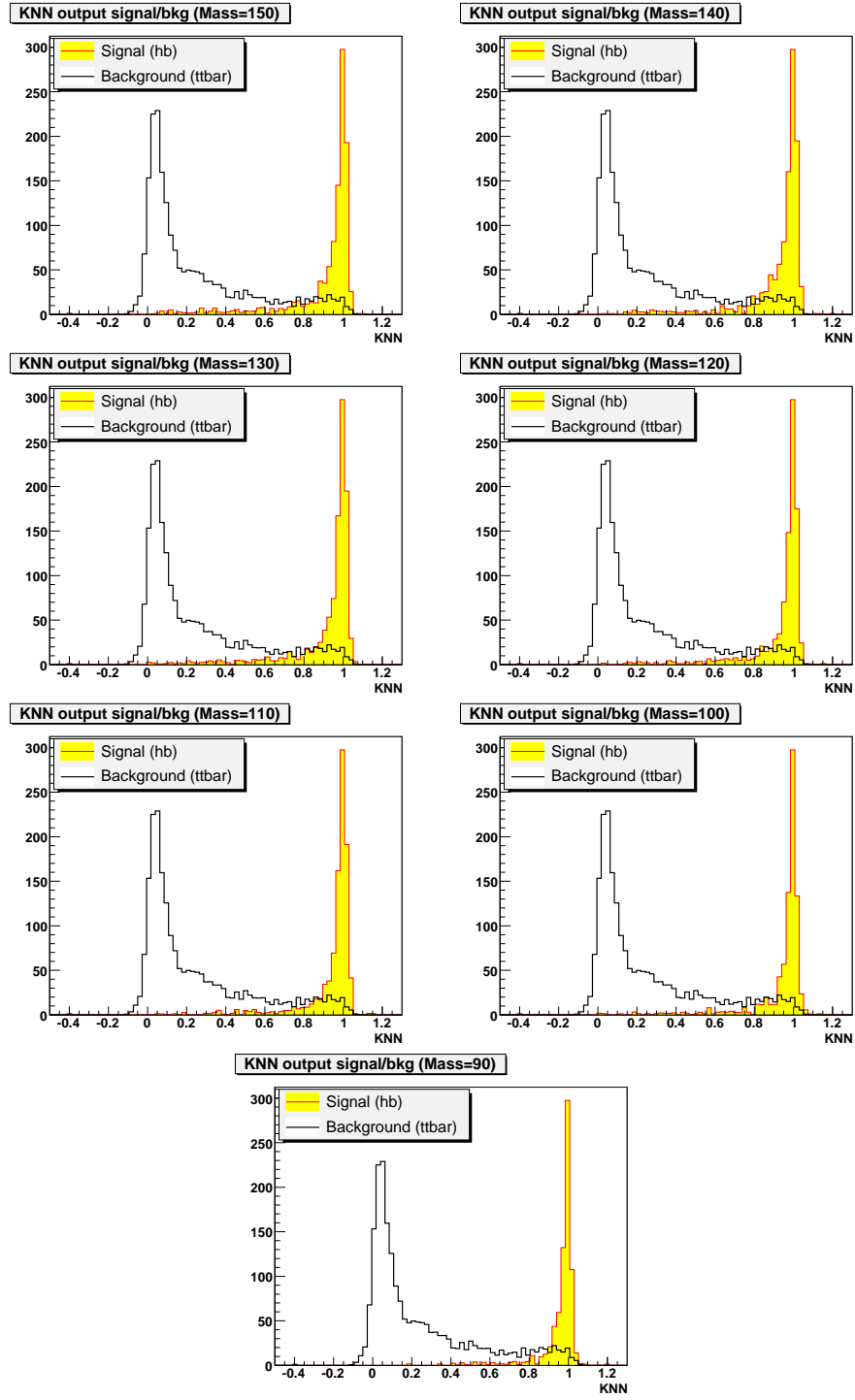
Figure 4.25. KNN output for different Higgs masses. Arbitrary normalization.

4.7 Event Cut Flow

The event yields after the various cuts in the data and MC are shown in Tables 4.2-4.4. The selection criteria are summarized below:

- PreSel: muon trigger requirement; $\Delta Z_{vtx} < 1$ cm for μ, τ_h and jet; cut 1 in Section 4.4.1; cuts 1-5 in Section 4.4.2; $NN_\tau > 0.3$.

- MuIso: muon isolation (cuts 2-4 in Section 4.4.1)

- Tau Pt: $E_T^\tau > 14$ GeV and τ_h type = 1,2,3

- dPhi: $|\phi_\mu - \phi_{\tau_h}| > 2.0$ (cut 6 in Section 4.4.2)

- Mass: 30<Mass<180 on the $(\mu, \tau_h, \not{E}_T)$ invariant mass

- Sign: Opposite Sign (OS) vs Same Sign (SS)

- Tau NN: final NN_τ cut (as described in Section 4.4.2)

- TAjet: at least one jet in the event satisfying all requirements in paragraph 4.4.3 and being taggable

- KNN: Kinematic Neural Network cut (as described in Section 4.6.4)

- btag: at least one b-tagged jet

TABLE 4.2

DATA AND MC CUT FLOW TABLE FOR τ_h TYPE 1

	Data OS	Data SS	bh(M=120)[1]	$t\bar{t}$ (di-l)	$t\bar{t}$ (l+jet)	W+jj(c/b)	WW
	328 pb^{-1}	328 pb^{-1}					
PreSel	209230	209230	442.2	200.37	268.94	97350.81	391.96
MuIso	21327	21327	108.4	72.31	79.41	6059.46	85.68
Mu Trig	21327	21327	92.3	53.21	56.15	4844.53	74.90
Tau Pt	766	766	58.5	37.01	38.36	2786.92	42.55
dPhi	658	658	4.6	1.47	0.35	49.94	2.59
Mass	637	637	4.4	0.80	0.17	27.89	1.64
Sign	424	213	4.4	0.37	0.14	23.56	1.26
TauNN	255	86	4.0	0.36	0.13	19.93	1.25
TAjet	24	9	1.7	0.35	0.06	8.76	1.17
KNN	24	9	1.7	0.34	0.06	1.87	0.08
bTAG	0	0	0.7	0.20	0.04	0.01	0.00

[1]numbers for the Higgs signal are normalized for $\tan\beta$=80

TABLE 4.3

DATA AND MC CUT FLOW TABLE FOR τ_h TYPE 2

	Data OS	Data SS	bh(M=120)[1]	$t\bar{t}$ (di-l)	$t\bar{t}$ (l+jet)	W+jj(c/b)	WW
	328 pb^{-1}	328 pb^{-1}	442.2	200.37	268.94	97350.81	391.96
PreSel	209230	209230	108.4	72.31	79.41	6059.46	85.68
MuIso	21327	21327	92.3	53.21	56.15	4844.53	74.90
Mu Trig	21327	21327	58.5	37.01	38.36	2786.92	42.55
Tau Pt	1852	1852	29.2	25.61	2.41	194.81	30.05
dPhi	1601	1601	28.2	13.42	1.22	110.45	19.35
Mass	1533	1533	28.0	6.44	0.74	88.64	14.91
Sign	1184	349	28.0	6.38	0.58	72.17	14.86
TauNN	773	104	25.2	6.16	0.22	27.54	14.43
TAjet	86	8	10.4	5.99	0.22	11.66	1.12
KNN	79	7	9.9	1.17	0.02	8.48	1.09
bTAG	1	0	3.9	0.56	0.01	0.07	0.01

[1] numbers for the Higgs signal are normalized for $\tan\beta$=80

TABLE 4.4

DATA AND MC CUT FLOW TABLE FOR τ_h TYPE 3

	Data OS	Data SS	bh(M=120)[1]	$t\bar{t}$ (di-l)	$t\bar{t}$ (l+jet)	W+jj(c/b)	WW
	328 pb^{-1}	328 pb^{-1}					
PreSel	209230	209230	442.2	200.37	268.94	97350.81	391.96
MuIso	21327	21327	108.4	72.31	79.41	6059.46	85.68
Mu Trig	21327	21327	92.3	53.21	56.15	4844.53	74.90
Tau Pt	21327	21327	58.5	37.01	38.36	2786.92	42.55
dPhi	9817	9817	16.6	7.91	33.67	1937.71	4.97
Mass	7940	7940	15.5	4.18	17.51	1111.38	3.27
Sign	7471	7471	15.4	1.78	9.35	900.36	2.63
TauNN	2719	2013	12.0	0.80	4.70	378.86	2.10
TAjet	323	128	7.6	0.10	0.20	18.90	1.13
KNN	30	18	3.1	0.10	0.20	8.54	0.09
bTAG	30	18	3.1	0.10	0.20	8.54	0.09
	2	2	1.2	0.07	0.11	0.28	0.00

---

[1]numbers for the Higgs signal are normalized for $\tan\beta$=80

4.8 Systematic Uncertainties

A summary of the systematical uncertainties for the signal and background prediction is shown in the Table 4.5. For backgrounds derived from data, the systematic errors result from the statistical errors of the background estimates.

For backgrounds derived from Monte Carlo, the following systematic errors are included in the calculations:

- The Jet Energy Scale uncertainty is estimated by moving the energy scale of all jets in each MC sample (signal and background) by $\pm 1\sigma$, and calculating the new acceptances [25]. Similarly for the Jet Reconstruction Efficiency uncertainty.

- A 10% uncertainty is assigned on the signal and backrounds taken from MC acceptances due to the missing τ ES correction.

- The TRF uncertainty is estimated in the same way as the JES uncertainty [24].

- The NN_τ uncertainty is taken from [26]. Since for type 3 taus we use a tighter NN_τ cut than in [26] (0.98 instead of 0.9), we rescale the systematic uncertainty from 3.2% to 9%. This change has a negligible effect on the cross section limit.

- The statistical uncertainty of the overall trigger efficiency in the data (1.1%) is used as the muon trigger efficiency systematic uncertainty.

- The luminosity uncertainty is taken to be equal 6.1%.

- The MC cross sections and their uncertainties are taken as follows:

  - The signal cross section is taken from [27] and a 10% uncertainty taken from [27] is assigned to it due to the uncertainty in the Parton Distribution Function.
  - The $t\bar{t}$ cross section is taken from ALPGEN, but the relative uncertainty on it is taken from [28].
  - The $W + jj$ and $W + b\bar{b}$ cross sections are taken from the MCFM calculations (in NLO) [29]. Their uncertainties are set to 30%, which corresponds to the difference between LO and NLO MCFM cross sections.
  - The WW cross section is taken from MCFM and a 20% uncertainty is assigned to it, which corresponds to the difference between the LO and NLO cross sections.

TABLE 4.5

SYSTEMATIC UNCERTAINTIES

	Type 1		Type 2		Type 3	
	Signal	Bkgd	Signal	Bkgd	Signal	Bkgd
Luminosity	6.1%	0.7%	6.1%	0.8%	6.1%	0.05%
Trigger	1.1%	0.13%	1.1%	0.14%	1.1%	0.01%
NN$_\tau$	3.2%	0.37%	3.2%	0.4%	9.0%	0.07%
Jet Reco Eff.	9.0%	0.2%	7.5%	1.7%	6.5%	1.3%
JES syst.	10.0%	1.5%	7.6%	4.0%	7.6%	0.6%
τ ES syst.	10%	1.2%	10.0%	1.3%	10.0%	0.06%
TRF syst.	5.0%	1.2%	5.0%	1.4%	5.2%	1.7%
Z+jet b-rate		4.8%		9.5%		2.5%
QCD fake rate		2.6%		0.6%		2.1%
QCD SS stat.		8.8%		2.3%		3.5%
QCD OS/SS ratio		3.6%		0.6%		0.9%
QCD b-rate		10.3%		2.4%		2.2%
MC stat.	13.0%	3.8%	5.3%	2.5%	9.0%	5.7%
MC x-section	10.0%	2.6%	10.0%	2.5%	10.0%	3.3%

4.9 Cross Section Limit

4.9.1 Method

The estimated number of events from the various backgrounds and the observed number of events in the data for the three τ_h types are shown in Table 4.6. The signal acceptance, number of expected signal events, total number of estimated background events, and number of observed events, for each Higgs mass and each of the three τ_h types, are shown in Tables 4.7-4.9.

TABLE 4.6

ESTIMATED BACKGROUNDS AND OBSERVED NUMBER OF EVENTS
FOR THE THREE HADRONIC τ TYPES

Sample	Type 1	Type 2	Type 3
QCD	0.60 ± 0.22	0.48 ± 0.14	0.95 ± 0.16
Z+jet	0.34 ± 0.09	1.50 ± 0.27	0.25 ± 0.08
$t\bar{t}$ (di-l)	0.20 ± 0.037	0.56 ± 0.14	0.07 ± 0.017
$t\bar{t}$ (l+jet)	0.035 ± 0.019	0.009 ± 0.009	0.11 ± 0.04
W+jj	0.008 ± 0.005	0.073 ± 0.036	0.28 ± 0.12
W+cc	0.001 ± 0.001	0	0
W+bb	0	0	0
WW	0	0.014 ± 0.004	0
Total Background	1.18 ± 0.19	2.63 ± 0.31	1.66 ± 0.14
Observed	0	1	2

TABLE 4.7

TYPE 1 SIGNAL ACCEPTANCES AND EVENT YIELDS

	$M_H = 90$	$M_H = 100$	$M_H = 110$	$M_H = 120$
Sig. Accept. (%)	0.077±0.02	0.12±0.03	0.13±0.03	0.15±0.03
Expected Signal[1]	1.05±0.3	1.1±0.27	0.81±0.20	0.68±0.15
Total Bkgd	1.18±0.19	1.18±0.19	1.18±0.19	1.18±0.19
Observed	0	0	0	0
	$M_H = 130$	$M_H = 140$	$M_H = 150$	
Sig. Accept. (%)	0.16±0.037	0.19±0.037	0.18±0.036	
Expected Signal	0.51±0.12	0.44±0.09	0.30±0.06	
Total Bkgd	1.18±0.19	1.18±0.19	1.18±0.19	
Observed	0	0	0	

---

[1]The expected signal is normalized to the expected cross section at $\tan\beta = 80$ [27].

108

TABLE 4.8

TYPE 2 SIGNAL ACCEPTANCES AND EVENT YIELDS

	$M_H = 90$	$M_H = 100$	$M_H = 110$	$M_H = 120$
Sig. Accept. (%)	0.46±0.085	0.59±0.01	0.71±0.12	0.87±0.14
Expected Signal[1]	6.4±1.2	5.4±1.0	4.5±0.8	3.9±0.68
Total Bkgd	2.63±0.31	2.63±0.31	2.63±0.31	2.63±0.31
Observed	1	1	1	1
	$M_H = 130$	$M_H = 140$	$M_H = 150$	
Sig. Accept. (%)	0.93±0.15	1.2±0.18	1.2±0.2	
Expected Signal	2.9±0.51	2.7±0.45	2.1±0.35	
Total Bkgd	2.63±0.31	2.63±0.31	2.63±0.31	
Observed	1	1	1	

---

[1]The expected signal is normalized to the expected cross section at $\tan\beta = 80$ [27].

TABLE 4.9

TYPE 3 SIGNAL ACCEPTANCES AND EVENT YIELDS

	$M_H = 90$	$M_H = 100$	$M_H = 110$	$M_H = 120$
Sig. Accept. (%)	0.16±0.041	0.21±0.043	0.26±0.055	0.27±0.053
Expected Signal[1]	2.2±0.58	1.9±0.41	1.7±0.36	1.2±0.24
Total Bkgd	1.66±0.14	1.66±0.14	1.66±0.14	1.66±0.14
Observed	2	2	2	2
	$M_H = 130$	$M_H = 140$	$M_H = 150$	
Sig. Accept. (%)	0.35±0.067	0.32±0.066	0.38±0.074	
Expected Signal	1.1±0.22	0.71±0.15	0.63±0.13	
Total Bkgd	1.66±0.14	1.66±0.14	1.66±0.14	
Observed	2	2	2	

---

[1]The expected signal is normalized to the expected cross section at $\tan\beta = 80$ [27].

Upper limits for the production cross section times branching ratio are set using the modified frequentist approach [30]. In order to maximize the sensitivity, each τ_h type is treated as a separate channel. The differences in shape between signal and background are exploited by using the invariant mass distribution[1] of the hypothesized signal, expected background, and observed data in the calculation of the limit. In each channel, the mass distribution is split in three bins (see Section 4.9.2). Finally, the expected and measured limits are corrected for the branching ratio of one $\tau \rightarrow \mu$ and the other τ decaying hadronically (32%).

4.9.2   Invariant Mass

The invariant mass of the $(\mu, \tau_h, \not{E}_T)$ system is shown separately for each channel (i.e., τ_h-type) in Figure 4.26. In each channel, the mass distribution was split in three bins: 30-60, 60-85 and 85-180 GeV. The bin size was determined so as to allow enough statistics for the estimation of the QCD multijet SS events from the data.

4.9.3   Optimization of the NN$_\tau$ Selection

The cuts on NN$_\tau$ were optimized separately for each τ_h type, according to the following procedure:

- First, only type 2 τ's (where most of the signal comes from) are considered. The expected cross section limit as a function of the type-2 NN$_\tau$ cut is shown on Figure 4.27). Based on this plot, a cut of NN$_\tau$>0.8 for type 2 τ's was selected.

- Then, type-3 NN$_\tau$ cut is optimized based on the expected cross section limit when using type 2 and 3 τ's, with the type-2 NN$_\tau$ cut fixed at 0.8 (Figure 4.28). A cut of NN$_\tau$>0.98 for type 3 τ's was selected.

- Finally, the type-1 NN$_\tau$ cut was optimized based on the expected cross section limit when using all three τ types, with the type-2 and type-3 NN$_\tau$ cuts fixed at 0.8 and 0.98, respectively (Figure 4.29). A cut of NN$_\tau$>0.8 for type 1 τ's was selected.

---

[1]As mentioned earlier, the invariant mass was constructed from the 4-vector momenta of the μ, hadronic τ, and missing E_T of the event.
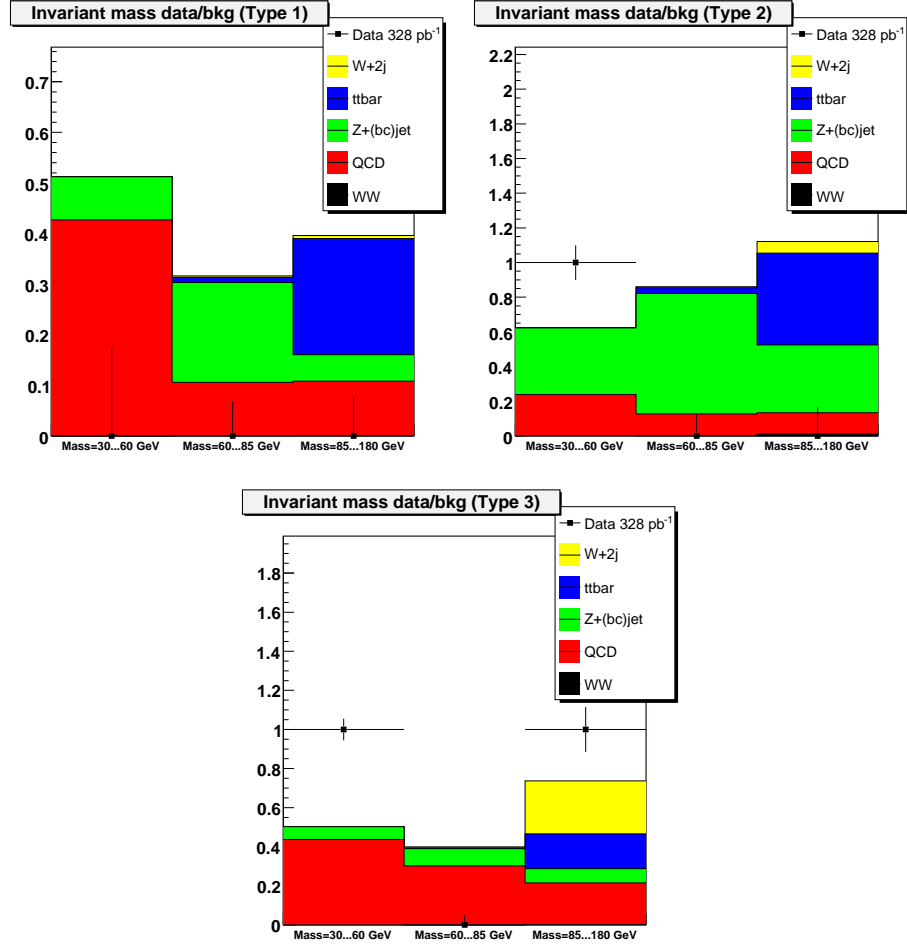
Figure 4.26. Invariant mass distributions for each τ_h type. Histograms show the various backgrounds, points show the data. Error bars on the data points indicate the uncertainty of the background estimation.
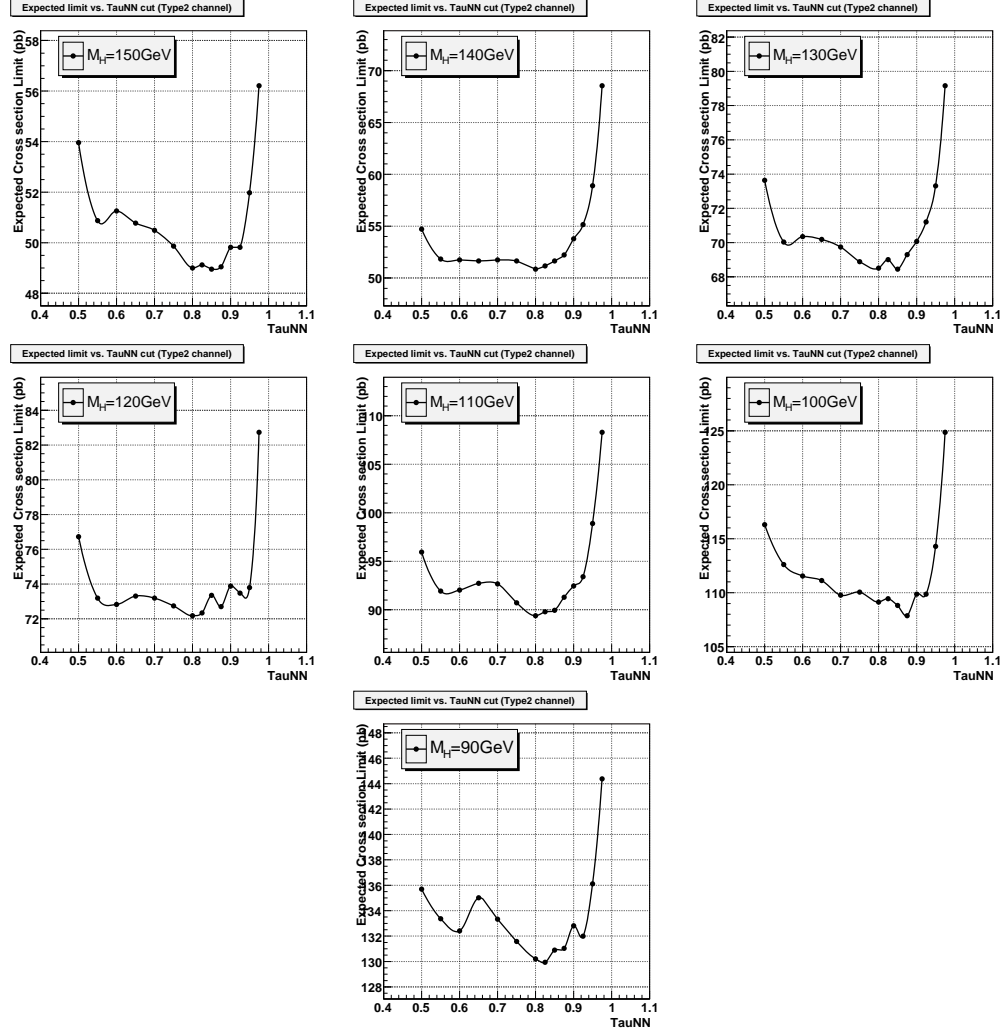
Figure 4.27. Expected cross section limit as a function of the NN_τ cut for type 2 τ's. Limit derived using only type 2 τ's.

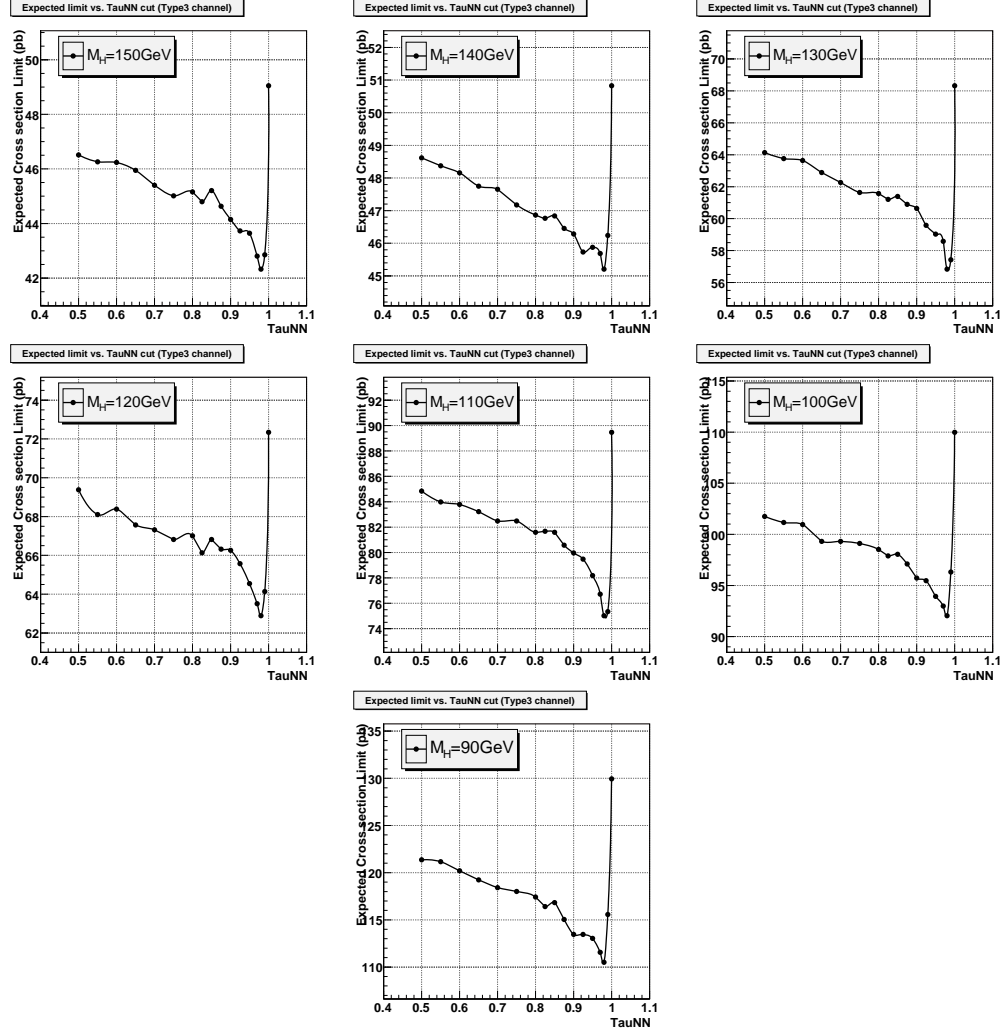Figure 4.28. Expected cross section limit as a function of the NN_τ cut for type 3 τ's. Limit derived using type 2 and 3 τ's, with the type 2 NN_τ cut fixed at 0.80.
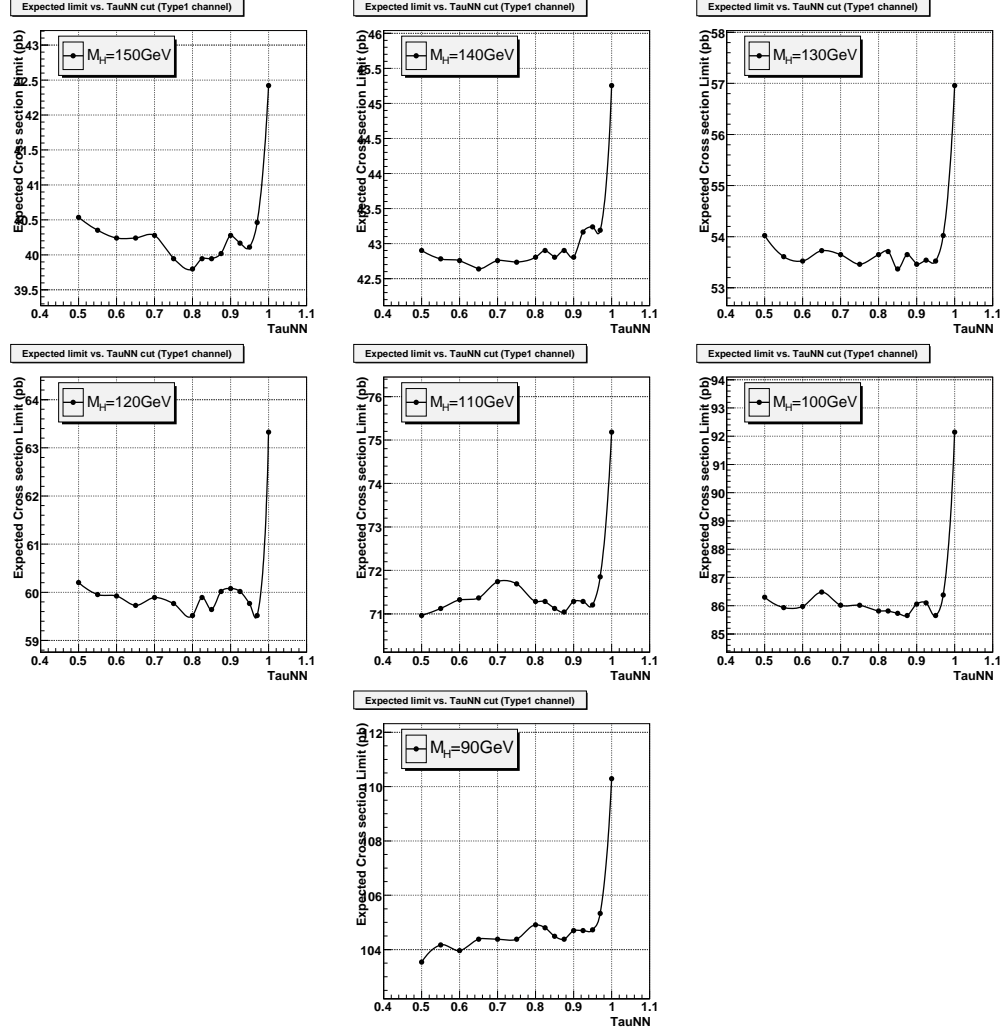
Figure 4.29. Expected cross section limit as a function of the NN_τ cut for type 1 τ's. Limit derived using type 1, 2 and 3 τ's, with the type 2 and 3 NN_τ cuts fixed at 0.80 and 0.98, respectively.

4.9.4 Optimization of the KNN Selection

The KNN was optimized separately for each τ_h type. Figures 4.30, 4.31 and 4.32 show the expected limit as a function of the KNN cut for τ-types 1, 2 and 3, respectively. As is evident from the plots, the KNN selection offers no benefit to events with type 1 or 3 τ's. Therefore, no cut on KNN is applied for these types. For events with type 2 τ's, a cut of KNN>0.4 results in the best expected limit.

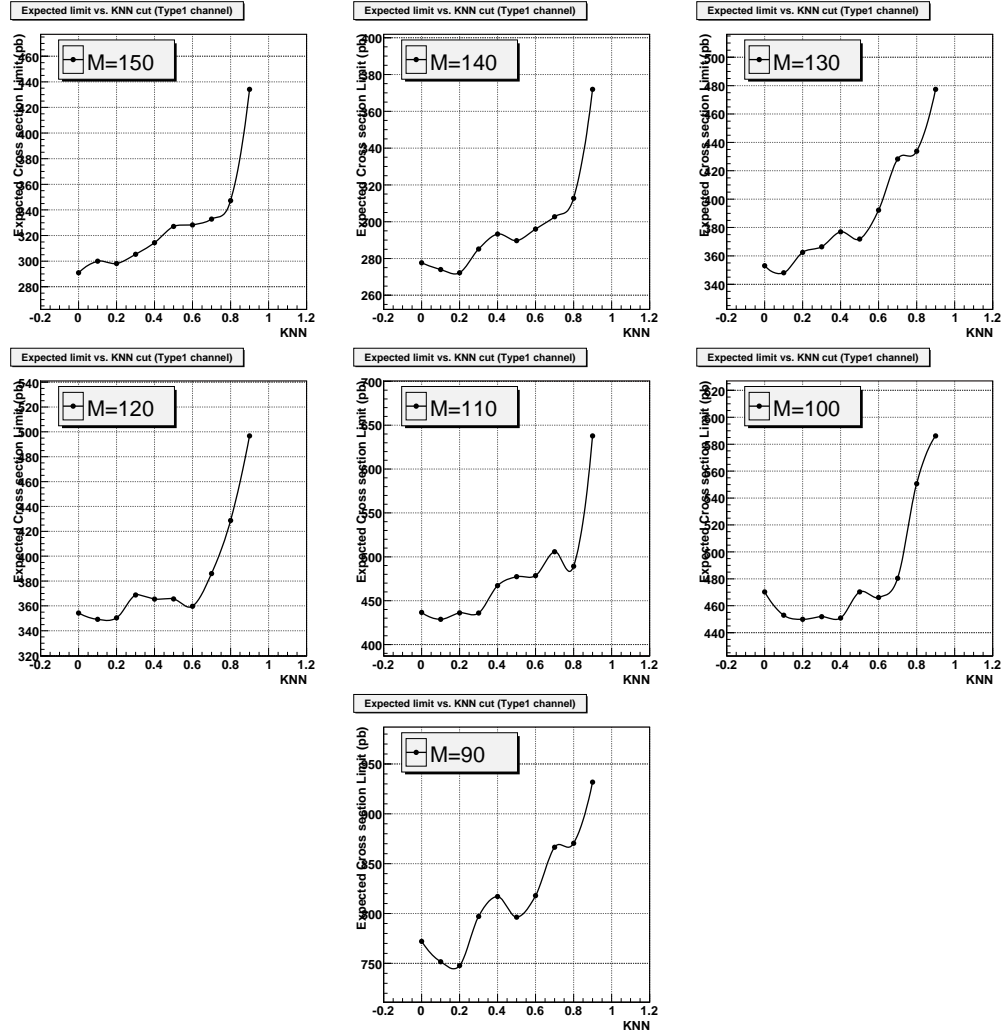Figure 4.30. Expected cross section limit as a function of the KNN cut for type 1 τ's. Limit derived using only type 1 τ's.
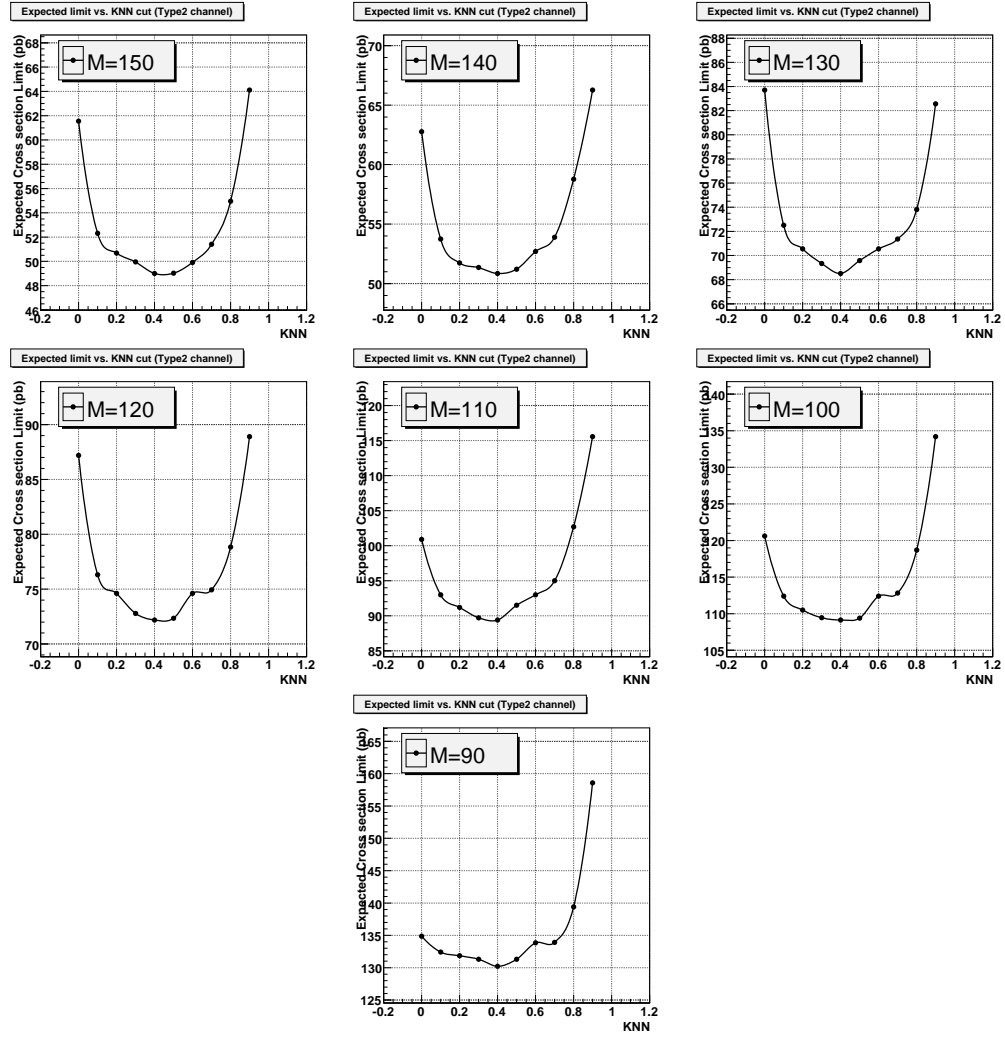
Figure 4.31. Expected cross section limit as a function of the KNN cut for type 2 τ's. Limit derived using only type 2 τ's.
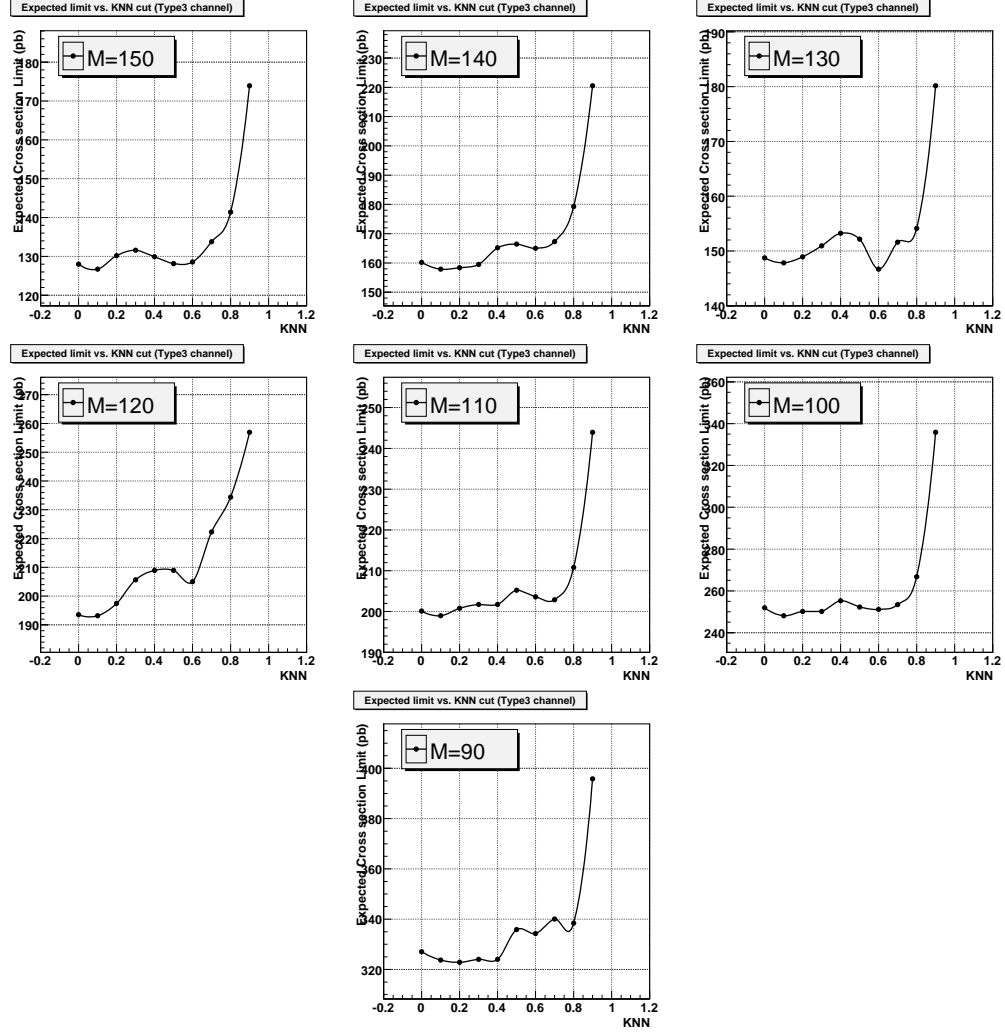
Figure 4.32. Expected cross section limit as a function of the KNN cut for type 3 τ's. Limit derived using only type 3 τ's.

118

4.10 Results

Figure 4.33 shows the 95% confidence level (C.L.) expected and measured limits as a function of the Higgs mass. The band indicates the $\pm 1\sigma$ uncertainty on the expected limit. The fact that the observed limit is somewhat outside the 1σ uncertainty of the expected limit can be traced back to Figure 4.26: for type 2 τ_h's (which dominate the result), we expect a total of 2.6 events and observe 1. However, this one observed event does not appear in the third (or even second) mass bin, where we expect the most events, but rather in the first bin, where we expect the smallest number of events. This results in a larger discrepancy between expected and observed limit than the total number of expected and observed events would indicate.
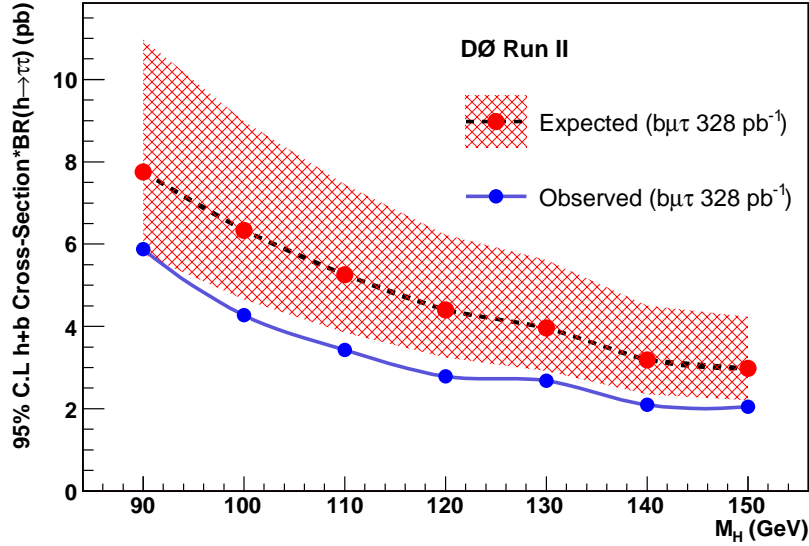

Figure 4.33. The 95% C.L. expected and measured limits on the $p\bar{p} \to bh$ cross section as a function of the Higgs mass, measured from the $\tau^+\tau^-$ decay mode. The band indicates $\pm 1\sigma$ uncertainty on the expected limit.

119

We would like to compare the bh production cross section limit from the current analysis with the one previously obtained from the $h \to b\bar{b}$ decay mode [31] using the same data set. However, the current analysis uses the updated DØ luminosity calculation [32], whereas the $b\bar{b}$ analysis from the same data is only available using the older, inaccurate DØ integrated luminosity. Therefore, for comparison purposes only, the current analysis is also shown using the older, inaccurate luminosity calculation, together with the $b\bar{b}$ result, in Figure 4.34. In this plot, the expected and measured limits from the current analysis are corrected for the branching ratio of $h/H/A \to \tau^+\tau^-$ (10%). As is evident from the plot, the $h \to \tau^+\tau^-$ decay mode is comparable to the $h \to b\bar{b}$ one, despite the 1:9 branching ratio.

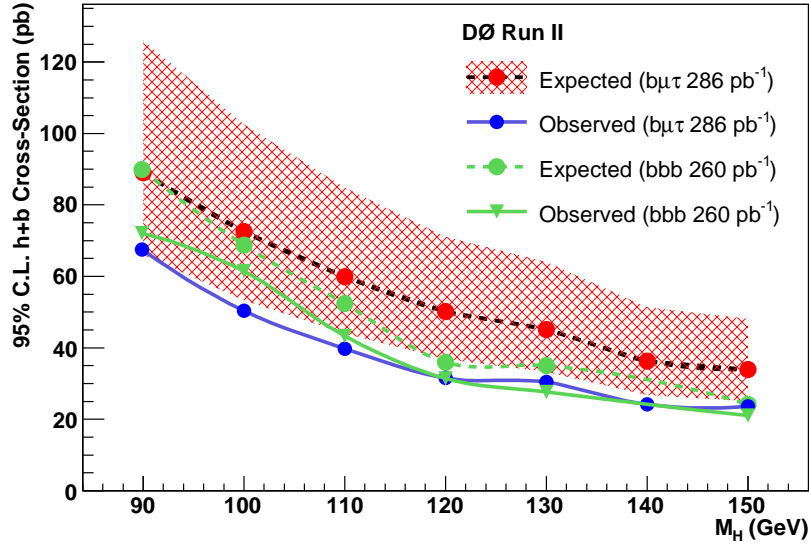Figure 4.34. The 95% C.L. expected and measured limits on the $p\bar{p} \to bh$ cross section as a function of the Higgs mass, measured from the $\tau^+\tau^-$ and $b\bar{b}$ decay modes. The band indicates $\pm 1\sigma$ uncertainty on the expected limit using the $\tau^+\tau^-$ decay. The integrated luminosities are inaccurate; the plot is provided only for comparison between the two decay modes (see text).

4.11   Interpretation within the MSSM framework

Using the cross section limit for bh production [27], we can exclude regions of $(m_A, \tan\beta)$ parameter space in the MSSM. Beyond LO, the masses and couplings of the Higgs bosons in the MSSM depend (through radiative corrections) on additional SUSY parameters, besides m_A and $\tan\beta$. Thus, we derive limits on $\tan\beta$ as a function of m_A in two specific scenarios[2]: the m_h^{max} scenario (with the parameters $M_{SUSY} = 1000$ GeV, $X_t = 2000$ GeV, $M_2 = 200$ GeV, $\mu = \pm 200$ GeV, $m_g = 800$ GeV) and the no-mixing scenario (with the parameters $M_{SUSY} = 2000$ GeV, $X_t = 0$, $M_2 = 200$ GeV, $\mu = \pm 200$ GeV, $m_g = 1600$ GeV) [33]. The MSSM enhancement of the production cross sections, as well as the branching ratios, for the Higgs bosons are calculated over the mass range 90-150 GeV using the FEYNHIGGS program [34], version 2.3.1. Since at large $\tan\beta$ the A boson is nearly degenerate in mass with either the h or the H boson, their production cross sections are added. The results are shown in Figure 4.35.

This analysis excludes a significant portion of the MSSM parameter space. For negative values of the Higgsino mass parameter μ, the $(h/H/A) \rightarrow \tau^+\tau^-$ decay mode explored here is comparable to the $b\bar{b}$ decay mode, previously published by DØ [31]. For positive values of μ, however, the $\tau^+\tau^-$ mode is superior to the $b\bar{b}$ one, as it does not suffer from the effect of the large supersymmetric radiative corrections to the Higgs decay width, associated with a change of the effective Yukawa couplings of the bottom quarks to the Higgs fields [33]. In general, the $b(h/H/A) \rightarrow b b\bar{b}$ channel [31], the $b(h/H/A) \rightarrow b\tau^+\tau^-$ channel presented here, and the inclusive $(h/H/A) \rightarrow \tau^+\tau^-$ channel [35, 36] are all complimentary, since in the regions of the MSSM phase space where the Higgs couplings to b-quarks are enhanced, the couplings to τ-leptons are suppressed, and vice-versa. The combination of all three channels will provide the

---

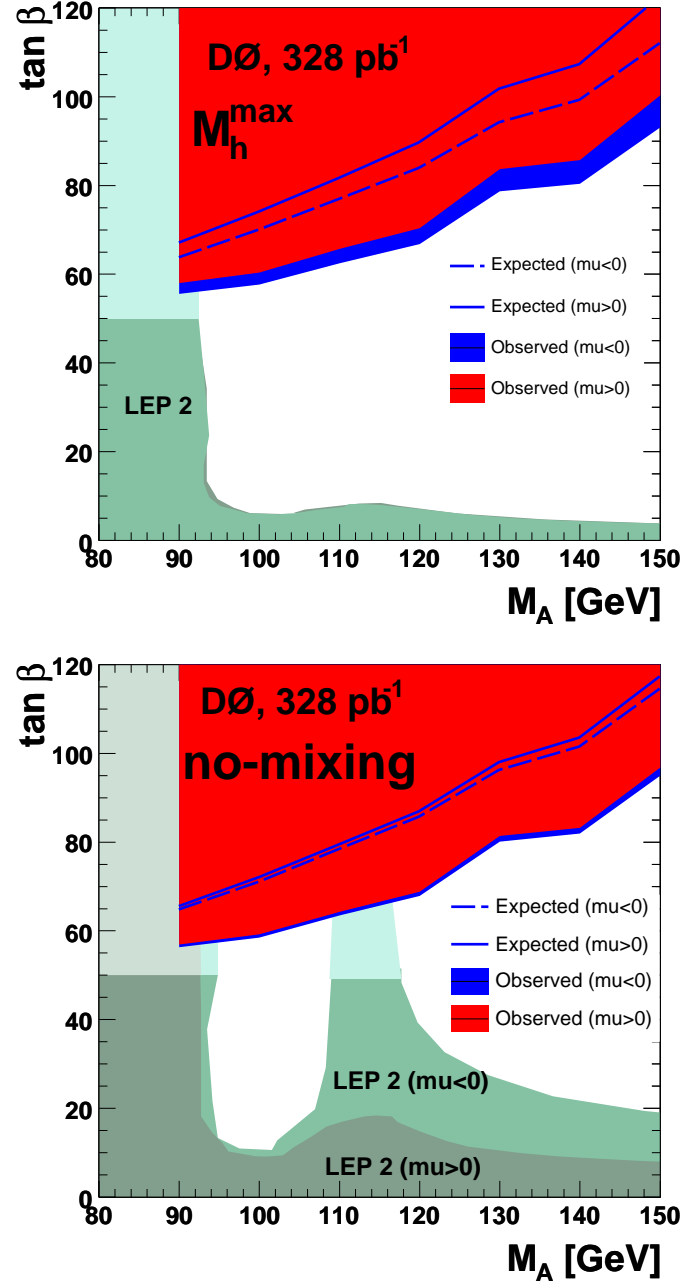[2]Both scenarios assume a CP-conserving Higgs sector.

Figure 4.35. Excluded region in the $(m_A, \tan\beta)$ plane for the m_h^{max} (left) and the no-mixing (right) scenario of the MSSM, for $\mu = +200$ GeV and $\mu = -200$ GeV. Also shown is the region excluded by the LEP experiments.

best exclusion limits.

Using the expected cross section limit for bh production, we can derive projections for the $(m_A, \tan\beta)$ region that can be excluded in the MSSM for various integrated luminosities. The results are shown in Figure 4.36 for the same m_h^{max} and no-mixing scenarios used in Figure 4.35.
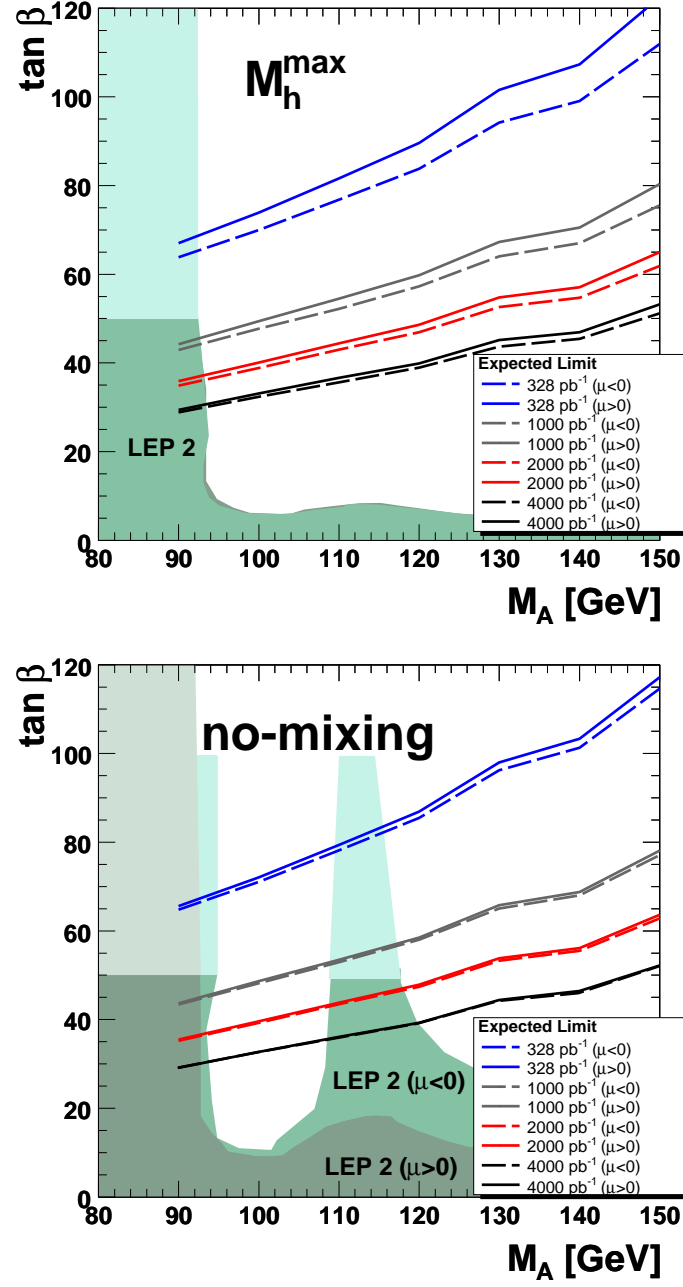
Figure 4.36. Projections of the $(m_A, \tan\beta)$ region that can be excluded in the m_h^{max} (left) and the no-mixing (right) scenario of the MSSM, for various integrated luminosities.

CHAPTER 5

CONCLUSIONS

A search has been performed for a signal from the neutral Higgs bosons in the $b + \tau^+\tau^-$ channel using data collected with the DØ detector during Run II of the Fermilab Tevatron. No evidence for the Higgs signal was found. The results were interpreted in the context of MSSM to provide limits in the m_A vs. $\tan\beta$ parameter space for two MSSM scenarios. For the m_A range of 90-150 GeV, values of $\tan\beta > 60 - 100$ were excluded with at 95% Conficence Level. Larger data sets (see Figure 4.36) should allow lower $\tan\beta$ to be excluded in the future.

BIBLIOGRAPHY

[1] M. Kaku, "Quantum Field Theory a Modern Introduction", Oxford University Press, New York (1993).

[2] D.I. Kazakov, "Beyond the Standard Model", hep-ph/0012288.

[3] S. Dawson, *et al.*, S. Dawson, "Higgs-Boson Production with One Bottom-Quark Jet at Hadron Colliders", Phys. Rev. Lett. 94, 031802 (2005)

[4] A. Patwa, Ph.D. Thesis, Stony Brook University, 2002 (unpublished).

[5] DØ Collaboration, "The DØ Upgrade Central Fiber Tracker: Technical Design Report", DØ Internal Note #4164, 1997 (unpublished). http://d0server1.fnal.gov/users/stefan/www/CFT TDR/CFT TDR.ps

[6] A. Bross *et al.*, "SCIFI 97: Conference on Scintillating Fiber Detectors", AIP Conference Proceedings 450, 1998.

[7] M. Adams *et al.*, "Design Report of the Central Preshower Detector for the D Upgrade", D Internal Note #3014.

[8] A. Gordeev *et al.*, "Technical Design Report of the Forward Preshower Detector for the DØ Upgrade", DØ Internal Note #3445, 1998 (unpublished).

[9] M. Gao, A Search for Extra Neutral Gauge Boson in the Dielectron Channel with the DØ Detector in $p\bar{p}$ Collisions at ps=1.96 TeV, Ph.D. Thesis, Columbia University, 2003 (unpublished).

[10] A. Melnitchouk, Search for non-SM Light Higgs Boson in the $h \rightarrow \gamma\gamma$ Channel, Ph.D. Thesis, Brown University, 2003 (unpublished)

[11] P. Demine, Study of the tri-lepton events in the Run II data of the D experiment at the Tevatron. Interpretation in the R-parity violating supersymmetry framework (λcoupling), Ph.D. Thesis, ISN Grenoble, 2002 (unpublished).

[12] O. Peters, "Muon Segment Alghorithm", http://www-d0.fnal.gov/nikhef/muon_reco/segmentreco/

[13] C. Clement *et al.*, MuonID Certication for p14, DØ Internal Note #4350.

[14] G. C. Blazey *et al.*, "Proceedings of the Workshop on QCD and Weak Boson Physics in Run II", 1999, edited by U.Baur, R.K. Ellis, and D. Zeppenfeld, Fermilab Pub-00/297, p. 47

[15] Daniel Bloch, Benoit Clement, Denis Gele, Sebatian Greder, "Performance of the JLIP b-tagger in p14", DØ Internal Note #4348, 2004.

[16] G. Borissov, "Ordering a Chaos or ...Technical Details of AA Tracking" http://www-d0.fnal.gov/atwork/adm/d0_private/2003-02-28/adm_talk.ps

[17] A. Garcia-Bellido *et al.*, "Primary Vertex certification in p14", DØ Note #4320, 2004.

[18] A. Schwartzman and M. Narain, "Probabilistic Primary Vertex Selection",. DØ Note #4042, 2002.

[19] T. Sjöstrand *et al.*, PYTHIA, Comput. Phys. Commun. **135**, 238 (2001).

[20] M. Mangano *et al.*, ALPGEN, JHEP **0307**, 1 (2003).

[21] F. Deliot, G. Hesketh, P. Telford and B. Tuchming, "Measurement of $\sigma(p\bar{p} \rightarrow WX) \times Br(W \rightarrow \mu\nu)$ at $\sqrt{s} = 1.96$ TeV", DØ Note 4749.

[22] C. Clement *et al.*, "Muon ID Certification for p14", DØ Note 4350.

[23] M. Arov *et al.*, "τ identification with neural networks for pass2 data", DØ Note 4773.

[24] D. Bloch and B. Clément, "Update of the JLIP *b*-tagger Performance in p14/pass2 with JES 5.3", DØ Note 4824.

[25] DØ Jet Energy Scale group, http://www-d0.fnal.gov/phys_id/jes/d0_private/cerified/cerified.html

[26] C. Galea, S. Nelson, A. Patwa and S. Protopopescu, "Measurement of the production cross section times branching ratio of $Z/\gamma^* \rightarrow \tau\tau$ in $p\bar{p}$ interactions at $\sqrt{s} = 1.96$ TeV at DØ", DØ Note 4550.

[27] J. Campbell, R.K. Ellis, F. Maltoni and S. Willenbrock, Phys. Rev. D **67**, 095002 (2003), hep-ph/0204093.

[28] N. Kidonakis and R. Vogt, Phys. Rev. D **68**, 114014 (2003); hep-ph/0308222.

[29] http://www-clued0.fnal.gov/~nunne/cross-sections/caps_xsect.html

[30] T. Junk, Nucl. Instrum. Methods Phys. Res. A **434**, 435 (1999).

[31] DØ Collaboration, V. M. Abazov *et al.*, Phys. Rev. Lett. **95**, 151801 (2005).

[32] B. Casey *et al.*, "Determination of the Effective Inelastic $p\bar{p}$ Cross-Section for the DØ Luminosity Measurement Using Upgraded Readout Electronics", DØ Note 4958, and G. Snow, for the DØ Luminosity Working Group, "Adjustments to the Measured Integrated Luminosity in Run IIa", DØ Note 5139.

[33] M. Carena, S. Heinemeyer, C.E.M. Wagner and G. Weiglein, Eur. Phys. J. C **45**, 797 (2005), hep-ph/0511023.

[34] S. Heinemeyer, W. Hollik and G. Weiglein, Comput. Phys. Commun. **124**, 76 (2000), hep-ph/9812320; FEYNHIGGS program: http://www.feynhiggs.de.

[35] CDF Collaboration, A. Abulencia *et al.*, Phys. Rev. Lett. **96**, 011802 (2006).

[36] DØ Collaboration, V. M. Abazov *et al.*, Phys. Rev. Lett. **97**, 121802 (2006).

[37] DØ Collaboration, S. Abachi *et al.*, Nucl. Instr. and Meth. A338, 185 (1994).